ABSTRACT

Title of Dissertation: Designing Optical Quantum Computing with Minimal Hardware

Yu Shi
Doctor of Philosophy, 2023

Dissertation Directed by: Professor Edo Waks
Department of Electrical and Computer Engineering

Photons, while indispensable for quantum communication and metrology, fall short due to limited photon-photon interactions, thus suboptimal for quantum computing. This thesis explores the use of an atom-photon interface to foster entanglement between photons, thereby facilitating more scalable optical quantum computing with reduced resource demands.

I initially discuss the deterministic generation of multi-dimensional cluster states via an atom-photon interface and time-delay feedback. These cluster states are essential resources for fault-tolerant measurement-based quantum computing. A diagrammatic method is introduced to derive tensor networks of highly entangled states, thereby aiding in the simulation of states produced from sequential photons. Subsequently, I investigate the implementation of the optical quantum Fourier transform through the interface, which facilitates photon-photon interactions and significantly reduces the dependence on linear optical devices. In addition to devising techniques, I introduce an error metric for non-trace-preserving quantum operations that aligns with

fault-tolerant quantum computing theory. This metric is beneficial for assessing errors across various quantum platforms and post-selected protocols.

Overall, this research advances the field of optical quantum information processing, proposing scalable, practical solutions for quantum computing. Concurrently, it pioneers novel error metrics, providing a promising benchmarking and optimization strategy for robust quantum information processing.

DESIGNING OPTICAL QUANTUM COMPUTING WITH MINIMAL HARDWARE

by

Yu Shi

Dissertation submitted to the Faculty of the Graduate School of the
University of Maryland, College Park in partial fulfillment
of the requirements for the degree of
Doctor of Philosophy
2023

Advisory Committee:
Professor Edo Waks, Chair/Advisor
Professor Avik Dutt
Professor Cheng Gong
Professor Julius Goldhar
Professor Ronald L. Walsworth
Professor Victor M. Yakovenko

Acknowledgments

I would like to express my deep gratitude to my advisor, Edo Waks, whose guidance and steadfast support have been instrumental in the progression of my doctoral studies. My committee members, Avik Dutt, Cheng Gong, Julius Goldhar, Ronald Walsworth, and Victor Yakovenko, deserve special recognition for their contributions and insights that brought this thesis to fruition.

In addition, I extend my sincere thanks to Shuo Sun, whose inspiring discussions have had a significant impact on my work. My gratitude also goes to Alexandra Brozena for her elaborate editing of my papers. Moreover, I am indebted to Dorothea Brosius for providing the LaTex template, a significant aid in the composition of my thesis.

I am immensely grateful to the vibrant research community at the University of Maryland. Collectively, we have cultivated a stimulating, open research environment that has been pivotal to my growth and success.

While it is impossible to acknowledge every individual who has played a part in this journey, I deeply regret any inadvertent omissions. I express my sincere appreciation for each contribution, big or small, that helped shape this thesis.

Table of Contents

Acknowledgements iii

Table of Contents iii

List of Figures v

Chapter 1: Introduction 1
- 1.1 Quantum Computing: a Primer . . . 1
  - 1.1.1 Classical vs. Quantum Computing . . . 1
  - 1.1.2 Building Blocks of Quantum Computers . . . 3
  - 1.1.3 Defeating Errors in Quantum Computing . . . 7
  - 1.1.4 Platforms for Quantum Computing . . . 8
- 1.2 Optical Quantum Information Processing . . . 11
  - 1.2.1 Overview of Optical QIP . . . 11
  - 1.2.2 Photonic Encoding . . . 12
  - 1.2.3 Minimal Hardware in Quantum Computing . . . 15
- 1.3 Thesis Contributions and Outline . . . 17

Chapter 2: Methodology: Atom-Photon Interface 19
- 2.1 Overview of Atom-Photon Interface . . . 19
  - 2.1.1 Bridging Stationary and Flying Qubits . . . 19
  - 2.1.2 Atom-Photon Interface Applications . . . 20
  - 2.1.3 Technologies for Atom-Photon Interfaces . . . 22
- 2.2 Cavity Quantum Electrodynamics Model . . . 23
  - 2.2.1 Electron-Charged Quantum Dots in Cavity . . . 23
  - 2.2.2 Controlled Phase-Flip Gate . . . 27
  - 2.2.3 Coherent Time-Delay Feedback Control . . . 29
- 2.A Derivation of Heisenberg Equations of Motion . . . 31

Chapter 3: Multi-Dimensional Optical Cluster State Generation 35
- 3.1 Cluster-State Quantum Computing . . . 35
  - 3.1.1 What is a Cluster State? . . . 35
  - 3.1.2 Universality of Cluster-State Quantum Computing . . . 36
  - 3.1.3 Fault-Tolerance and Cluster State Dimensionality . . . 39
  - 3.1.4 Review on the Generation of Photonic Cluster States . . . 40
- 3.2 Protocol for 3D Cluster State Generation with Time-Delay Feedback . . . 41

3.2.1 3D Lattice Linearization . . . 41
3.2.2 Building Nearest-Neighbor Entanglement . . . 43
3.2.3 Non-Nearest-Neighbor Entanglement and Time-Delay Feedback . . . 44
3.2.4 3D Cluster State Generation Procedure . . . 45
3.3 Physical Implementation . . . 46
3.4 Extension to Higher Dimensional States . . . 50
3.5 Analysis of Cluster State Fidelity . . . 52
3.5.1 Tensor Network Formalism . . . 52
3.5.2 Fidelity Evaluation . . . 56
3.5.3 Parameter Settings . . . 58
3.5.4 Simulation Results . . . 59
3.A Derivation of Quantum Circuits for Cluster State Generation . . . 61
3.B Matrix Product Operator Decomposition . . . 64
3.C Derivation of the Imperfect Photon-Photon CZ Gate . . . 65

Chapter 4: Optical Quantum Fourier Transform 67
4.1 Basics of Quantum Fourier Transform . . . 67
4.2 Atom-Photon Interface Revisited . . . 69
4.2.1 Controlled Phase-Shift Gate . . . 69
4.2.2 Active Phase Tuning . . . 71
4.3 Implementation of the Optical Quantum Fourier Transform . . . 73

Chapter 5: Error Metric for Non-Trace-Preserving Operations 77
5.1 Quantum Error Correction and Threshold . . . 77
5.2 Error Measure and Diamond Distance . . . 80
5.3 General Distance for Non-Trace-Preserving Operations . . . 82
5.3.1 Characteristic of Non-Trace-Preserving Errors . . . 82
5.3.2 Defining the General Distance . . . 83
5.3.3 Upper Bound for General Distance . . . 85
5.4 Applications of the Error Metric . . . 87
5.4.1 Leakage in Atom-Photon Interface . . . 87
5.4.2 Leakage in Neutral Atoms . . . 88
5.A Stability of the General Distance . . . 91
5.B Renormalization of Quantum Operations . . . 94
5.C Calculation of the Normalizing Distance . . . 96

Bibliography 99

List of Figures

2.1 Characteristic size of a quantum dot relative to a single atom and a photonic nanostructure . . . 24
2.2 Schematic diagram of the atom-photon interface . . . 26
2.3 Schematic diagram of the cavity field along with the input and output fields for a single-sided cavity. . . . 31

3.1 Depiction of Cluster States and Tree-Level Graph State . . . 36
3.2 Simulating a universal two-qubit quantum circuit using cluster states . . . 38
3.3 Transformation of a 3d cluster state into a linear chain . . . 42
3.4 Scheme for establishing nearest-neighbor photon entanglement . . . 44
3.5 Scheme for establishing non-nearest-neighbor photon entanglement . . . 45
3.6 Generation of 3D cluster states with helical boundaries . . . 47
3.7 Physical setup for generating a 3d cluster state with sequential photon reflection . . . 49
3.8 Schematic diagrams and setup for generating s-dimensional cluster states . . . 51
3.9 Tensor network decomposition and representation of a 1D cluster state . . . 53
3.10 Tensor network decomposition and representation of a 3D cluster state . . . 55
3.11 Scaling factor (β) of fidelity, as a function of both resonant cooperativity and magnetic field for a 3D cluster state. . . . 60

4.1 Circuit for the discrete quantum Fourier transform. . . . 68
4.2 Level structure of the reengineered atom-cavity system. . . . 70
4.3 Plot of the controlled phase shift $\Delta\theta$ as a function of the Stark shift Δ_S. . . . 73
4.4 Scheme for optical quantum Fourier transform . . . 74

5.1 Error reduction rate as a function of leakage probability for different detection efficiencies. . . . 91

Chapter 1: Introduction

1.1 Quantum Computing: a Primer

1.1.1 Classical vs. Quantum Computing

Computers have become indispensable in modern society, catalyzing advances across diverse fields and revolutionizing many aspects of daily life. From scientific research and engineering to design, manufacturing, communication, and entertainment, their widespread use is primarily due to their ability to execute complex calculations and simulate intricate physical systems. The bedrock of this versatility and broad applicability is the Church-Turing thesis [1], which asserts that any real-world computation can be translated into an equivalent computation involving a Turing machine.

In essence, a Turing machine is a theoretical computational device. It comprises an infinitely long tape divided into discrete cells, a read-write head that traverses the tape, and a control unit that determines the machine's behavior. The tape functions as the machine's memory, while the read-write head can either read the symbol at its current position, write a new symbol, and shift left or right along the tape. Based on a set of instructions, known as a program, the control unit manipulates the machine's actions according to the current state and the symbol being read. This simple yet powerful architecture imparts a Turing machine with the ability to simulate

any computation. Consequently, computational models that can emulate Turing machines, such as modern programming languages like C++ and Python, inherit this versatile computational capacity.

Building on this foundation, the extended Church-Turing thesis takes the concept a step further. It asserts that any real-world computational model can be simulated by a Turing machine within polynomial time complexity. This idea is critical in the field of computational complexity theory as it formalizes the notion of efficient computation. It indicates that classical computers, based on the Turing machine model, are not only universally applicable but also achieve optimal efficiency in terms of computational resources. However, this theory has not gone unchallenged [2].

The advent of quantum computing has presented a formidable challenge to the extended Church-Turing thesis. Richard Feynman, in his seminal 1981 lecture "Simulating Physics with Computers," [3] argued that classical computers would struggle to simulate quantum mechanics effectively. He pointed to the exponential resources required to represent a quantum system and the absence of quantum phenomena like superposition and entanglement in classical systems as significant hurdles. Furthermore, Feynman introduced a pioneering concept that could overcome these challenges: a "universal quantum simulator," now known as a quantum computer. This innovative device, operating under the principles of quantum mechanics, promised the ability to perform tasks previously deemed intractable for classical computers, such as the efficient and precise simulation of quantum systems.

Quantum computers promise to outperform classical computers in numerous areas, not only in simulating quantum systems but also in solving a broad spectrum of mathematical problems. A remarkable example of this is Shor's algorithm [4], which enables the factorization of

large numbers on a quantum computer in polynomial time, while the best-known classical algorithm requires exponential time for the same task. Another striking illustration is Grover's algorithm [5]. Designed for search problems, it allows a quantum computer to locate a target within an unsorted database of N objects in approximately $O(\sqrt{N})$ time, while a classical computer would require an exhaustive search, taking up to $O(N)$ time. These groundbreaking algorithms underscore the transformative potential of quantum computing.

The full implementation of Shor's and Grover's algorithms critically depends on the future development of fault-tolerant quantum computers. In the meantime, researchers are demonstrating quantum advantage by identifying practical computational tasks executable on present-day noisy intermediate-scale quantum (NISQ) devices [6] but beyond the reach of classical computers. Two landmark experiments include Random Circuit Sampling by Google [7] and Gaussian Boson Sampling by the University of Science and Technology of China [8]. Despite current technological limitations and errors, these tasks can be performed on a quantum computer in mere minutes, which is significantly faster than on classical computers. With even the most plentiful resources, accomplishing the same tasks on classical supercomputers would require an impractically long computation period, estimated to be several decades or even centuries.

1.1.2 Building Blocks of Quantum Computers

A qubit, or quantum bit, is the fundamental unit of quantum information processing, analogous to the classical bit in conventional digital computers [1]. However, unlike classical bits, which can exist solely in a definite state of either 0 or 1, a qubit leverages the principles of quantum mechanics to exist in a superposition of states. This superposition principle allows a qubit

to inhabit a linear combination of the computational basis states $|0\rangle$ and $|1\rangle$ simultaneously. This can be represented by the state vector $|\psi\rangle = \alpha|0\rangle + \beta|1\rangle$ in a Hilbert space, where α and β are complex probability amplitudes such that $|\alpha|^2 + |\beta|^2 = 1$. Nevertheless, upon measurement, the qubit collapses from its superposition state to one of the basis states, either $|0\rangle$ or $|1\rangle$, with probabilities given by $|\alpha|^2$ and $|\beta|^2$, respectively. In addition to the computational basis states, there are other important basis states used in quantum computing, including the $|+\rangle$ and $|-\rangle$ states. These are superpositions of the $|0\rangle$ and $|1\rangle$ states. More specifically, the $|+\rangle$ state is defined as $\frac{1}{\sqrt{2}}(|0\rangle + |1\rangle)$, and the $|-\rangle$ state is defined as $\frac{1}{\sqrt{2}}(|0\rangle - |1\rangle)$. It's important to note that there are infinitely many ways to choose a basis for the qubit's Hilbert space, and different choices of basis are useful in different situations.

Quantum gates in quantum computing function as operations on qubits, much as classical logic gates operate on classical bits. Unlike classical gates, however, quantum gates are represented by unitary matrices, thereby preserving the normalization of quantum states. Single-qubit gates can be characterized by a 2×2 unitary matrix that operates on an individual qubit's state vector. There are several foundational single-qubit gates playing pivotal roles in quantum computing, such as the Pauli gates, represented by the following matrices:

$$\sigma_x = \begin{pmatrix} 0 & 1 \\ 1 & 0 \end{pmatrix}, \quad \sigma_y = \begin{pmatrix} 0 & -i \\ i & 0 \end{pmatrix}, \quad \sigma_z = \begin{pmatrix} 1 & 0 \\ 0 & -1 \end{pmatrix}. \tag{1.1}$$

The Pauli-X gate, commonly likened to the classical NOT gate, flips the state of a qubit between $|0\rangle$ and $|1\rangle$. The Pauli-Z gate leaves the state $|0\rangle$ unchanged but applies a phase flip to the state $|1\rangle$, resulting in $-|1\rangle$. The Pauli-Y gate performs both a bit flip and a phase flip. Another significant

single-qubit gate is the Hadamard gate, represented as

$$H = \frac{1}{\sqrt{2}} \begin{pmatrix} 1 & 1 \\ 1 & -1 \end{pmatrix}. \tag{1.2}$$

This gate maps the basis state $|0\rangle$ to $|+\rangle$ and $|1\rangle$ to $|+\rangle$, thus creating a balanced superposition of states. Two other essential single-qubit gates are the P and T gates, which apply phase shifts of $\pi/2$ and $\pi/4$ respectively to the state $|1\rangle$, leaving the state $|0\rangle$ unchanged. These gates are indispensable for achieving universal and fault-tolerant quantum computing [9].

The state space of a single qubit is two-dimensional. However, when considering multiple qubits or a composite quantum system, the state of the system is represented within the tensor product space, constructed from the individual Hilbert spaces of the qubits. The dimensionality of this tensor product space equals the product of the dimensions of the individual spaces. To illustrate, consider two qubits, each with a two-dimensional Hilbert space. The system composed of these two qubits is represented in a four-dimensional Hilbert space. The basis states of this composite system—$|00\rangle$, $|01\rangle$, $|10\rangle$, and $|11\rangle$—are formed through the tensor products of the individual qubits' basis states. Within this combined Hilbert space, a quantum state can simultaneously exist in a superposition of all its basis states, each of which corresponds to one possible configuration of all the qubits. Consequently, an n-qubit quantum computer can effectively process 2^n configurations simultaneously due to the feature of quantum mechanics.

In systems of multiple qubits, it is possible to form states that cannot be factored into a product of individual qubit states. Such a state is termed "entangled," and this unique correlation is known as "entanglement." For instance, the Bell state $\frac{1}{\sqrt{2}}(|00\rangle + |11\rangle)$ represents an

entangled two-qubit state [10]. This state exhibits a fascinating feature: when the first qubit is measured and found to be in state $|0\rangle$, the second qubit will instantaneously collapse to state $|0\rangle$, and the same applies for the state $|1\rangle$, despite the second qubit's state being indeterminate prior to the measurement. In quantum computing, entanglement plays a pivotal role as the underlying mechanism of quantum algorithms. Besides the Bell state, other entangled states, such as the Greenberger–Horne–Zeilinger (GHZ) state [11] and cluster states [12], exist. Specifically, cluster states are fundamental for measurement-based quantum computing [13] and are particularly crucial in the realm of optical quantum computing.

To establish entanglement between qubits, we need to employ two-qubit gates, which are hence sometimes referred to as entangling gates. A prominent example of a two-qubit gate is the controlled NOT (CNOT) gate, which is denoted as CNOT $= |0\rangle\langle 0| \otimes I + |1\rangle\langle 1| \otimes X$. The tensor product representation expands the CNOT gate in terms of the individual control and target qubits. The CNOT gate executes a NOT operation, also known as an X gate, on the target qubit exclusively when the state of the control qubit is in state $|1\rangle$. In essence, it flips the target qubit if, and only if, the control qubit is in state $|1\rangle$. Conversely, if the control qubit is in state $|0\rangle$, the target qubit remains in its original state. By applying a CNOT gate to two qubits initially in a superposition state, one can create an entangled state between them.

The combination of prevalent single-qubit gates, such as the Pauli and Hadamard, alongside phase gates like the P and T gates, forms a comprehensive set that can be employed to conduct any desired manipulation on a single qubit. Moreover, two-qubit gates serve to facilitate interaction and entanglement among qubits, together constituting a universal quantum gate set [1]. The Solovay-Kitaev theorem [14] shows that any quantum operation can be approximated to an arbitrary level of precision using a finite sequence of gates from this set. Consequently, any quantum

algorithm can be implemented by performing a sequence of single-qubit and CNOT gates. A universal quantum computer can be realized by strategically applying these gates to a properly arranged array of qubits and leveraging the principles of superposition and entanglement. Such a computer has the capacity to execute any quantum algorithm, harnessing the extraordinary power of quantum mechanics to process information in ways that dramatically surpass the capabilities of conventional classical computers.

1.1.3 Defeating Errors in Quantum Computing

In quantum computing, errors pose a formidable challenge. Owing to the high sensitivity inherent in quantum systems, even minor interactions with the external environment can induce substantial errors. Such errors potentially compromise the fidelity of information processed by quantum gates, thereby impeding the successful implementation of quantum algorithms and potentially resulting in erroneous or nonsensical outcomes. The ramifications of these errors are substantial, presenting a major obstacle to the development and realization of large-scale, reliable quantum computers.

Decoherence serves as a primary source of error in quantum systems. It designates the process by which a quantum system forfeits its inherent quantum properties, i.e., superposition and entanglement, consequently transitioning into a classical system. This phenomenon is typically propelled by the interaction of qubits with the external environment, encompassing all elements outside the quantum system, such as heat, electromagnetic radiation, and even cosmic rays [15]. Since quantum computers rely on the principles of superposition and entanglement to solve certain problems beyond the reach of classical computers, decoherence can undermine these delicate

quantum properties, rendering quantum algorithms ineffective and thereby reducing the quantum advantage. When a quantum system fully succumbs to decoherence, it effectively turns into a classical system without any quantum advantage [16]. There exist other types of errors in quantum systems too, including gate inaccuracies, readout errors, state preparation errors, qubit crosstalk, and leakage. The construction of a reliable quantum computer necessitates addressing and mitigating all these errors.

To address this issue, various quantum error-correcting codes and protocols have been developed. The concept of quantum error correction incorporates redundancy, similar to classical error correction, but with significant differences due to the unique characteristics of quantum information, especially the no-cloning theorem and entanglement. Widely adopted protocols include the Calderbank-Shor-Steane (CSS) codes [17] and surface codes [18]. The goal is to construct a logical qubit from a collection of physical qubits in such a way that errors can be detected and corrected without disturbing the information they contain. Importantly, minimizing errors in quantum computers involves not only correction after occurrence but also proactive prevention. This includes developing more stable qubits [19–22], improving gate fidelity [23–26], and creating better isolation for quantum systems [27].

1.1.4 Platforms for Quantum Computing

Various physical systems can serve as platforms for implementing qubits and constructing quantum computers. The chosen platform impacts key factors like the qubits' coherence times, error rates, operational speeds, as well as practical considerations such as scalability and manufacturability. Among the many physical implementations under investigation, certain platforms

have gained prominence due to their unique properties and technological advancements.

Trapped-ion quantum computers [28] utilize individual ions, confined by electromagnetic fields, as qubits. Quantum states are represented by each ion's internal energy levels. Quantum operations are performed by applying laser or microwave pulses, with entanglement realized through the ions' mutual Coulomb interaction. Trapped ions exhibit extended coherence times and high-fidelity operations, which are two significant advantages. However, challenges exist in scaling these systems and controlling interactions between distant ions.

Neutral-atom quantum computing [29] traps individual atoms in an optical lattice formed by intersecting laser beams, where the internal states of the atoms act as qubits. This platform's primary advantage lies in its inherent scalability, as optical lattices can contain large arrays of atoms. Quantum operations are executed using additional laser or microwave pulses. However, achieving high-fidelity operations and addressing individual atoms in a large array can be challenging.

Nitrogen-vacancy (NV) centers in diamond [30] provide another promising platform. Here, a qubit is implemented by the spin state of an electron associated with the NV center. These systems can operate at room temperature and possess long coherence times, making them particularly attractive for quantum sensing applications [31, 32]. However, the development of high-fidelity multi-qubit gates and a scalable architecture remains a challenge.

Quantum dots [33] are nano-sized semiconducting particles whose electron states can be manipulated to form qubits. These dots can be fabricated using techniques compatible with modern semiconductor industry processes, offering a pathway to scalable quantum computing. However, maintaining coherence and achieving high-fidelity operations in these systems is quite challenging due to their susceptibility to environmental noise.

Superconducting circuits [34], also known as superconducting qubits, employ the quantum behavior of macroscopic electrical circuits, with the circuit's energy levels forming the qubit's basis states. Superconducting qubits can be fabricated using established microfabrication techniques and can be electronically controlled. These systems have made significant strides and form the backbone of several leading quantum computers, including those by IBM and Google. However, superconducting circuits require cryogenic systems for operation, leading to shorter coherence times and scalability issues due to the necessity for larger dilution refrigerators when increasing the number of superconducting qubits.

Photonic quantum computing [35] uses individual photons as qubits, encoding information in various quantum states, such as polarization or path. Leveraging advancements in optical communication technology, these systems offer benefits such as easy qubit manipulation, high measurement precision, extended coherence times, and an inherent compatibility with quantum communication and networking applications. This is due to the weak interaction of photons with the environment and their ability to travel long distances. However, optical quantum computing also faces unique challenges. Implementing two-qubit gates is problematic due to the weak interaction between photons. To circumvent this, many schemes employ measurement-based quantum computation (MBQC) [13, 36, 37], which necessitates the preparation of a highly entangled state of numerous photons, known as a cluster state [38–46]. Another significant hurdle is the efficiency of single-photon sources and detectors [47], which can lead to computational errors. Despite these challenges, substantial progress is being made in this field.

1.2 Optical Quantum Information Processing

1.2.1 Overview of Optical QIP

Optical quantum information processing (QIP) has emerged as a promising field. This approach leverages the unique properties of photons, particles of light, as the fundamental units of quantum information, known as qubits. Photons, with their robustness to environmental noise, ability to maintain quantum coherence over long periods and distances, and capacity to be manipulated with high precision using established optical technologies, offer a unique set of advantages for quantum information processing.

Optical quantum information processing presents an array of diverse applications [48], each of which harnesses the unique properties of photons in remarkable ways. Quantum communication employs photons as ideal carriers of quantum information over long distances. Existing fiber-optic networks can facilitate Quantum Key Distribution (QKD), enabling parties to share a secure encryption key, with its security firmly rooted in quantum mechanics. Quantum teleportation allows the transfer of a qubit's state from one location to another without physically transmitting the qubit itself. Moreover, quantum sensing leverages squeezed states of light, for example, to attain measurements with enhanced precision compared to classical systems. Quantum imaging employs quantum correlations between photons to produce images of objects with higher resolution or sensitivity than traditional methods [49]. Techniques such as ghost imaging [50] use entangled photons to form an image of an object, even when one of the photons doesn't interact with the object directly. In quantum computing, photons can serve as qubits, implementing algorithms via a series of optical gates and measurements. Additionally, distributed

quantum computing broadens the notion of quantum computing by locating qubits at disparate network nodes and enabling quantum communication between these nodes [51]. Given their suitability for long-distance transmission, photons naturally fit the role of qubits in such systems.

1.2.2 Photonic Encoding

In optical quantum computing, quantum information can be encoded into the bosonic modes of light [52]. A bosonic mode, described by annihilation and creation operators, represents a quantum state that photons can occupy. The number of photons in the mode is described by a Fock state $|n\rangle$, representing n photons in the mode. Typical bosonic modes of photons include path, polarization, time bin, and frequency.

Single-rail encoding and dual-rail encoding represent two common methods for encoding qubits into bosonic modes, each with its distinct features. Single-rail encoding employs the presence or absence of a photon in a single mode to represent the two states of a qubit. Typically, the Fock state $|1\rangle$ encodes the state $|1\rangle$ of the qubit, and the Fock state $|0\rangle$ denotes the state $|0\rangle$ of the qubit. A general quantum state of the qubit can be expressed as $\alpha|0\rangle + \beta|1\rangle$, where α and β are complex numbers. Single-rail encoding is straightforward and resource-efficient but can be more vulnerable to loss and noise.

In contrast, dual-rail encoding employs two bosonic modes to store a single qubit. The presence of a photon in one mode and its absence in the other symbolize the two states of a qubit. Specifically, the Fock state $|1\rangle_1|0\rangle_2$, with a photon in the first mode and none in the second, encodes the state $|1\rangle$ of the qubit. Alternatively, the Fock state $|0\rangle_1|1\rangle_2$, with no photon in the first mode but one in the second, corresponds to the state $|0\rangle$ of the qubit. A general quantum state of

the qubit can be written as $\alpha|0\rangle_1|1\rangle_2 + \beta|1\rangle_1|0\rangle_2$. As dual-rail encoding exhibits more robustness against photon loss [53], this thesis concentrates on dual-encoding based on photon polarization. That is, the horizontal and vertical polarization states of a photon represent the two basis states of a qubit. Polarization encoding is widely utilized due to the convenience of its manipulation using standard optical components. However, other encodings bear similar principles and can be understood in analogous ways.

1.2.2.1 Single-Photon Gates

For photonic qubits with polarization encoding, commonly employed optical elements for enacting single-qubit gates include wave plates and polarizing beam splitters. Wave plates, such as half-wave ($\lambda/2$) and quarter-wave ($\lambda/4$) plates, can induce a phase shift between the two orthogonal polarization components of a photon. By adjusting the orientation of a wave plate, a single-qubit rotation along any axis can be accomplished. As an illustration, a Hadamard gate can be realized with a $\lambda/2$ wave plate set at a 22.5° angle [52]. Moreover, achieving an arbitrary rotation necessitates a $\lambda/4$-$\lambda/2$-$\lambda/4$ wave plates sequence.

1.2.2.2 Two-Photon Gates

Implementing two-qubit gates poses a significant challenge due to the weak interaction between photons. This often necessitates achieving optical non-linearity, exemplified by the controlled phase-flip (CZ) gate. This gate operates on a pair of qubits, leaving the first qubit unchanged while flipping the sign of the second qubit only if the first qubit is in the $|1\rangle$ state. Consequently, it facilitates the following mapping: $|00\rangle \rightarrow |00\rangle$, $|01\rangle \rightarrow |01\rangle$, $|10\rangle \rightarrow |10\rangle$,

and $|11\rangle \rightarrow -|11\rangle$. A CZ gate, complemented with single-qubit gates, is equivalent to a CNOT gate, thereby also capable of generating quantum entanglement and composing the universal gate set. However, attaining strong optical non-linearity at the single-photon level poses a formidable challenge when using bulk optical materials.

Various approaches have been proposed to overcome this hurdle, and there's substantial progress in this regard. A typical strategy for implementing two-qubit gates in photonic quantum computing relies on using measurements to induce effective non-linearity. This involves configuring a setup where distinct measurement outcomes correspond to different effective interactions among the photons. The Linear Optical Quantum Computing (LOQC) strategy, proposed by Knill, Laflamme, and Milburn [53], employs ancillary photons to assist in the interaction. These supplemental photons, alongside the computational photons, are sent into an interferometric network comprised of beam splitters and phase shifters. Single-photon detectors are then used to measure the presence or absence of photons at the end of the network. When a measurement signals that a photon has been detected at a specific mode, this "collapses" the quantum state of the system, effectively implementing a CZ gate. However, since the success of the gate operation hinges on a specific measurement outcome and is probabilistic, further techniques like quantum error correction and quantum teleportation [53, 54] are often required to construct a scalable quantum computer using LOQC.

Measurement-Based Quantum Computing (MBQC) [13] is another approach to optical quantum computing. This method involves the creation of a highly entangled state of many photons, known as a cluster state. Then, by performing single-photon measurements on this state, quantum computations can be executed. The main challenge lies in the efficient generation of large and intricate photonic cluster states. However, the creation of a cluster state can be

achieved by employing LOQC [36] or fusion gates [39], which significantly reduce the overhead required to overcome the probabilistic nature of linear optics. The generation of a cluster state can also be executed deterministically by leveraging strong interactions between photons and atoms [38, 40, 43, 45], as demonstrated through cavity quantum electrodynamics [55]. These methods markedly enhance the scalability of optical quantum computing.

1.2.3 Minimal Hardware in Quantum Computing

Quantum computing is inherently resource-intensive, with the quest for fault-tolerance—designing and operating quantum computers that maintain accuracy despite component failures or errors—-exacerbating this demand. The achievement of such resilience typically requires quantum error correction protocols, where a logical qubit is encoded into a set of physical qubits, facilitating error detection and correction. Error-corrected quantum computation might necessitate hundreds or even thousands of physical qubits to encode a single logical qubit with a sufficiently low error rate [56]. Moreover, the complexity of practical problems targeted by quantum computers amplifies the required qubit count significantly. To run intricate quantum algorithms on a logically error-corrected and fault-tolerant quantum computer, we might require millions of physical qubits, manifesting the challenge of scaling across all quantum platforms.

Scaling quantum systems is indeed formidable, particularly in matter-based systems where the addition of qubits often calls for extensive modifications to the physical setup. As the number of quantum bits increases, the complexity of quantum control elevates. Furthermore, each new qubit or operation increases the probability of error due to susceptibility to environmental noise and interference. Thus, while the aim is to build larger quantum systems, a parallel objective is

to optimize hardware and resources to effectively manage these systems, harness the available technology to its full potential, and curtail error rates.

In contrast to many platforms, photonic quantum computing offers several potential advantages that could alleviate resource requirements. Photonic quantum computers do not necessitate ultra-low temperatures, obviating the need for elaborate cooling infrastructure. Their inherent noise resistance, due to limited environmental interaction, may curtail error rates and extend coherence times, thus moderating the demand for error correction. Photonic systems' scalability can be amplified by advancements in Photonic Integrated Circuits (PICs) [57], which allow for optical component miniaturization onto a single chip. Many core components, essential for quantum architectures, are compatible with PICs currently employed in classical computing and are under active exploration and optimization. Leveraging current manufacturing techniques and standards, such as CMOS technology, the arrival of PICs housing hundreds of thousands of components is imminent [47]. Moreover, photons are inherently apt for long-distance communication, making them ideal for distributed quantum computing. Photons can be produced in a highly modular manner, enabling any number of qubits to be created from a single device and facilitating universal gates between them. This property opens up the possibility of constructing large-scale computing infrastructures.

Finally, amalgamating photonic and matter-based qubits could offer considerable advantages [52]. Approaches that realize strong optical nonlinearity through single photon interactions with atoms are promising. This hybrid tactic could yield deterministic cluster states [38, 40, 42–45], further reducing linear optical quantum computing overhead. Additionally, employing atomic qubits as single-photon sources, capable of storing quantum information, could serve as a node or quantum repeater for implementing quantum networks.

1.3 Thesis Contributions and Outline

This thesis, which primarily builds upon my major contributions to journal articles [44, 58] and a preprint [59], focuses on optical quantum computing using an atom-photon interface.

Firstly, I delve into the generation of multi-dimensional cluster states, an essential resource for fault-tolerant measurement-based quantum computing. My approach, distinguishing itself from previous proposals, is deterministic and eliminates the need for feed-forward control. Moreover, it boasts hardware efficiency by requiring only a single interface and exhibits flexibility, as it can be readily extended to arbitrarily high dimensions. To complement this study, I introduce a diagrammatic method for deriving tensor networks of highly entangled optical states. This contribution offers a valuable tool for simulating matrix product states (MPS) [60–63] and projected entangled pair states (PEPS) [64, 65] generated from sequential photons.

Subsequently, I explore the optical quantum Fourier transform (QFT) implemented via an atom-photon interface. The proposed protocol leverages this interface to mediate photon-photon interactions, dramatically reducing the need for linear optical devices. Additionally, I propose a method for rapidly adjusting the atomic transitions [66, 67], thereby achieving arbitrary controlled phase-shift gates.

Finally, I scrutinize non-trace-preserving errors in realistic quantum systems. Conventionally, quantum operations are idealized as completely positive and trace-preserving (CPTP) maps [68]. However, real-world quantum systems do not always preserve the quantum particles in the computational subspace due to phenomena like photon loss. The process also involves state normalization, which is a nonlinear map. Despite its significance, the quantification of such errors has not received substantial attention. I aim to address this gap by studying these errors

and proposing a computationally efficient metric to quantify them. Importantly, this metric aligns with the fault-tolerant quantum computing theory [69, 70], underscoring its practical relevance.

As for the structure of this thesis, Chapter 2 discusses the physics of the atom-photon interface, exploring the dynamics of an atom inside a cavity (i.e., the Jaynes-Cummings model), along with the input-output formalism for external probe photons. Chapter 3 delves into the theoretical and experimental aspects of generating multi-dimensional cluster states and uses tensor network methods to estimate the fidelity of the produced cluster states. Chapter 4 elucidates how an atom-photon interface can mediate photon-photon interactions and implement controlled phase-shift gates, crucial components for executing the optical quantum Fourier transform. Finally, Chapter 5 provides a comprehensive discussion on an error metric for non-trace-preserving operations, presenting the general distance (an extension of the diamond distance), detailing its properties, and deriving an efficient algorithm to bound this general distance.

Chapter 2: Methodology: Atom-Photon Interface

2.1 Overview of Atom-Photon Interface

2.1.1 Bridging Stationary and Flying Qubits

In optical quantum computing, the crucial interaction between photons and atoms forms the basis of the atom-photon interface. Photons, the carriers of quantum information, excel at transmitting this information due to their speed and relative resilience to noise and decoherence. Atoms, acting as quantum memories or processing units, are ideal for storing and processing quantum information due to their long lifetimes and well-understood internal states. Together, they enable a mechanism for controlled exchanges between individual atoms and photons. This interface is central to actualizing quantum networks and computers, as it forms the essential bridge between stationary qubits (atoms) and flying qubits (photons) [71–77].

Harnessing the distinct advantages of both atoms and photons necessitates a robust and efficient atom-photon interface. Precise control over the atomic states and photon properties, along with their mutual interactions, is crucial for this purpose. To provide a comprehensive understanding, this chapter will delve into the importance, design, and applications of atom-photon interfaces within the context of optical quantum computing. The foundational methodology of this thesis, aimed at deterministically generating cluster states to enable measurement-based quantum

computing, will also be presented.

2.1.2 Atom-Photon Interface Applications

Atom-photon interfaces are pivotal across various sectors of quantum science and technology, providing essential capabilities for storing and manipulating quantum information. In one significant application, atom-photon interfaces enable the slowing, storing, and retrieval of light in a regulated manner [78]. The slowing of light arises from the dispersive properties of the atomic medium interacting with light under certain conditions. By adjusting atomic states, this effect can be carefully manipulated, paving the way for light storage. This storage mechanism, facilitated by the absorption and re-emission of a probe pulse without information loss through a principle known as Electromagnetically Induced Transparency (EIT) [79]. Building on this concept, atom-photon interfaces are not just instrumental for storing light but also for its efficient retrieval while preserving its quantum state. By an opposite process, the stored quantum state of light can be transformed back into a propagating photon. This crucial process, which safeguards the quantum information carried by light, is at the core of quantum memory devices and quantum repeaters' operation.

Moving beyond light storage and retrieval, atom-photon interfaces serve a critical role in the transfer of quantum states in quantum communication and computing. This process begins with the encoding of quantum information onto a stationary qubit, such as an atom, ion, or a spin in a solid. The encoded information is then transferred to a photonic qubit, capable of conveying quantum data over vast distances with minimal coherence loss. This transfer occurs through techniques like resonant fluorescence or Raman scattering [80], and, like the earlier stages, relies

heavily on atom-photon interactions. This ability to establish and manipulate atom-photon and atom-atom entanglement has significant implications for distributed quantum computing architectures [81].

Despite the challenges posed by atoms' propensity to emit photons spontaneously and randomly, atom-photon interfaces provide a viable solution to create single-photon sources, which are fundamental for quantum communication, cryptography, and computing. By manipulating the emission process, atom-photon interfaces can help create a deterministic single-photon source. One approach involves engineering the atom's environment to enhance the likelihood of photon emission into a specific mode, an effect known as the Purcell effect.

Taking the utility of atom-photon interfaces even further, they serve as the foundation for optical quantum gates. Through controlled atomic and photonic interactions, these interfaces enable both single-qubit and two-qubit gates. Single-qubit gates can perform elementary quantum operations on atoms via methods like Raman transitions or resonant interactions. For more complex two-qubit gates, entangling operations are crucial. The common approach uses the controlled phase shift acquired by a photon interacting with an atom, creating a controlled-Z gate. This gate enables entanglement of the atomic state with the photonic state, serving as a critical resource for quantum information processing.

Finally, in the realms of quantum sensing and metrology, atom-photon interfaces make ultra-precise measurements possible. By coupling photons to atomic states that respond to external fields, atom-photon interfaces allow for measurements beyond classical limits. They are also integral to optical clocks for ultra-precise time measurement and magnetometry for detecting perturbations in atomic energy levels induced by magnetic fields [82]. Thus, atom-photon interfaces, with their varied applications, are an essential tool in the quantum science and technology

toolkit.

2.1.3 Technologies for Atom-Photon Interfaces

Several techniques and strategies are available for implementing atom-photon interfaces, each with unique characteristics and benefits. One such technique involves atomic ensembles, which consist of many ultra-cold atoms. These ensembles are an effective platform for atom-photon interfaces due to the amplification of light-matter interactions that result from collective atomic behavior. The Duan-Lukin-Cirac-Zoller (DLCZ) protocol [83] leverages these atomic ensembles, utilizing photon interference to store and retrieve quantum information. Additionally, when photons emitted from two separate ensembles interfere and are detected, entanglement between the ensembles can occur, a property key to quantum repeaters. However, atomic ensembles present challenges in identifying individual atoms within the group and maintaining coherence among a large number of atoms.

Transitioning from atomic ensembles to individual atoms, another approach uses trapped ions or ultra-cold neutral atoms. Trapped ions are laser-cooled and confined within an electromagnetic field, with quantum information typically stored in the ions' electronic states, which can be manipulated using laser or microwave radiation. Similarly, ultra-cold neutral atoms trapped in optical lattices - arrays of microscopic traps created by standing waves of laser light - can also serve as quantum registers, where each atom functions as a qubit.

Complementing these techniques, semiconductor quantum dots and color centers in diamonds offer additional strategies that leverage naturally trapped atoms within an atomic lattice. Semiconductor quantum dots, capable of confining individual electrons and holes, allow for state

control either electrically or optically [84–86]. Furthermore, when placed within a photonic cavity, the coupling with photons can be significantly enhanced. Meanwhile, color centers in diamonds arise from lattice defects, such as a carbon atom being replaced by another atom like nitrogen. These color centers, which can be individually addressed and manipulated using light and microwaves, serve as effective tools for storing and processing quantum information.

Lastly, cavity quantum electrodynamics (QED) systems provide another route for creating atom-photon interfaces [87]. These systems trap atoms or ions in an optical or microwave resonator cavity. Due to the high quality factor of these cavities, strong coupling between atoms and photons is achievable, allowing a photon to be absorbed and re-emitted many times before it's lost. Techniques in cavity QED, such as the Jaynes-Cummings model where a two-level atom interacts with a single mode of a radiation field in a cavity, have been instrumental in demonstrating quantum gates and entanglement. Thus, in the broader perspective of atom-photon interfaces, these methods present exciting possibilities for the development of quantum technologies.

2.2 Cavity Quantum Electrodynamics Model

2.2.1 Electron-Charged Quantum Dots in Cavity

We consider a solid-state spin qubit (alternatively termed an atomic qubit or atom) that is coupled to a photonic cavity [72], as illustrated in Figure 2.1. This spin qubit consists of a single-electron-injected quantum dot. A magnetic field, applied in the Voigt configuration such that it is perpendicular to the direction of light propagation, is used to break the spin degeneracy, and we diagonalize the quantum states of the system along the magnetic field's direction.

The energy level structure of the quantum dot, depicted in Figure 2.2, encompasses two

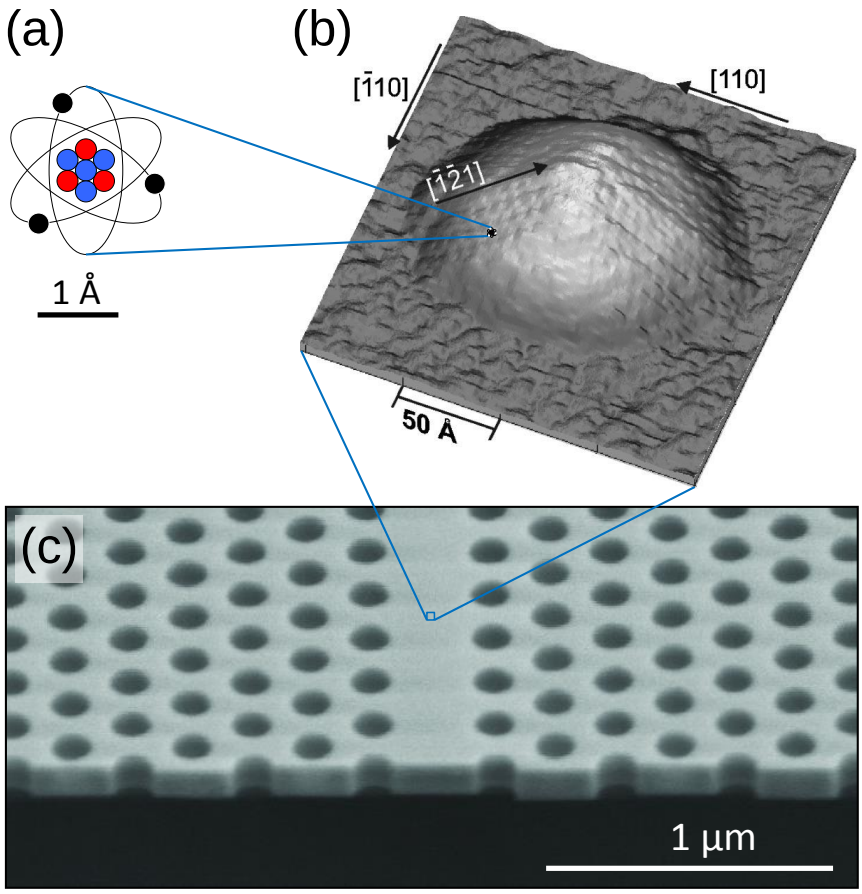

Figure 2.1: Characteristic size of a quantum dot relative to a single atom and a photonic crystal. (a) A single atom measures a few angstroms. (b) Self-assembled InGaAs quantum dots, consisting of roughly 10^5 atoms, span across tens of nanometers. These single quantum dots can be embedded in photonic nanostructures for quantum-optics experiments. (c) A photonic-crystal waveguide is depicted, characterized by a photonic lattice constant typically measuring around $250\,\mathrm{nm}$. Figure reprinted with permission from [88].

ground states, each with opposing electron spin, forming a stable quantum memory [89], denoted as $|\uparrow\rangle$ and $|\downarrow\rangle$. Additionally, it includes two excited states, each housing a pair of electrons and a single hole with opposite spins, labeled as $|\Uparrow\rangle$ and $|\Downarrow\rangle$. In this setup, all four transitions are possible. However, the polarization of transitions σ_1 and σ_4 is orthogonal to that of transitions σ_2 and σ_3 due to the selection rule. Transitions σ_2 and σ_3 serve to apply single-qubit rotation on the atom [86], whereas transitions σ_1 and σ_4 can be utilized to create an entangling gate between the atom and photons. Specifically for entangling the atom and a reflected photon, we consider the atom's interaction with the cavity mode polarized along the quantization axis (V polarization), which only couples to transitions σ_1 and σ_4.

The internal Hamiltonian of the atom-cavity system, with respect to transitions σ_1 and σ_4, is expressed as:

$$\frac{\hat{H}}{\hbar} = \omega_c \hat{a}^\dagger \hat{a} + \omega_\uparrow \hat{\sigma}_{\Uparrow\Uparrow} + \omega_\downarrow \hat{\sigma}_{\Downarrow\Downarrow} + ig\left(\hat{\sigma}_{\Uparrow\uparrow}\hat{a} - \hat{\sigma}_{\uparrow\Uparrow}\hat{a}^\dagger + \hat{\sigma}_{\Downarrow\downarrow}\hat{a} - \hat{\sigma}_{\downarrow\Downarrow}\hat{a}^\dagger\right) . \tag{2.1}$$

In the above equation, g denotes the atom-cavity coupling strength. ω_c represents the frequency of the cavity mode, and $\hat{a}$ is the annihilation operator for the cavity mode in V polarization. The spin operator is represented by $\hat{\sigma}$, with its state space reduced to two uncoupled subspaces $\{|\uparrow\rangle, |\Uparrow\rangle\}$ and $\{|\downarrow\rangle, |\Downarrow\rangle\}$, and notation $\hat{\sigma}_{\uparrow\Uparrow}$ is interpreted as operator $|\uparrow\rangle\langle\Uparrow|$, etc. $\omega_\uparrow$ and $\omega_\downarrow$ are the transition frequencies of $|\uparrow\rangle \leftrightarrow |\Uparrow\rangle$ and $|\downarrow\rangle \leftrightarrow |\Downarrow\rangle$, respectively. It is assumed that the spin-up transition is in resonance with the frequency of the cavity mode, which implies $\omega_\uparrow = \omega_c$, and the spin-down transition is detuned by the Zeeman splitting, represented as $\Delta_Z = \omega_\downarrow - \omega_\uparrow$. Note that the Hamiltonian can be viewed as the Jaynes-Cummings model under the rotating wave approximation, where a single bosonic mode is concurrently coupled to two distinct fermionic

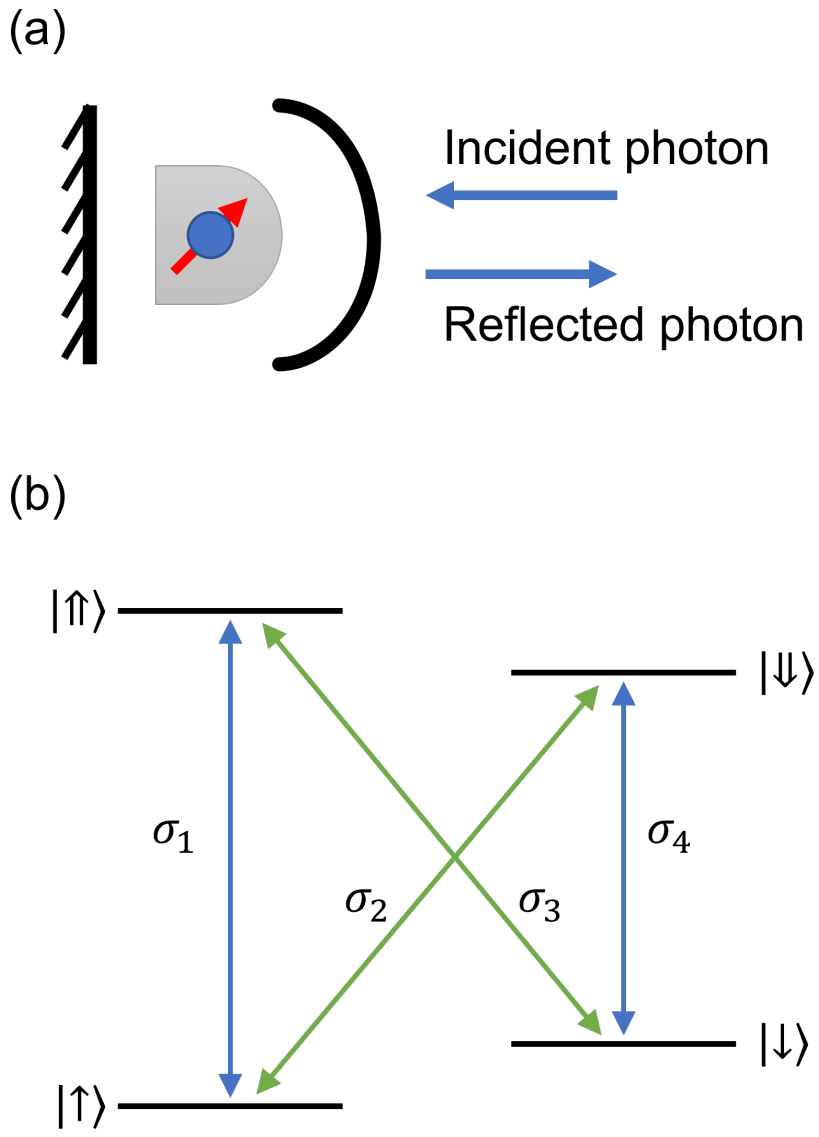

Figure 2.2: Diagram illustrating the atom-photon interface. (a) Depicts a single-sided cavity encapsulating a spin quantum made of an electron-injected quantum dot, enabling the control of phase shift in incident photons via reflection. (b) Illustrates the energy level structure of a charged quantum dot under a magnetic field. This structure comprises two spin ground states and two excited trion states, with four allowed optical transitions labelled σ_1 to σ_4.

modes.

The atom-cavity system is coupled both to the external probe field through a transmitting mirror and to a reservoir. This results in the Heisenberg equations of motion defined within either subspace, as shown below:

$$\begin{aligned}
\frac{d\hat{a}}{dt} &= -\left[i\left(\omega_c - \omega\right) + \frac{\gamma}{2}\right]\hat{a} - g\hat{\sigma}_- - \sqrt{\gamma}\hat{a}_{\text{in}}\ , \\
\frac{d\hat{\sigma}_-}{dt} &= -\left[i\left(\omega_{\uparrow,\downarrow} - \omega\right) + \frac{\kappa}{2}\right]\hat{\sigma}_- - g\hat{\sigma}_z\hat{a}\ , \\
\hat{a}_{\text{out}} &= \hat{a}_{\text{in}} + \sqrt{\gamma}\hat{a}\ .
\end{aligned} \tag{2.2}$$

Without loss of generality, we will consider the subspace of $\{|\uparrow\rangle\,, |\Uparrow\rangle\}$. In these equations, $\hat{\sigma}_- = \hat{\sigma}_{\uparrow\Uparrow}$ and $\hat{\sigma}_z = |\Uparrow\rangle\langle\Uparrow| - |\uparrow\rangle\langle\uparrow|$. The terms $\hat{a}_{\text{in}}$ and $\hat{a}_{\text{out}}$ represent the input and output field operators for the probe beam, respectively. The probe beam frequency is denoted by ω, and is set to be equal to ω_c. The decay rate of the excited atom is denoted by κ, and the decay rate of the cavity mode is denoted by γ. For a detailed derivation of the Heisenberg equations of motion, please refer to Appendix 2.A.

2.2.2 Controlled Phase-Flip Gate

The state-dependent phase shift is experienced by the probe beam. When the probe beam exhibits H-polarization, it does not interact with the cavity, but rather reflects off a mirror without acquiring any phase shift. Conversely, the probe beam reflects off the cavity when in V-polarization. Given the adiabatic limit, where the probe beam's envelope alters very slowly compared to the frequency of the system dynamics, the derivatives of the operators $d\hat{a}/dt$ and $d\hat{\sigma}_-/dt$ can be approximated as zero. Moreover, for a large decay represented by κ, the atom state can

be approximated as $\hat{\sigma_z} = -1$. As a result, the equation of motion can be solved analytically, yielding:

$$\hat{a}_{\text{out}} = \frac{4g^2 - \gamma(\kappa + i2\Delta_{\uparrow,\downarrow})}{4g^2 + \gamma(\kappa + i2\Delta_{\uparrow,\downarrow})}\hat{a}_{\text{in}} \ , \tag{2.3}$$

where $\Delta_{\uparrow,\downarrow} = \omega_{\uparrow,\downarrow} - \omega$ is denoted, and $\omega_c = \omega$ is set. The equation formulates the reflection coefficient of the probe beam reflected from an atom-coupled cavity.

To facilitate comprehension, we define the atom-cavity cooperativity as follows:

$$C_{\uparrow,\downarrow} = \frac{4g^2}{\gamma(\kappa + i2\Delta_{\uparrow,\downarrow})} \ . \tag{2.4}$$

As a consequence, the reflection coefficient is given by:

$$r_{\uparrow,\downarrow} = \frac{C_{\uparrow,\downarrow} - 1}{C_{\uparrow,\downarrow} + 1} \ . \tag{2.5}$$

The atom-cavity cooperativity is a frequently utilized measure in cavity QED, indicating the strength of coupling between the atom within and the cavity mode. The strong coupling regime is defined by the interaction strength between the cavity photons and the atom exceeding their individual decay rates, γ and κ. In this regime, light and matter can interact coherently over multiple periods, enabling precise manipulation of quantum states. To achieve strong coupling in cavity QED, it's necessary to engineer the cavity and atom in a way that maximizes their interaction strength. This is usually achieved by enhancing the quality factor (Q) of the cavity, which essentially measures its capacity to store energy, and by meticulously aligning the cavity's resonance frequency with the transition frequency of the atom.

Let us define the state of the incident light as $|H\rangle \equiv |0\rangle_p$ for an H-polarized photon and

$|V\rangle \equiv |1\rangle_p$ for a V-polarized photon. Similarly, we label the spin states as $|\uparrow\rangle \equiv |0\rangle_a$ and $|\downarrow\rangle \equiv |1\rangle_a$. The state of the entire system, denoted as $|\psi\rangle = |x\rangle_p \otimes |y\rangle_a$, where x and y represent the qubit states of the photon and spin, respectively, transforms according to the following operator:

$$U_r = \begin{pmatrix} 1 & 0 & 0 & 0 \\ 0 & 1 & 0 & 0 \\ 0 & 0 & r_\uparrow & 0 \\ 0 & 0 & 0 & r_\downarrow \end{pmatrix}. \tag{2.6}$$

Assuming strong coupling between the cavity and atom, where $g \gg \gamma, \kappa$, the spin-up transition resonates with the frequency of the cavity mode. As such, $C_\uparrow \gg 1$ and $r_\uparrow = 1$. Considering the spin-down transitions, which are detuned by the Zeeman splitting ($\Delta_\downarrow = \Delta_Z$), we assume a large detuning, which results in $C_\downarrow \ll 1$ and $r_\downarrow = -1$. Therefore, the reflection operator applies the controlled phase-flip gate.

2.2.3 Coherent Time-Delay Feedback Control

Coherent time-delay feedback control [90–96] can act as a significant augmentation to cavity quantum electrodynamics (QED), strengthening the atom-photon interface. It's well established that single- or multi-body states can be prepared by the emission of photons [38]. However, photons emitted through sequential processes typically generate entanglement in a one-dimensional fashion, thus producing states with limited functionality [60]. Notably, preparing complex multi-body states, essential for advanced quantum simulations [64] and universal quantum computing [43], presents substantial challenges within single cavity QED systems.

This complexity emerges from the Markovian characteristics of sequential emission processes, which substantially limit the types of states that can be achieved. Within the Markovian limit, the interaction between atoms and photons is generally describable by a master equation that essentially ignores quantum memory. In contrast, a characteristic non-Markovian open quantum system arises when a photon emits into a feedback reservoir. This reservoir preserves the system's memory, subsequently feeding this information back coherently following one or more discrete time delays. As such, delayed quantum feedback makes the system non-Markovian, introducing effective quantum memory and expanding the system into a larger Hilbert space.

Cavity quantum electrodynamics (QED) systems are particularly suitable for time-delay feedback control. Through the use of reflective mirrors, various cavity input and output channels can effectively couple light into the feedback loop, connecting these channels. This setup allows quantum information to re-enter the system after a time delay. By linking multiple distant atoms with a photonic waveguide, or associating a single atom with its output field using a time-delay loop, a photonic arrangement with feedback control can be established.

This coherent time-delay feedback control has the potential to stabilize optical systems. For instance, such feedback can maintain a specific level of coherence in a two-level system embedded in a cavity, even at finite temperatures [97]. A single-emitter-cavity system operating under weak coupling can transition into a strongly coupled system through the introduction of time-delay feedback [98]. This mechanism can also amplify the optical squeezing characteristics of a degenerate parametric amplifier [99]. By leveraging multi-photon scattering and time-delay feedback, an uncoupled bound state within the continuum can be excited [100]. Additionally, it can boost the energy-time entanglement of photons in a Franson interferometer [101]. This form of coherent time-delay feedback control can also generate resources for quantum entanglement

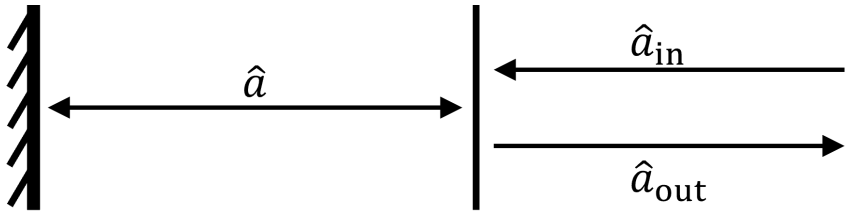

Figure 2.3: Schematic diagram of the cavity field along with the input and output fields for a single-sided cavity.

and facilitate the realization of universal quantum computing [43–45].

Appendix 2.A Derivation of Heisenberg Equations of Motion

We adopt the discourse from [102] and consider the single-side cavity structure illustrated in Figure 2.3. The external field operator, denoted as $b(t) = b(x > 0, t)$, captures the input-output fields. Given the confinement of the cavity within a specific region of space, it is necessary to determine how the field outside the cavity responds to the cavity's presence and any matter contained within.

The interaction Hamiltonian, as it pertains to the cavity field, is symbolized by the harmonic oscillator annihilation and creation operators a and $a^\dagger$, respectively. Within the rotating wave approximation, the interaction with the external field is defined as:

$$V = -i\hbar \int_{-\infty}^{\infty} g(\omega)[ab^\dagger(\omega) - a^\dagger b(\omega)]d\omega \ . \tag{2.7}$$

In this equation, $g(\omega)$ symbolizes the frequency-dependent coupling strength, typically peaking around ω. If the cavity contains matter, this may lead to complex dynamics within the field inside the cavity, thereby causing the external fields to diverge from the dynamics of the free field. This divergence, in turn, prompts an explicit time dependence in the frequency space operators,

$b(t,\omega)$, within the Heisenberg picture.

The Heisenberg equation of motion for b, defined as $\dot{b}(t,\omega) = -i[V/\hbar, b(t,\omega)]$, within the interaction picture, is:

$$\dot{b}(t,\omega) = -i\omega b(t,\omega) + g(\omega)a(t) \ . \tag{2.8}$$

Depending on whether we choose to solve in terms of the input at a time $t_0 < t$ or in terms of the output at a time $t_1 > t$, the solution to this equation can be written in two ways:

$$b(t,\omega) = e^{-i\omega(t-t_0)}b_0(\omega) + g(\omega)\int_{t_0}^{t} e^{-i\omega(t-t')}a(t')dt' \ , \tag{2.9}$$

$$b(t,\omega) = e^{-i\omega(t-t_1)}b_1(\omega) - g(\omega)\int_{t}^{t_1} e^{-i\omega(t-t')}a(t')dt' \ . \tag{2.10}$$

The boundary conditions $b_0(\omega)$ and $b_1(\omega)$ are typically specified at $-\infty$ and $+\infty$, respectively, corresponding to times when the field is a free field.

The cavity field operator is defined by the equation:

$$\dot{a}(t) = -i\left[\frac{H}{\hbar}, a(t)\right] - \int_{-\infty}^{\infty} g(\omega)b(t,\omega)d\omega \ , \tag{2.11}$$

where H is the Hamiltonian of the cavity. Given the solution with initial conditions 2.9, this equation becomes:

$$\begin{aligned}\dot{a}(t) = -i\left[\frac{H}{\hbar}, a(t)\right] &- \int_{-\infty}^{\infty} g(\omega)e^{-i\omega(t-t_0)}b_0(\omega)d\omega \\ &- \int_{-\infty}^{\infty} g^2(\omega)\int_{t_0}^{t} e^{-i\omega(t-t')}a(t')dtd\omega \ .\end{aligned} \tag{2.12}$$

We now assume that $g(\omega) = g$ is frequency-independent over a wide range of frequencies sur-

rounding the carrying frequency. This assumption is the first approximation needed to derive a Markov quantum stochastic process. Consequently, we set $g^2 = \gamma/2\pi$. The input field is defined by the external field at t_0 as:

$$a_{\text{in}}(t) = \frac{1}{\sqrt{2\pi}} \int_{-\infty}^{\infty} e^{-i\omega(t-t_0)} b_0(\omega) d\omega \ . \tag{2.13}$$

At the limit of an integral involving a function that smoothly approaches zero at $\pm\infty$ (for example, a Gaussian function), the following result holds:

$$\int_{t_0}^{t} f(t')\delta(t-t')dt = \int_{t}^{t_1} f(t')\delta(t-t')dt = \frac{1}{2} f(t) \ . \tag{2.14}$$

By interchanging the sequence of time and frequency integration in the last term of equation 2.12 and employing equation 2.14, we obtain:

$$\dot{a}(t) = -i \left[\frac{H}{\hbar}, a(t) \right] - \frac{\gamma}{2} a(t) - \sqrt{\gamma} a_{\text{in}}(t) \ . \tag{2.15}$$

In a similar manner, the time-reversed equation of motion, obtained by substituting the solution in terms of the final conditions 2.10 into 2.11, is:

$$\dot{a}(t) = -i \left[\frac{H}{\hbar}, a(t) \right] + \frac{\gamma}{2} a(t) + \sqrt{\gamma} a_{\text{out}}(t) \ . \tag{2.16}$$

The output field operator is expressed as:

$$a_{\text{out}}(t) = -\frac{1}{\sqrt{2\pi}} \int_{-\infty}^{\infty} e^{-i\omega(t-t_1)} b_1(\omega) d\omega \ . \tag{2.17}$$

It's worth noting that the negative sign in the above equation encapsulates the boundary condition of the phase shift observed in the reflected light. Consequently, the input and output fields are related as follows:

$$a_{\text{in}}(t) + a_{\text{out}}(t) = \sqrt{\gamma} a(t) \ . \tag{2.18}$$

Dynamic terms between the input and the cavity field also contribute to the output field. A similar analysis can be applied to the equation of motion for the atom in the cavity, considering the atom's interaction with numerous bosonic modes as a reservoir. This interaction accounts for the atomic decay.

Chapter 3: Multi-Dimensional Optical Cluster State Generation

3.1 Cluster-State Quantum Computing

Measurement-based quantum computing (MBQC) [13] offers a revolutionary approach for quantum computing, that vastly differs from the standard gate model. Instead of executing sequences of unitary operations on a small number of qubits, MBQC leverages entanglement as a computational resource, operating primarily through single-qubit measurements. The initial state of the system, often referred to as the resource state, is an entangled state of multiple qubits, typically in the form of a cluster state. Hence, MBQC is also commonly known as cluster-state quantum computing [103]. Upon preparation of this state, the quantum computation is carried out by performing a series of single-qubit measurements. Each measurement's outcome not only reads out results but also determines the basis for subsequent measurements. The computational task accomplished hinges on the specific order and basis of these measurements.

3.1.1 What is a Cluster State?

Within the context of cluster-state quantum computing, a cluster state functions as a multi-qubit entangled state [12], providing the core computational resource. It can be envisioned as a "quantum graph" [104], depicted in Figure 3.1. Here, each vertex stands for a physical qubit,

with edges (or bonds) denoting the entanglement between qubits.

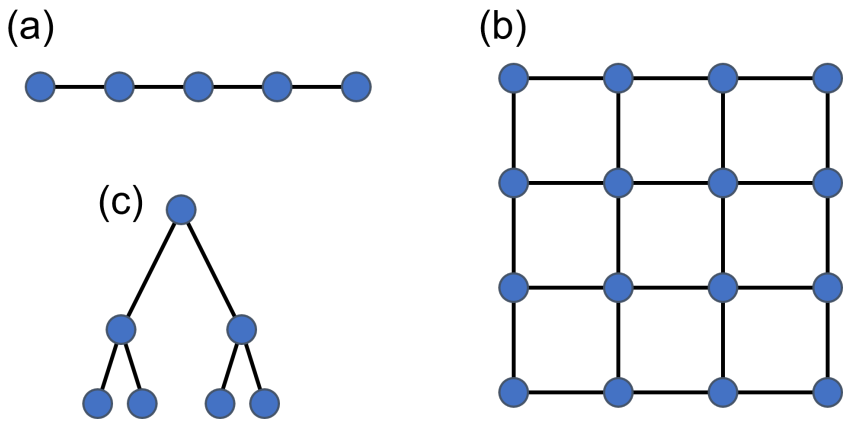

Figure 3.1: Representation of one-dimensional (a) and two-dimensional (b) cluster states. (c) Depicts a tree-level graph state, which retains properties of cluster states but exhibits different topology.

Take, for instance, a five-qubit cluster state as illustrated in Figure 3.1(a). Starting from an initial state $|+\rangle^{\otimes 5}$, where $|+\rangle = \frac{1}{\sqrt{2}}(|0\rangle + |1\rangle)$ symbolizes the superposition of computational basis, the entanglement bonds are built by implementing CZ gates between pairs of neighboring qubits. The CZ gate is defined as $|0\rangle\langle 0| \otimes I + |1\rangle\langle 1| \otimes Z$, functioning as a two-qubit gate that flips the phase of the target qubit based on the state of the control qubit. It's noteworthy that the order of CZ gate implementation bears no impact, since these gates are commutative. More generally, cluster states of various topologies can be constructed following a similar process. These states showcase a type of long-range entanglement, resilient to local disturbances, making them ideally suited for quantum computation and error correction.

3.1.2 Universality of Cluster-State Quantum Computing

The universality of cluster-state quantum computing represents a fundamental facet of its potential. To establish this universality, one must demonstrate that any quantum computation can

be efficiently executed via cluster-state quantum computing. Central to this assertion is the understanding that any quantum circuit composed of single-qubit rotations and two-qubit controlled phase-flip gates can be implemented within the cluster model. To illustrate this, we can simulate a universal quantum circuit using a simplified cluster state scheme suggested by Nielsen [36]. This scheme is functionally equivalent to the original one-way quantum computing model proposed Raussendorf, et al. [105].

Figure 3.2(a) illustrates a two-qubit circuit for universal quantum computing. For simplicity and without loss of generality, we take the input states to be $|+\rangle \otimes |+\rangle$. Here, $\hat{R}_z(\theta)$ signifies a single-qubit rotation by an angle θ around the z-axis, whereas $\hat{R}_x(\theta)$ denotes rotation around the x-axis. According to Euler's theorem, an arbitrary rotation on the Bloch sphere — that is, an SU(2) operator — can be decomposed into z-x sequences such that $\hat{U} = e^{i\alpha}\hat{R}_z(\beta)\hat{R}_x(\gamma)\hat{R}_z(\delta)$, where α, β, γ, and δ are real numbers. The vertical line with dotted ends symbolizes a CZ gate. As the Solovay-Kitaev theorem [14] demonstrates the universality of single-qubit rotations and the CZ gate for quantum computation, it naturally follows that the depicted circuit is universal.

To simulate the quantum circuit, we initially prepare a cluster state as depicted in Figure 3.2(b). Here, each circle represents a physical qubit, and each edge denotes entanglement between the corresponding qubits. The universality of the cluster-state quantum computing necessitates at least two-dimensional (2D) cluster states. The horizontal line signifies the transition of a logical qubit, while the vertical line represents the crosstalk among logical qubits. Following this setup, the simulation proceeds with a sequence of single-qubit measurements from left to right, as illustrated in Figure 3.2(c). For each qubit, we measure the observable $\cos(\theta)\hat{\sigma}_x + \sin(\theta)\hat{\sigma}_y$, with the angle θ represented by the symbols inside the circle. It should be noted that the sign of these angles is contingent on the measurement outcomes of its left neighboring qubits, barring those

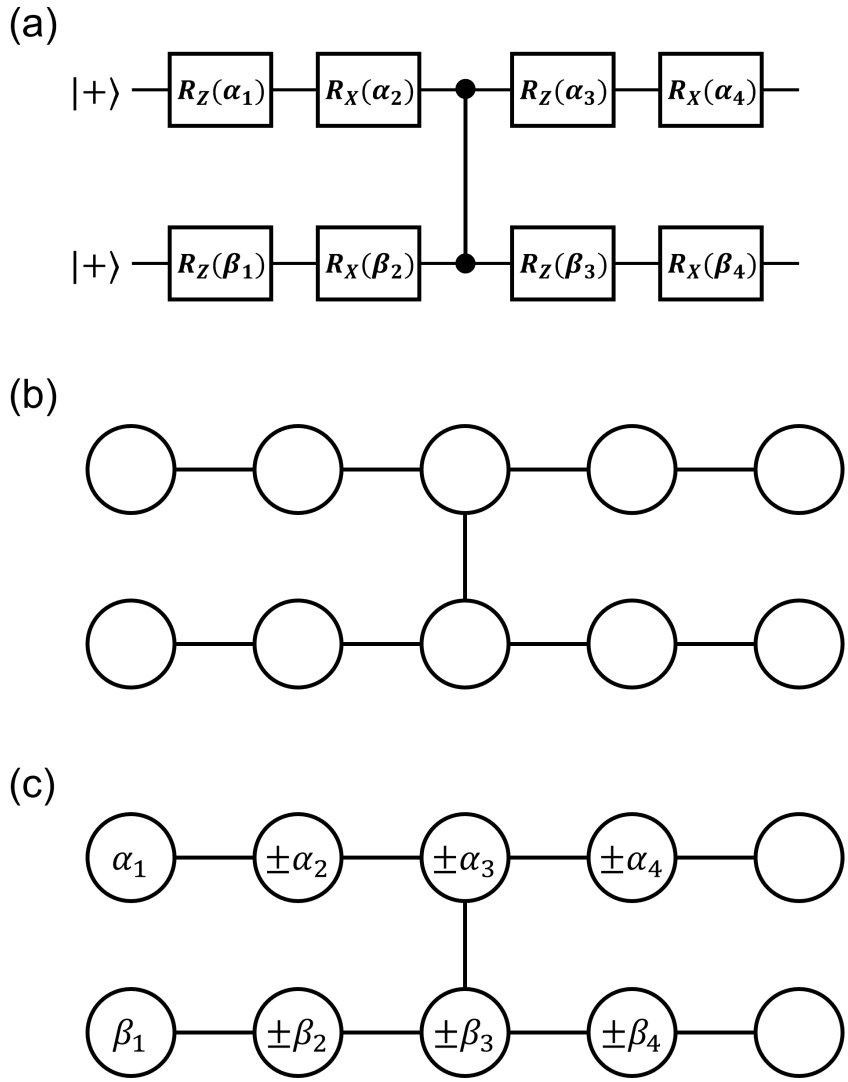

Figure 3.2: (a) A universal two-qubit circuit for quantum computing, featuring the single-qubit gate $R_{\mathrm{X(Z)}}(\theta)$ representing a rotation by θ along the $X(Z)$-axis of the Bloch sphere. The dotted line indicates a controlled phase-flip gate. (b) The cluster state simulating the circuit from (a). Each circle denotes a single qubit. (c) The simulation process involves a series of single-qubit measurements on the cluster state. Each measures the observable $\cos(\theta)\sigma_x + \sin(\theta)\sigma_y$, with angle θ indicated by symbols within the circle. The angle's sign depends on the measurement outcomes of its left qubits, excluding the first column. The unmeasured qubits on the rightmost side represent the quantum circuit's outcome.

in the first column. The unmeasured cluster qubits on the far right constitute the output from the quantum circuit. It is straightforward to verify that these output states result from applying the desired quantum circuit to the input states. In order to simulate more complex circuits, one can construct larger cluster states by arranging universal blocks. To achieve specially interconnected cluster states, redundant qubits can be measured in the computational basis and subsequently removed from the overarching cluster state.

3.1.3 Fault-Tolerance and Cluster State Dimensionality

The dimensionality of cluster states is crucial in both universal and fault-tolerant MBQC. For universal MBQC, a two-dimensional (2D) cluster state suffices to enable universal quantum computing within the MBQC framework. To exemplify, a basic square lattice cluster state can execute any quantum circuit composed of single-qubit rotations and two-qubit controlled-phase gates, given an appropriately chosen sequence of measurements.

In contrast, the requirements shift considerably when aiming for fault-tolerant MBQC. Quantum error correction necessitates an increase in dimensionality [106]. Topological error correction codes, frequently utilized in fault-tolerant MBQC, typically require cluster states that can be conceptualized as three-dimensional (3D) structures. In this 3D configuration, one dimension often symbolizes time, encapsulating the evolution of the computation, while the other two dimensions depict a 2D lattice of qubits, akin to a surface code, at a specific temporal stage. The logical qubits within the surface code are represented by distinct topological features of the state, such as the loops in the lattice, rather than individual physical qubits. Therefore, local errors that impact only a limited number of qubits can be corrected without compromising the information

stored in the logical qubits.

3.1.4 Review on the Generation of Photonic Cluster States

The probabilistic generation of photonic cluster states has seen significant advancements in recent years. Nielsen [36] developed an approach to optical quantum computation, amalgamating the Knill-Laflamme-Milburn (KLM) scheme [53] with the one-way quantum computing [13]. Browne and Rudolph [39] introduced a fusion gate that leverages parity measurements of maximally entangled photon pairs to generate cluster states efficiently. Gimeno-Segovia et al. [41] proposed a scheme that utilizes 3-qubit GHZ states to generate cluster states, exhibiting resilience to photon loss and surpassing the efficiency of previous proposals. Bodiya and Duan [107] suggested a method for constructing graph states efficiently using linear optics, imperfect photon sources, and single-photon detectors. Walther et al. [108] reported the first proof of principle experiment of one-way quantum computing, realizing four-qubit cluster states encoded into the polarization state of four photons and showcasing Grover's search algorithm [5] using these states. Subsequently, Lu et al. [109] conducted an experiment that successfully generated six-photon graph states.

In the field of deterministic generation of photonic cluster states, Lindner and Rudolph [38] proposed a method to manipulate a single photon emitter into a device capable of emitting long strings of photonic cluster states in an on-demand manner. Economou et al. [40] presented an approach to generate a two-dimensional cluster state of polarization encoded photonic qubits from two coupled quantum dot emitters. Pichler et al. [43] suggested and analyzed a deterministic protocol to generate two-dimensional photonic cluster states using a solitary quantum emitter via

time-delay feedback. Dhand et al. [110] investigated an all-optical scheme for generating one-dimensional and higher-dimensional tensor network photonic states encoded in temporal modes of light. Gimeno-Segovia et al. [42] proposed a method for deterministic generation of large-scale entangled photonic cluster states from interacting solid-state emitters. Experiments for deterministic generation of 1D cluster states have been reported using both trapped ions [111] and quantum dots [55, 112].

3.2 Protocol for 3D Cluster State Generation with Time-Delay Feedback

In cluster-state quantum computing, preparing optical cluster states is a critical step. Although single-qubit measurements are relatively straightforward with photons, generating optical cluster states presents a significant challenge because photons do not directly interact with each other. In this section, I will explore the potential of an atom-photon interface in facilitating the creation of optical cluster states [44]. Specifically, I will propose a protocol to generate 3D cluster states using time-delay feedback. Subsequently, I will generalize this protocol to accommodate any multi-dimensional cluster state, where the dimensionality of the states increases linearly with the number of time-delay feedback loops.

3.2.1 3D Lattice Linearization

A 3D cluster state can be delineated on a 3D lattice, where nodes represent qubits (photons, in this case), and edges signify the entanglement between photons. Figure 3.3(a) depicts a cluster state on a cuboid lattice with dimensions $N \times M \times L$. Each photon within the lattice can be assigned a unique coordinate (n, m, l) based on its row (n), column (m), and layer (l) position.

We then label it (k) using the following formula:

$$k = (l-1)\,MN + (m-1)\,N + n. \tag{3.1}$$

In this schema, the entanglement of photon k with its nearest neighbors, $k-1$, $k-N$, and $k-MN$, defines the unit cell of the 3D lattice.

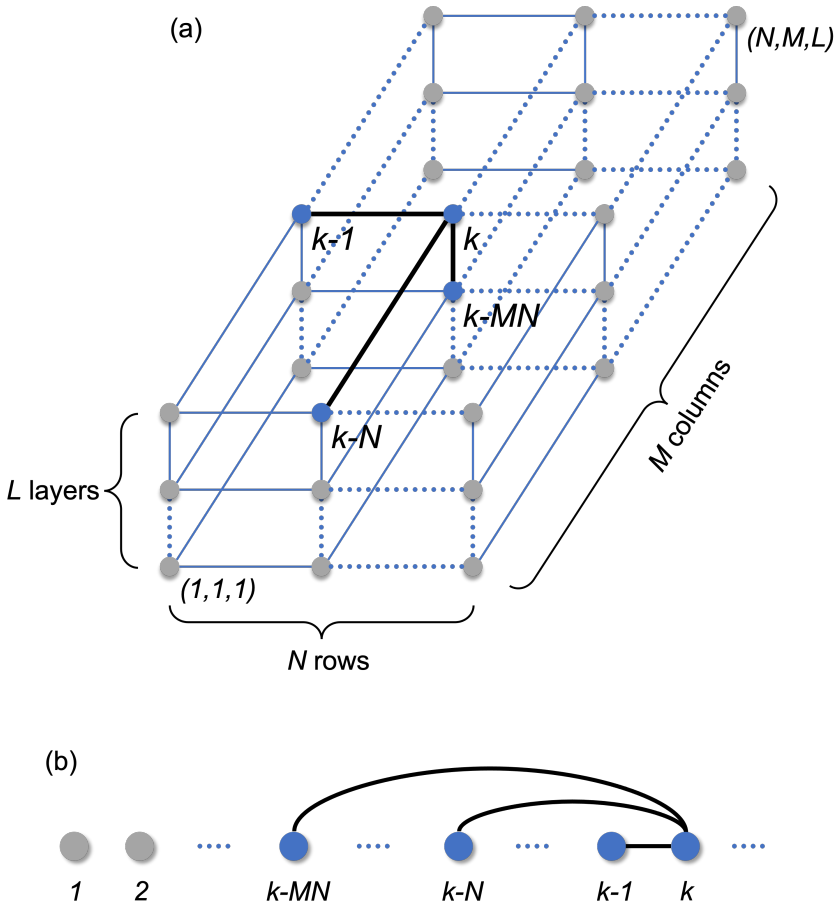

Figure 3.3: (a) Depicts the schematic of a 3D cluster state structured on a cuboid lattice. Each node represents a photon, with edges between nodes represent entanglement. The entanglement of photon k with its nearest neighbors $k-1$, $k-N$, and $k-MN$ define the system's unit cell. (b) Demonstrates the reconfiguration of the 3D lattice into a linear chain.

Given that photons are 'flying' qubits, a fixed 3D lattice structure is less conducive to generating a photon-based 3D cluster state. Therefore, we propose an alternative: rearranging the

lattice into a linear chain. To transform the 3D lattice into a linear chain, we sequentially list the photons by their label k, as depicted in Figure 3.3(b). This configuration results in photons exhibiting a mix of both nearest and non-nearest neighbor entanglement within the chain. For instance, photon k from the unit cell is entangled with its nearest neighbor photon $k-1$, whereas photons $k-N$ and $k-MN$ are now classified as non-nearest neighbors. Nevertheless, the generation of this entanglement between nearest and non-nearest neighbors within the linear photon sequence poses a substantial challenge, especially considering that photons cannot directly interact with each other.

3.2.2 Building Nearest-Neighbor Entanglement

Nearest-neighbor entanglement between photons can be facilitated through the sequential application of controlled phase-flip (CZ) gates with the aid of an ancilla, i.e., an atomic qubit. Figure 3.4(a) demonstrates how an ancilla can generate a 1D cluster among a series of periodically spaced photons with a uniform delay time T_{cycle} (equivalent to one clock cycle). The photons, symbolized by blue circles, travel from right to left and are adequately separated to ensure they interact with the ancilla individually and sequentially. Each photon is initialized to the state $|+\rangle = \frac{1}{\sqrt{2}}(|0\rangle + |1\rangle)$, where $|0\rangle$ and $|1\rangle$ denote the computational basis. The atom-photon interface applies a CZ gate to each photon, thus creating an entanglement between the photon and the atom (for a detailed explanation, refer to Section 2.2.2). This step is succeeded by the application of Hadamard gates, as depicted in Figure 3.4(b). When CZ and Hadamard gates are sequentially imposed in this fashion on photons k and $k+1$, they generate an effective CZ gate between the two photons (for a detailed derivation, refer to Appendix 3.A). This approach, sim-

ilar to the protocol presented by Lindner and Rudolph, enables the construction of 1D cluster states.

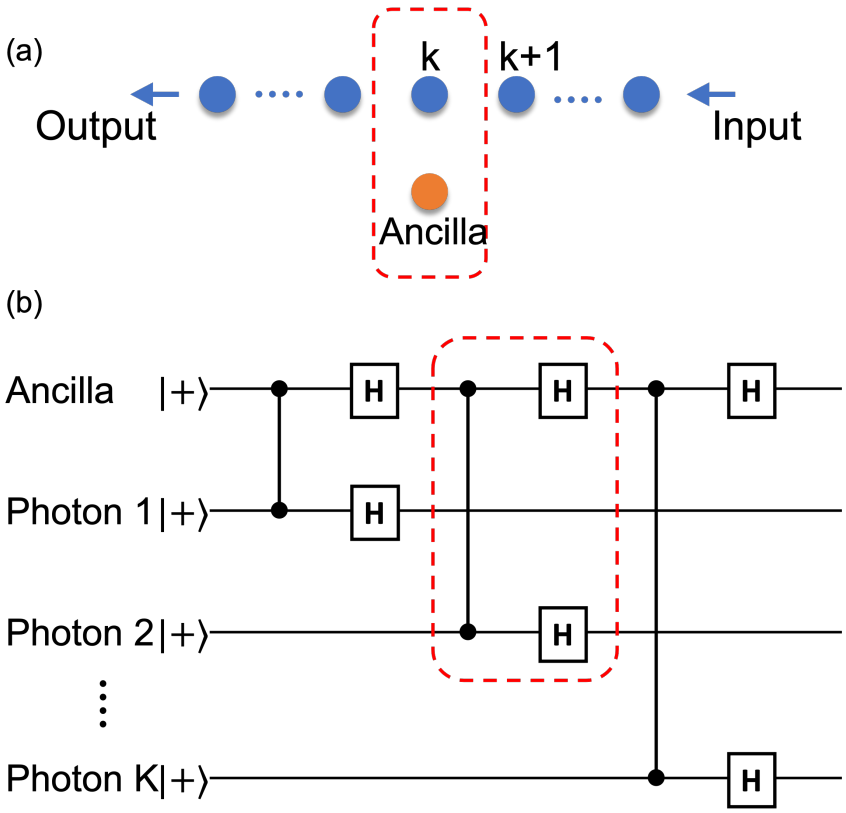

Figure 3.4: (a) Schematic diagram of a system that incorporates a stationary ancilla interacting sequentially with a series of photons. (b) Quantum circuit designed to generate nearest neighbor entanglement among photons. The dotted lines symbolize CZ gates, while the squares labeled H denote Hadamard gates.

3.2.3 Non-Nearest-Neighbor Entanglement and Time-Delay Feedback

To generate non-nearest-neighbor entanglement between photons through an ancilla, a time-delay feedback mechanism comes into play [43, 113]. As illustrated in Figures 3.5, this mechanism allows the interaction between two photons k and $k-N$. A mirror reflects photon $k-N$ to the atom following a delay of NT_{cycle}. The atom then applies a CZ gate sequentially to photon $k-N$ and photon k. After this, the application of Hadamard gates to photon k and the

atom essentially swaps their states. This action creates the non-nearest-neighbor entanglement between photons k and $k-N$ while setting the system up for the next clock cycle (see Appendix 3.A for a detailed derivation). Implementing this process for all the photons in the chain allows the generation of a 2D cluster state.

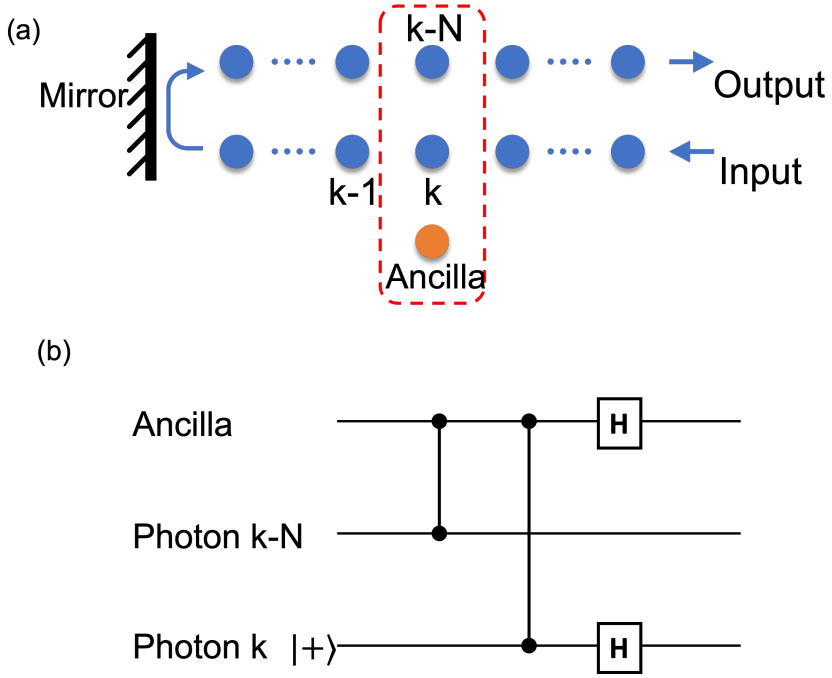

Figure 3.5: (a) Schematic diagram for generating non-nearest neighbor entanglement, incorporating a stationary ancilla, a series of photons, and a single time-delay photon feedback. Photons $k-N$ and k interact sequentially with the ancilla during one cycle. (b) Quantum circuit designed to entangle photons $k-N$ and k.

3.2.4 3D Cluster State Generation Procedure

Now that we have devised a method to generate both nearest- and non-nearest-neighbor interactions, these can be amalgamated to create multi-dimensional cluster states. Figure 3.6(a) showcases this approach for a 3D cluster state, necessitating two non-nearest neighbor interactions, and consequently, two time-delay feedbacks. The first mirror imparts a delay of NT_{cycle}

to a photon while the second induces a delay of $(MN - N)\, T_{\text{cycle}}$. This staggered delay pattern facilitates the ancilla in sequentially applying a CZ gate to photons $k - MN$, $k - N$, and k. While the protocol remains indifferent to the order of CZ gate application, we adopt this specific sequence for the sake of clarity. Following the CZ gates, we apply Hadamard gates on photon k and the ancilla, thereby executing the quantum circuit as shown in Figure 3.6(b). Repeating this circuit for each cycle across all photons leads to the creation of a 3D cluster state.

The procedure outlined above yields a cluster state that slightly deviates from the one built on a cuboid lattice, as depicted in Figure 3.3(a). While the internal structure of the cluster state remains unaltered, the edge introduces a more intricate boundary condition, as illustrated in Figure 3.6(c). Photon (N, M, l), located on the lattice boundary, also gets entangled with photon $(1, 1, l + 1)$, due to their adjacency in the rearranged linear chain. As such, the generated cluster state exhibits a helical connectivity pattern, akin to the 2D cluster state proposed by Pichler et al. [43], but now extended to a higher dimension. The redundant qubits at the boundary and undesired locations can be eliminated by conducting measurements in the computational basis post-generation, leading to the desired cluster state typically employed in topological fault-tolerant MBQC.

3.3 Physical Implementation

The preceding section outlines the theoretical protocol for generating 3D cluster states. This section will elaborate on how to physically implement this concept using the atom-photon interface and time-delay feedback. The atom-photon interface allows the application of controlled phase-flip (CZ) gates between atomic and photonic qubits. For a detailed description,

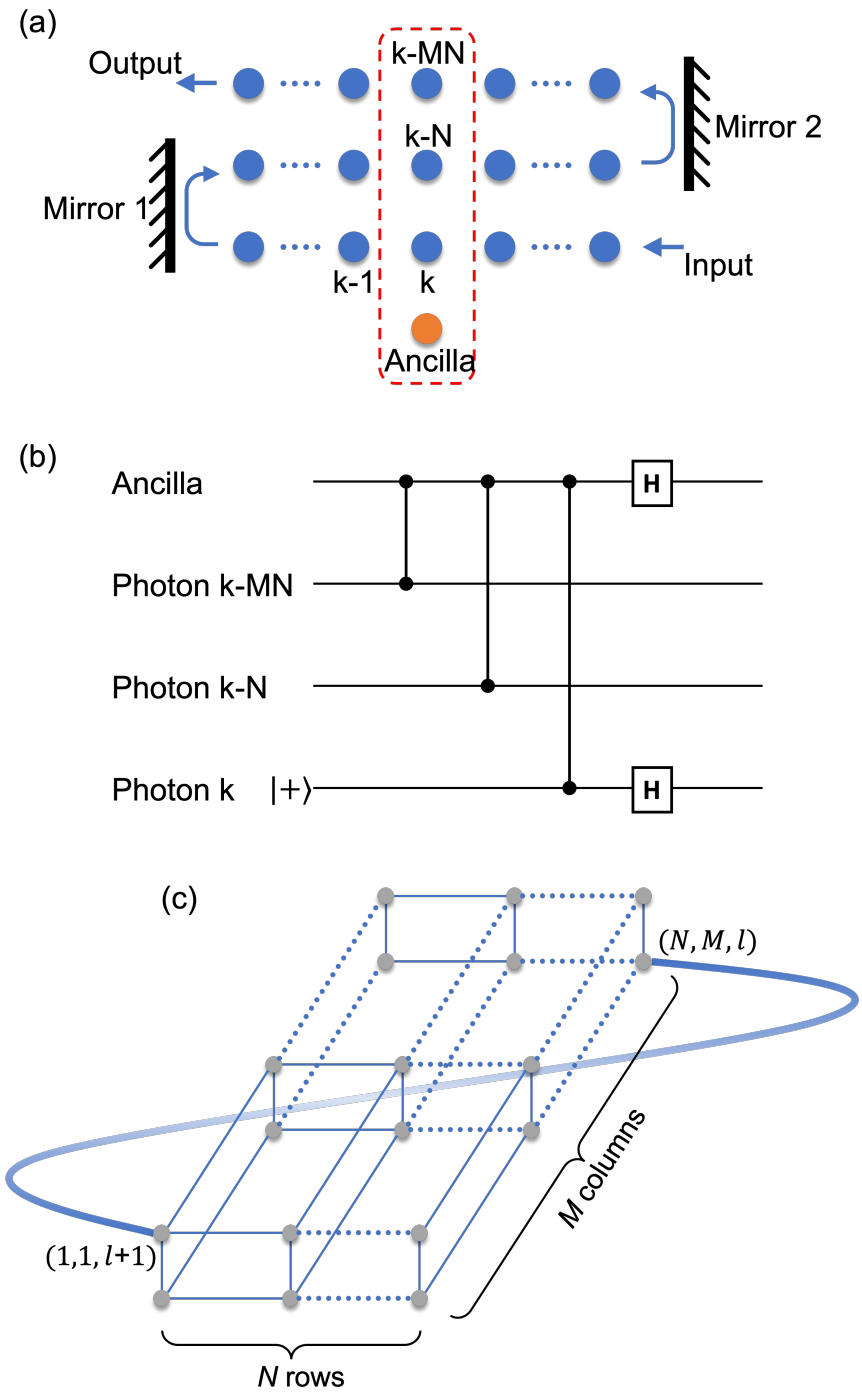

Figure 3.6: (a) Schematic diagram for generating 3D cluster states, involving a stationary ancilla, a sequence of photons, and two instances of time-delay feedback. Photons $k-MN$, $k-N$, and k interact sequentially with the ancilla within one cycle. (b) Quantum circuit designed to entangle photons $k-MN$, $k-N$, and k. (c) Helical boundary in a 3D cluster state, where, for instance, photons (N, M, l) and $(1, 1, l+1)$ are entangled.

please refer to Section 2.2.2.

Figure 3.7(a) illustrates the physical implementation of the time-delay feedback necessary for the formation of a 3D cluster state. Two time-delay feedback loops comprising two delay lines (Delay Line 1 and 2) and two rapid optical switches (Switch 1 and 2) are utilized. These switches can quickly transition between reflection and transmission modes for photons. A quarter-wave plate ($\frac{\lambda}{4}$-waveplate) is integrated into Delay Line 2 to adjust the photon's polarization. Additionally, a switch is installed at the system's input/output port to guide the input photons towards the cavity and connect the photons departing the cavity to the output port. The interval between sequentially injected photons is represented as T_{cycle}. To generate a 3D cluster state with dimensions $N \times M \times L$, the delay of Line 1 is set as $\left(MN - N - \frac{1}{3}\right) T_{\text{cycle}}$ and that of Line 2 as $\left(N - \frac{1}{3}\right) T_{\text{cycle}}$. The time delay between Switch 1 and the cavity is represented as τ_1, and the delay between Switch 1 and Switch 2 is depicted as τ_2, where $\tau_1, \tau_2 \ll T_{\text{cycle}}$.

Figure 3.7(b) indicates how the reflection and transmission states of Switch 1 and Switch 2 are set as functions of time, relative to the commencement of the k^{th} cycle (where $t = 0$). The clock cycle T_{cycle} is divided into three segments that correspond to the propagation periods of photons $k - MN$, $k - N$, and k, respectively. The arrows indicate the timings when a photon reaches each switch, either moving towards or rebounding from the cavity. The timing sequence is designed so that photon $k - MN$ first interacts with the cavity and exits the system. This is then followed by photon $k - N$, which reflects off the cavity and proceeds into Delay Line 1, and subsequently, photon k reflects off the cavity, entering Delay Line 2. These steps emulate the CZ gates between the photons and the atom as illustrated in the quantum circuit in Figure 3.6(b). In Delay Line 2, photon k traverses the $\frac{\lambda}{4}$-waveplate, reflects off a mirror, passes through the waveplate again, achieving an effective $\frac{\pi}{2}$ rotation, thereby implementing a Hadamard gate on

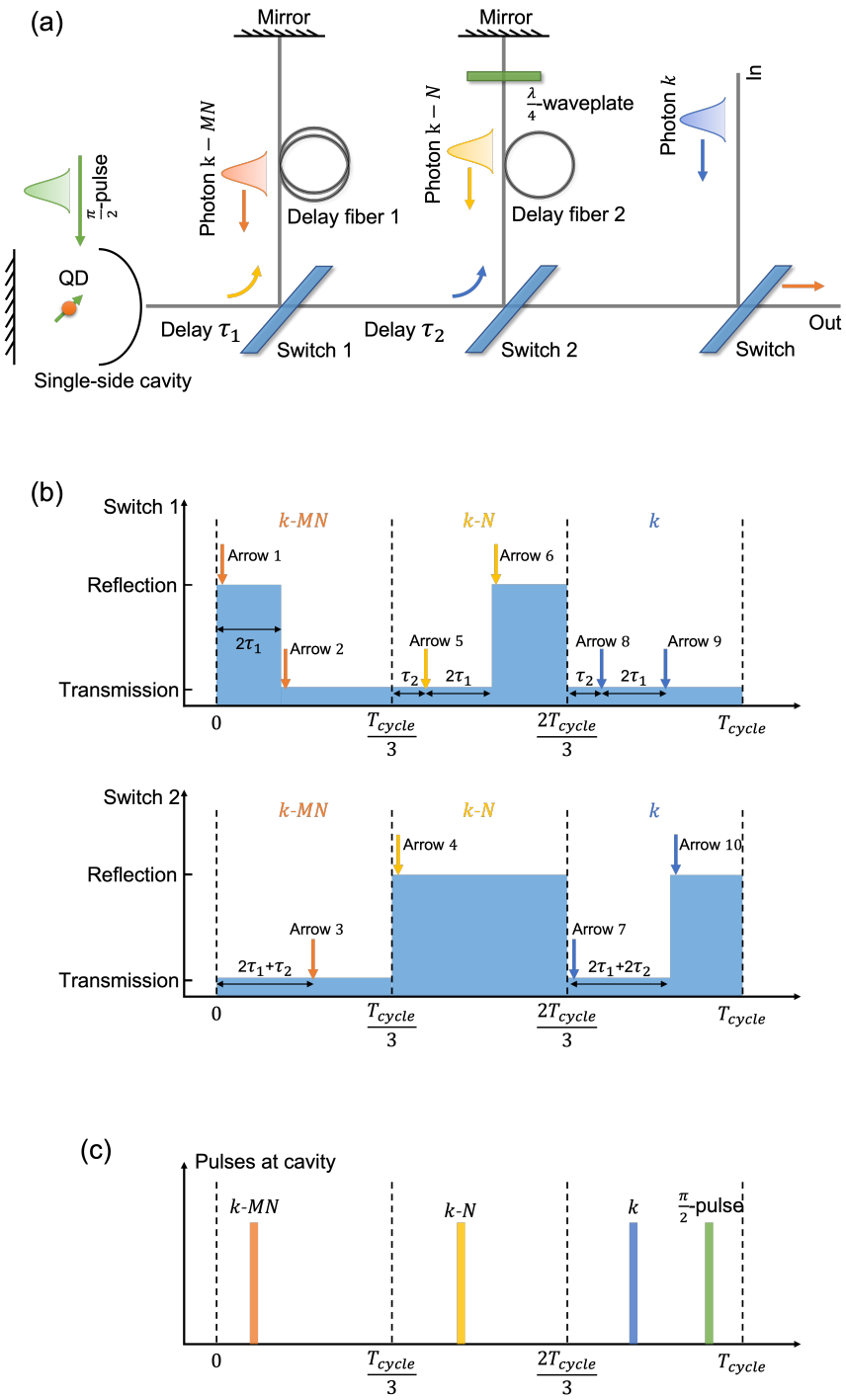

Figure 3.7: (a) Setup for generating a 3D cluster state. During the k^{th} cycle, photons $k-MN$, $k-N$, and k sequentially reflect off the cavity. (b) Schematic diagrams illustrating the state-flipping of two switchable mirrors between reflective and transmissive states during a photon injection period (T_{cycle}). The arrows denote the time points when photons reach the switches. (c) Diagram displaying the sequence of pulses reaching the cavity during one cycle.

the photon's polarization. A Hadamard gate is then applied to the atom using an ultrafast optical Raman control pulse of $\frac{\pi}{2}$ rotation, as indicated in the timing diagram in Figure 3.7(c). This $\frac{\pi}{2}$-pulse arrives at the cavity following the sequential reflections of photons $k - MN$, $k - N$, and k in the cycle.

For the initial few photons 1 through MN, either Delay Line 1 or Delay Line 2 may not house any photons. However, the procedure remains functional without any modification in this initial phase. For photons 1 through N, both delay lines remain vacant, so these photons will reflect off the cavity sequentially, constructing an initial 1D cluster state. Photons $N + 1$ through MN will then form entanglement with the returning photons from Delay Line 2, but no photon will depart from Delay Line 1. Consequently, these photons will construct the initial 2D cluster state that forms the first layer of the 3D cluster state. The remaining photons will then build additional layers needed to establish the 3D lattice. Note that the number of injected photons increases by one when needed so that the last layer can be partially filled.

3.4 Extension to Higher Dimensional States

The extension to higher dimensions can be performed analogously. Each additional dimension requires another non-nearest-neighbor connection, thereby necessitating an extra time-delay feedback. As depicted in Figure 3.8(a), to generate s-dimensional cluster states, we employ $(s - 1)$ mirrors to execute $(s - 1)$ time-delay feedbacks. Thus, the protocol showcases efficiency in that the increase in dimensions only results in a linear increment in the number of time-delay feedbacks.

The setup illustrated in Figure 3.8(b) comprises $(s - 1)$ time-delay feedback loops. We

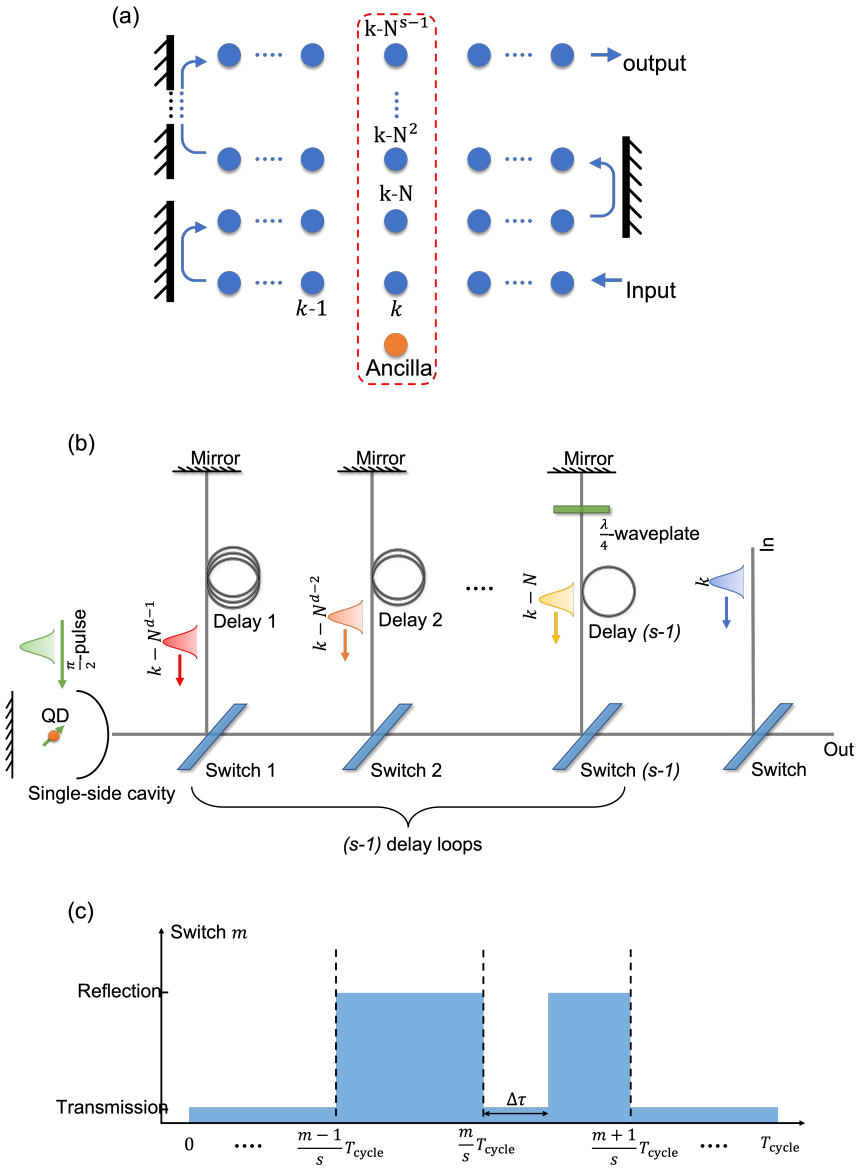

Figure 3.8: (a) Schematic diagram for generating s-dimensional cluster states using $(s-1)$ time-delay feedbacks. (b) Setup for generating an s-dimensional cluster state. (c) Schematic diagram demonstrating the state of switch m.

determine the delay time of line m as $\left(\prod_{l=1}^{m} N_l - \prod_{l=1}^{m-1} N_l - \frac{1}{s}\right) T_{\text{cycle}}$, where N_l signifies the length of the l^{th} dimension of the cluster state. Figure 3.8(c) presents the timing diagram for Switch m throughout a complete cycle with a duration of T_{cycle}. This timing diagram expands upon Figure 3.7(b), accommodating additional feedback loops.

3.5 Analysis of Cluster State Fidelity

3.5.1 Tensor Network Formalism

To estimate the fidelity of the produced cluster states, we employ a tensor network formalism [63]. A tensor network formalism efficiently characterizes a cluster state via interconnected tensors, the count of which equals the number of photons. Furthermore, the tensor network facilitates the calculation of fidelity of the cluster state realized practically in contrast to its theoretical prediction. This is achieved by constructing diagrams that render the calculation process more visually intuitive and straightforward than conventional linear algebra methods. This section initially provides a diagrammatic derivation of the tensor network representation of the multi-dimensional cluster state. Our derivation extends beyond analyzing the cluster state, offering value in a wider context of simulating matrix product states (MPS) [61] and projected entangled pair states (PEPS) [64] brought about by sequential photons [114–116].

Figure 3.9 presents the tensor network representation for a 1D cluster state, our initial focus before progressing to higher dimensions. In the context of 1D cluster states, photon k is linked to two photons, namely $k-1$ and $k+1$. Figure 3.9(a) demonstrates the tensor network diagram where both the states of the photons and the two-qubit gates possess tensor representations. The blue circles act as rank-1 tensors, symbolizing initially unentangled photons in the state $|+\rangle$. The

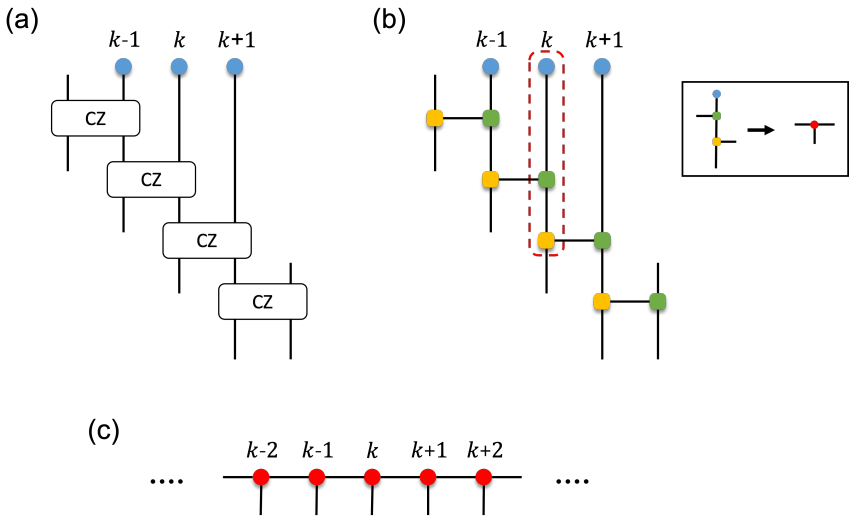

Figure 3.9: (a) Tensor network diagram of producing a 1D cluster state. (b) Decomposition of the CZ tensors in (a) into two rank-3 tensors, depicted by the yellow and green squares. These are subsequently combined with the circle tensor to form a new rank-3 tensor. (c) Application of the tensor contraction process illustrated in (b) to all photons enables the derivation of the simplified tensor network representing a 1D cluster state.

boxes labelled as CZ are rank-4 tensors denoting CZ gates. The lines emanating from the blue circles and boxes signify the indices of the tensors. Each rectangular box has four lines, two projecting upwards and two downwards. The lines ascending represent the input qubits, while the descending lines indicate the output qubits. The lines that connect the circles and boxes depict the application of CZ gates between two photons. The uncontracted lines directed downwards signify the qubits for the photons within the generated cluster state.

In standard tensor network state representations, such as Matrix Product States (MPS) and Projected Entangled Pair States (PEPS), each tensor stands for a single qubit. These qubits may have several contracted indices, but only one remains uncontracted. Nonetheless, the diagram in Figure 3.9(a) has more tensors than the system's qubits, necessitating simplification. Initially, we decompose the CZ tensor into two rank-3 tensors using singular value decomposition (refer to Appendix 3.B). Figure 3.9(b) demonstrates the diagram following this decomposition. The

yellow and green squares symbolize the two tensors derived from the CZ tensors, containing two vertical lines and one horizontal line. In contrast to the CZ tensors, the yellow and green tensors act on one photon. Consequently, we can contract tensors for a photon along its vertical line (see the dashed box in Figure 3.9(b)). This allows us to generate a new rank-3 tensor (refer to the solid box in Figure 3.9(b)). This rank-3 tensor maintains one uncontracted index symbolizing the qubit basis and two contracted indices denoting entanglement with adjacent tensors. Undertaking this tensor contraction process for all photons results in the canonical tensor network diagram of the 1D cluster state, as depicted in Figure 3.9(c).

Figure 3.10 illustrates the expansion of the tensor network representation to a 3D cluster state, where each photon is connected to six others. The creation of these connections in our protocol using two time-delay feedbacks is depicted in Figure 3.10(a). To streamline the tensor network, we decompose the CZ tensors into two rank-3 tensors each (represented by the green and yellow squares), leading to the revised diagram shown in Figure 3.10(b). By contracting the tensors along the vertical line for each photon, we generate a rank-7 tensor. This tensor comprises a single uncontracted index representing the qubit's basis, and six contracted indices indicating entanglement with neighboring tensors. Implementing this tensor contraction procedure for all photons results in the tensor network diagram of the 3D cluster state, depicted in Figure 3.10(c).

This derivation can be straightforwardly extended to higher s-dimensional cluster states. For each added dimension, we incorporate two additional square tensors into the contraction sequence. The end result is a rank $2s + 1$ tensor, characterized by a single uncontracted index representing the qubit basis, and $2s$ contracted indices indicating entanglement with neighboring tensors. Consequently, the tensor network representation for the s-dimensional cluster state comprises these contracted tensors, assembled in a s-dimensional superlattice.

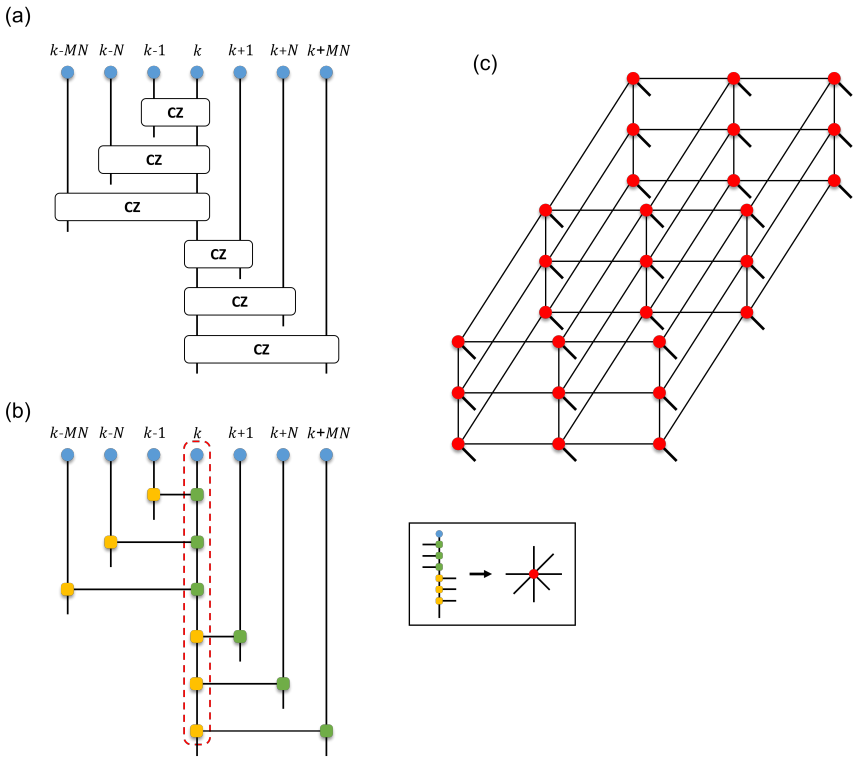

Figure 3.10: (a) Tensor network diagram that builds entanglement of photon k with its neighboring photons in a 3D cluster state. (b) Decomposition of the CZ tensors in (a) into two rank-3 tensors, symbolized by yellow and green squares. These can be combined with the circle tensor to form a rank-7 tensor. (c) Tensor contraction process as demonstrated in (b), when applied to all photons, facilitates the derivation of a simplified tensor network representing a 3D cluster state.

The preceding derivation presupposes ideal CZ gates, a premise that falls short in a realistic system. In actual physical implementation, the spin-photon gate is executed through a reflection operation U_{r}, as depicted in Equation 2.6. Owing to finite cooperativity and detuning, this reflection operation results in an imperfect CZ gate. Nevertheless, we can integrate U_{r} within the tensor network formalism. Appendix 3.C demonstrates how to transpose the imperfections of U_{r} onto the photon-photon CPHASE gate. This imperfect CPHASE gate can still be represented by a rank-4 tensor, which can be translated to a canonical representation following the decomposition methodology depicted in Figure 3.10.

3.5.2 Fidelity Evaluation

Having integrated imperfect CZ gates into the tensor network formalism, we can compute the fidelity, denoted as $\mathcal{F}_0$, which acts as a measure of our protocol's performance. We define this fidelity as:

$$\mathcal{F}_0 = \frac{|\langle \Psi_C | \Phi_C \rangle|^2}{\langle \Phi_C | \Phi_C \rangle}, \tag{3.2}$$

where $|\Psi_C\rangle$ represents the ideal cluster state and $|\Phi_C\rangle$ signifies the unnormalized output state produced by imperfect CZ gates. Leveraging the decomposition process delineated in the previous paragraph, we can represent these two states using tensor networks and compute the inner product of the two states by numerically contracting the networks. For executing this calculation, we employed the ITensor library software [117].

The prior definition of fidelity does not take into account spin decoherence, which occurs due to the spin's interaction with nearby spins [118]. We can portray this decoherence process as a quantum phase-flip channel that randomly flips the spin's phase with a probability of $\frac{T_{\mathrm{cycle}}}{T_2}$ in

a single cycle, where T_2 represents the characteristic spin dephasing time. This phase-flip error corresponds to flipping the phase of the subsequent injected photon, transforming the cluster state into another state within an orthogonal subspace [38]. Consequently, the spin decoherence reduces the fidelity of the cluster state by a factor of $\left(1 - \frac{T_{\text{cycle}}}{T_2}\right)$ in each cycle.

In addition to decoherence, the fidelity must accommodate the error resulting from imperfect spin rotation. This can be modeled as a quantum depolarization channel on the subsequent injected photon, occurring at a rate p and reducing the fidelity by $\left(1 - \frac{p}{2}\right)$. Combining the effects of spin dephasing and imperfect spin rotation, the total spin errors lower the fidelity by a factor of $\alpha = \left(1 - \frac{p}{2}\right)\left(1 - \frac{T_{\text{cycle}}}{T_2}\right)$ within a single photon injection period. As a result, we derive a revised fidelity $(\mathcal{F}_1)$ as follows:

$$\mathcal{F}_1 = \alpha^N \cdot \mathcal{F}_0, \tag{3.3}$$

where N represents the number of photons within the cluster state.

Photon loss is another factor that hampers the generation rate of cluster states. Fortunately, this error can be straightforwardly detected by comparing the number of photons entering and exiting the system. To quantify photon loss, we define the probability of collecting all the photons after a single protocol execution as the success probability $(\mathcal{P})$. This can be computed as:

$$\mathcal{P} = \eta^N \cdot \langle \Phi_C | \Phi_C \rangle \,, \tag{3.4}$$

where η denotes the detection efficiency, which accounts for state-independent loss, while $|\Phi_C\rangle$ is the unnormalized output state accounting for the loss due to finite cooperativity.

3.5.3 Parameter Settings

In order to analyze the protocol's performance under real-world experimental conditions, we base our consideration on the physical implementation of a spin qubit [73]. This utilizes an electron-charged quantum dot in a nano-cavity, a system that implements the atom-photon CZ gate modelled by U_{r} in Equation 2.6. The two spin-dependent reflection coefficients are computed as

$$r_{\uparrow,\downarrow} = \frac{C_{\uparrow,\downarrow} - 1}{C_{\uparrow,\downarrow} + 1}, \tag{3.5}$$

where $C_{\uparrow} = \frac{4g^2}{\gamma\kappa}$ signifies the on-resonant atom-cavity cooperativity, and $C_{\downarrow} = \frac{4g^2}{\gamma(\kappa + i2\Delta_{\downarrow})}$ represents the off-resonant cooperativity. Here, g is the quantum dot-cavity coupling strength, κ is the atomic dipole decay rate, γ is the cavity mode decay rate, and $\Delta_{\downarrow}$ is the detuning frequency between the spin-down state transition and the cavity mode. The detuning frequency is determined by an applied magnetic field (B) as

$$\Delta_{\downarrow} = \frac{(g_e + g_h)\,\mu_{\mathrm{B}} B}{\hbar}, \tag{3.6}$$

where g_e and g_h are the Lande factors for the electron and hole, respectively, and μ_{B} is the Bohr magneton. Building on previous experimental measurements, we have selected the following system parameters: $g_e = 0.43$, $g_h = 0.21$, $g = 10$ GHz, $\kappa = 0.3$ GHz, $\gamma = 40$ GHz [72, 119]. We have additionally chosen a spin rotation fidelity of 98% and a characteristic spin dephasing time of $T_2 = 2\,\mu\mathrm{s}$ [120]. We also presuppose a detection efficiency of $\eta = 0.8$ [121] and designate the photon injection period as a time cycle of $T_{\mathrm{cycle}} = 5\,\mathrm{ns}$. A typical pulse duration for the probe beam [119] and control laser [86] can be as short as hundreds of picoseconds, rendering it

negligible in comparison to the time cycle. These selected parameters enable us to estimate the fidelity of the state generated under realistic experimental conditions.

3.5.4 Simulation Results

We can perform simulations of the 3D cluster state with dimensions of $N \times M \times L$, where L can be extended indefinitely. This is feasible because the contraction of two 3D tensor network states of dimensions $N \times M \times L$ only requires the storage of an $N \times M$ tensor network in memory [63]. The stack dimension predominantly affects the fidelity of the initial photons and does not influence the scaling behavior of fidelity. Our results show that fidelity decreases exponentially with the increasing number of photons, which can be modeled as:

$$\mathcal{F}_1 \sim \beta^K, \tag{3.7}$$

where β is the scaling factor of the fidelity, and K represents the total number of photons in the cluster state.

We also investigated fidelity in relation to different values of resonant cooperativity C and magnetic field B, as these two parameters uniquely determine the off-resonant cooperativity $C_\downarrow$. Figure 3.11 displays the scaling factor (β) of fidelity as a function of cooperativity C and magnetic field B. We observed that fidelity increases with magnetic field strength and that there is an optimal cooperativity for each magnetic field value that maximizes the fidelity of the output state. This phenomenon is due to the fact that at a constant magnetic field, if the resonant cooperativity C is too low, the photon interaction with the atom is inadequate. Conversely, if C is excessively high, the off-resonant cooperativity $C_\downarrow$ also escalates, based on the relation $C_\downarrow = \frac{C}{1+i2\Delta_z/\kappa}$. This

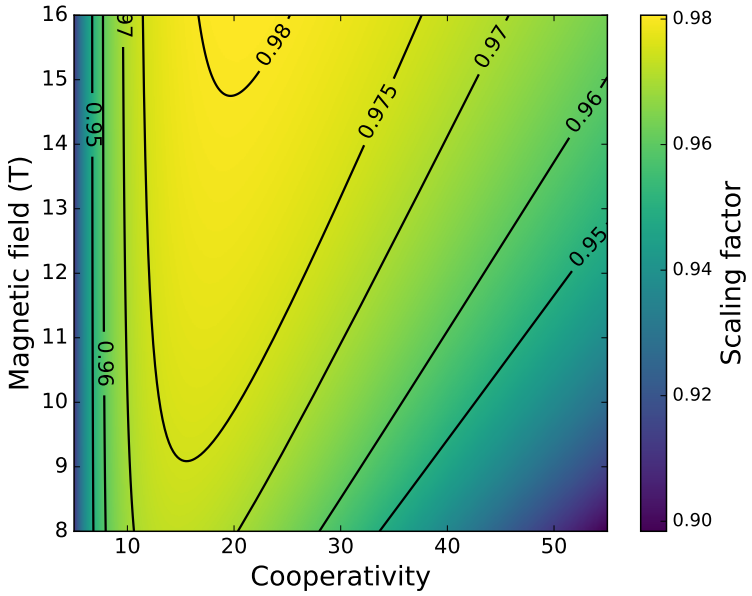

Figure 3.11: Scaling factor (β) of fidelity, as a function of both resonant cooperativity and magnetic field for a 3D cluster state.

increase surpasses the high-quality CZ gate requirement ($C_{\downarrow} \ll 1$), which in turn degrades the fidelity. Notably, achieving maximal fidelity cluster states would demand an exceptionally high magnetic field. However, implementing such a high magnetic field is impractical since an increase in the magnetic field reduces the relaxation time of the spin in the quantum dot [122]. In a subsequent section 4.2, we will revisit the atom-photon interface and address this tradeoff and the dilemma posed by the impracticality of high magnetic fields.

In addition, we can also calculate the generation rate of the cluster state. For example, given a detection efficiency of $\eta = 0.8$, the probability of successfully generating an 8-photon cluster state stands at 0.103. Given the photon injection period of $T_{\text{cycle}} = 5\,\text{ns}$, the system can produce one state every $40\,\text{ns}$. This results in a cluster state generation rate of approximately 2.6×10^6 per second.

Appendix 3.A Derivation of Quantum Circuits for Cluster State Generation

We first demonstrate that the quantum circuit depicted in Figure 3.4(b) builds the nearest-neighbor entanglement between photons within a linear chain. Our starting point is a 1D cluster state represented by $K+1$ qubits

$$|\Psi_{1\mathrm{D}}\rangle = \prod_{k=1}^{K} Z_{k-1,k}|+\rangle_{\mathrm{A}} \otimes |+\rangle^{\otimes K}, \tag{3.8}$$

where $Z_{i,j}$ denotes the controlled phase-flip (CZ) gate on qubit i and j. Here, the 0^{th} qubit represents the atom (A), while the remaining numbered qubits correspond to photons. We introduce a swap operator $S_{i,j}$ to exchange states between qubit i and j. Consequently, Equation 3.8 can be rewritten as

$$|\Psi_{1\mathrm{D}}\rangle = \prod_{k=1}^{K} S_{\mathrm{A},k} Z_{\mathrm{A},k}|+\rangle_{\mathrm{A}} \otimes |+\rangle^{\otimes K}. \tag{3.9}$$

In this product, the order is from right to left, which means $\prod_{i=1}^{K} U_i = U_K \cdots U_1$. We can apply the following identity

$$S_{\mathrm{A},k} Z_{\mathrm{A},k}|\phi\rangle_{\mathrm{A}} \otimes |+\rangle_k = (H_{\mathrm{A}} \otimes H_k)\, Z_{\mathrm{A},k}|\phi\rangle_{\mathrm{A}} \otimes |+\rangle_k, \tag{3.10}$$

where $|\phi\rangle_{\mathrm{A}}$ represents an arbitrary state of the atom, and H_{A} and H_k are the Hadamard gates on the atom and photon, respectively. This identity is applicable when the photon is in the state $|+\rangle$, whereas the atom can be in any state, whether entangled or unentangled. Using Equation 3.10,

we reformulate Equation 3.9 as

$$|\Psi_{1\mathrm{D}}\rangle = \prod_{k=1}^{K} \left(H_{\mathrm{A}} \otimes H_k\right) Z_{\mathrm{A},k} |+\rangle_{\mathrm{A}} \otimes |+\rangle^{\otimes K}. \tag{3.11}$$

This equation is implemented by the quantum circuit displayed in Figure 3.4(b).

We now establish that Figure 3.5 engenders non-nearest-neighbor entanglement between photons $k-N$ and k. Building on the 1D cluster state, we introduce an additional dimension by entangling photons $k-N$ and k to get

$$|\Psi_{2\mathrm{D}}\rangle = \prod_{k=N+1}^{K} Z_{k-N,k} \prod_{k=1}^{K} Z_{k-1,k} |+\rangle_{\mathrm{A}} \otimes |+\rangle^{\otimes K}. \tag{3.12}$$

Given that CZ gates $Z_{i,j}$ commute with each other, we can reorder the operators in Equation 3.12 to get

$$|\Psi_{2\mathrm{D}}\rangle = \prod_{k=N+1}^{K} Z_{k-1,k} Z_{k-N,k} \prod_{k=1}^{N} Z_{k-1,k} |+\rangle_{\mathrm{A}} \otimes |+\rangle^{\otimes K}. \tag{3.13}$$

As in the 1D case, we can introduce the swap operator $S_{i,j}$ to rewrite Equation 3.13 as

$$|\Psi_{2\mathrm{D}}\rangle = \prod_{k=N+1}^{K} S_{\mathrm{A},k} Z_{A,k} Z_{\mathrm{A},k-N} \prod_{k=1}^{N} S_{\mathrm{A},k} Z_{\mathrm{A},k} |+\rangle_{\mathrm{A}} \otimes |+\rangle^{\otimes K}. \tag{3.14}$$

Applying the identity from Equation 3.10, we can reformulate Equation. 3.14 as

$$|\Psi_{2\mathrm{D}}\rangle = \prod_{k=N+1}^{K} \left(H_{\mathrm{A}} \otimes H_k\right) Z_{\mathrm{A},k} Z_{\mathrm{A},k-N} \prod_{k=1}^{N} \left(H_{\mathrm{A}} \otimes H_k\right) Z_{\mathrm{A},k} |+\rangle_{\mathrm{A}} \otimes |+\rangle^{\otimes K}. \tag{3.15}$$

Consequently, we first create a 1D cluster state. On this basis, the quantum circuit in Figure 3.5(b)

implements the iterative steps of $\prod_{k=N+1}^{K}(H_{\mathrm{A}}\otimes H_k)\,Z_{\mathrm{A},k}Z_{\mathrm{A},k-N}$. This operation entangles photon k with photons $k-N$ and $k-1$, thereby generating the 2D cluster state.

Finally, we establish that Figure 3.6(b) generates the unit cell of the 3D cluster state. By introducing two non-nearest-neighbor gates to the linear chain of photons, we can derive the 3D cluster state as

$$|\Psi_{3\mathrm{D}}\rangle \prod_{k=MN+1}^{K} Z_{k-MN,k} \prod_{k=N+1}^{K} Z_{k-N,k} \prod_{k=1}^{K} Z_{k-1,k}|+\rangle_{\mathrm{A}}\otimes|+\rangle^{\otimes K}. \tag{3.16}$$

Since $Z_{i,j}$ commute with each other, we can rearrange the operators in the above equation as

$$\begin{aligned}|\Psi_{3\mathrm{D}}\rangle = &\prod_{k=MN+1}^{K} Z_{k-1,k}Z_{k-N,k}Z_{k-MN,k} \\ &\times \prod_{k=N+1}^{MN} Z_{k-1,k}Z_{k-N,k} \prod_{k=1}^{N} Z_{k-1,k}|+\rangle_{\mathrm{A}}\otimes|+\rangle^{\otimes K}.\end{aligned} \tag{3.17}$$

Upon introducing the swap operator $S_{i,j}$ between the qubit i and j, we can reformulate Equation 3.17 as

$$\begin{aligned}|\Psi_{3\mathrm{D}}\rangle = &\prod_{k=MN+1}^{K} S_{\mathrm{A},k}Z_{\mathrm{A},k}Z_{\mathrm{A},k-N}Z_{\mathrm{A},k-MN} \\ &\times \prod_{k=N+1}^{MN} S_{\mathrm{A},k}Z_{\mathrm{A},k}Z_{\mathrm{A},k-N} \prod_{k=1}^{N} S_{\mathrm{A},k}Z_{\mathrm{A},k}|+\rangle_{\mathrm{A}}\otimes|+\rangle^{\otimes K}.\end{aligned} \tag{3.18}$$

The operators within the second line of the preceding equation generate the 2D cluster state of dimensions $M\times N$. Utilizing the identity from Equation 3.10, we can reshape the operators within the first parentheses as

$$|\Psi_{3\mathrm{D}}\rangle = \prod_{k=N+1}^{K}(H_{\mathrm{A}}\otimes H_k)\,Z_{\mathrm{A},k}Z_{\mathrm{A},k-N}Z_{\mathrm{A},k-MN}|\Psi_{2\mathrm{D}_{\mathrm{M}\times\mathrm{N}}}\rangle. \tag{3.19}$$

The quantum circuit illustrated in Figure 3.6(b) implements the iterative operators from Equation 3.19, thereby facilitating the creation of the 3D cluster state based on an existing 2D cluster state.

Appendix 3.B Matrix Product Operator Decomposition

In this appendix, we elucidate the process of decomposing the CZ gate. Initially, we write the matrix element of the CZ gate between qubits i and j as

$$Z_{i,j} = Z^{\alpha,\beta}_{\alpha',\beta'} \left|\alpha',\beta'\right\rangle\!\left\langle\alpha,\beta\right|_{i,j}. \tag{3.20}$$

Subsequently, we perform a partial transposition of the matrix:

$$Z_{i,j} = Z^{\beta',\beta}_{\alpha',\alpha} \left|\alpha'\right\rangle\!\left\langle\alpha\right|_i \otimes \left|\beta'\right\rangle\!\left\langle\beta\right|_j. \tag{3.21}$$

We can then implement a Singular Value Decomposition on the matrix $Z^{\beta',\beta}_{\alpha',\alpha}$ on its row indices $(\alpha'\alpha)$ and column indices $(\beta'\beta)$, leading to

$$Z^{\beta',\beta}_{\alpha',\alpha} = \sum_s U^s_{\alpha'\alpha} \Lambda_s {V^s_{\beta'\beta}}^*, \tag{3.22}$$

where U and V are unitary, and Λ is a positive operator.

Subsequently, we take the square root of Λ and incorporate it into U and V, yielding

$$\begin{aligned} A^s_{\alpha'\alpha} &= U^s_{\alpha'\alpha}\sqrt{\Lambda}_s, \\ B^s_{\beta'\beta} &= {V^s_{\beta'\beta}}^*\sqrt{\Lambda}_s, \end{aligned} \tag{3.23}$$

In this context, we use Einstein's notation to forgo the use of summation operators. Hence, we can express the CZ tensor Z as the product of two tensors A and B as follows:

$$Z^{\beta',\beta}_{\alpha',\alpha} = A^s_{\alpha'\alpha}B^s_{\beta'\beta}. \tag{3.24}$$

In Figure 3.9(b), tensor A is depicted as a yellow square and tensor B as a green square. The indices α, α' and β, β' represent the qubit basis, and s stands for the index representing the entanglement bond between qubits.

Appendix 3.C Derivation of the Imperfect Photon-Photon CZ Gate

In this appendix, we demonstrate how an imperfect reflection operation U_{r}, as indicated in Eq. 2.6, leads to an effective, albeit imperfect, photon-photon CZ gate. The quantum circuit in Figure 3.6(b) entangles photon k with its neighbors in the three-dimensional cluster states. We can express this circuit as an operator form:

$$\mathcal{E} = H_s \otimes H_k Z_{s,k} Z_{s,k-N} Z_{s,k-MN}. \tag{3.25}$$

In an actual physical implementation, we substitute the ideal CZ gates Z with the reflection operator

$$U_{s,k} = (I + \epsilon R_{s,k})\, Z_{s,k}, \tag{3.26}$$

where $\epsilon R = UZ - I$. Here, $\epsilon \sim O\left(\left|1 - \frac{C_\uparrow - 1}{C_\uparrow + 1}\right| + \left|1 + \frac{C_\downarrow - 1}{C_\downarrow + 1}\right|\right)$ signifies the order of errors. Consequently, Equation 3.25 transforms to:

$$\mathcal{E}_1 = (H_s \otimes H_k)\,(I + \epsilon R_{s,k})\, Z_{s,k} U_{s,k-N} U_{s,k-MN}\ . \tag{3.27}$$

By commuting $H_s \otimes H_k$ and $I + \epsilon R_{s,k}$ and utilizing the relation in Eq. 3.10, we can simplify Equation 3.27 to:

$$\mathcal{E}_1 = \widetilde{U}_{s,k} U_{k,k-N} U_{k,k-MN} S_{s,k}, \tag{3.28}$$

where $S_{s,k}$ denotes the swap gate between the ancilla and photon k, and

$$\widetilde{U}_{s,k} = [I + \epsilon\,(H_s \otimes H_k)\, R_{s,k}\, (H_s \otimes H_k)]\, Z_{s,k} \tag{3.29}$$

represents an imperfect CZ gate with the error in $O(\epsilon)$.

Ultimately, we obtain an effective operation for entangling photon k with its six neighbors, which is:

$$\mathcal{E} = U_{k+MN,k} U_{k+N,k} U_{k+1,k} U_{k,k-N} U_{k,k-MN} U_{k,k-1}, \tag{3.30}$$

where $\widetilde{U}$ signifies the gate between the nearest neighbors, and U denotes the gate between the non-nearest neighbors.

Chapter 4: Optical Quantum Fourier Transform

4.1 Basics of Quantum Fourier Transform

The quantum Fourier transform (QFT) is a powerful tool in quantum information processing due to its significant role in various quantum algorithms. Most notably, these include Shor's factoring algorithm [4], which is utilized for integer factorization, and the quantum phase estimation algorithm [123], employed for eigenvalue estimation in quantum systems. QFT also finds applications in quantum simulation, quantum metrology, and quantum cryptography.

The implementation of a discrete Quantum Fourier Transform (QFT) on a quantum computer hinges on basic quantum gates [1], such as the Hadamard gate and the controlled phase-shift gate. As depicted by the quantum circuit in Figure 4.1, the circuit takes an n-qubit input and carries out the QFT as follows:

$$|x_1 x_2 \cdots x_n\rangle \xrightarrow{\text{QFT}} \frac{1}{2^{n/2}} \sum_{y=1}^{2^n-1} e^{i2\pi \cdot x \cdot y/2^n} |y_1 y_2 \cdots y_n\rangle, \tag{4.1}$$

where n represents the total number of input, and $|x\rangle = x_1 x_2 \cdots x_n$ and $y = y_1 y_2 \cdots y_n$ denote the binary representations of the input and output qubits, respectively. In this equation, the box labeled H signifies a Hadamard gate. The box labeled R_k, where k ranges from 2 to n and is connected to the photonic qubit via a vertical line, represents a controlled phase-shift gate

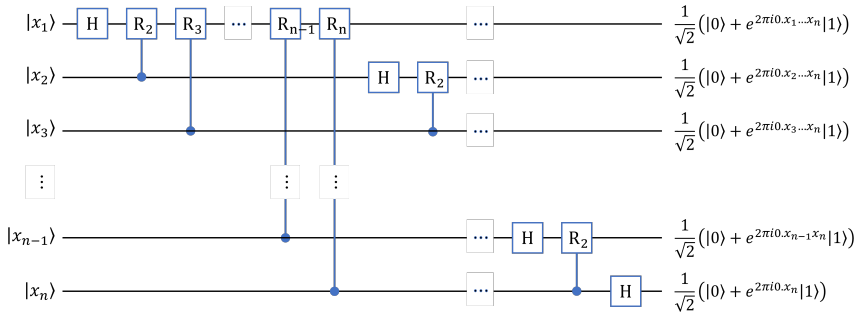

Figure 4.1: Circuit for the discrete quantum Fourier transform.

characterized by the matrix:

$$\mathrm{CR}_k = \begin{pmatrix} 1 & 0 & 0 & 0 \\ 0 & 1 & 0 & 0 \\ 0 & 0 & 1 & 0 \\ 0 & 0 & 0 & e^{i2\pi/2^k} \end{pmatrix}. \tag{4.2}$$

The QFT can be analogized to the role of the Fast Fourier Transform (FFT) in classical computing. The FFT is an algorithm that computes the discrete Fourier transform, thereby converting a mathematical function of time into a function of frequency. Conversely, the QFT transforms quantum states and superpositions from one basis to another, effectively transitioning the state of a quantum system from the computational basis to the Fourier basis. The potency of the QFT stems from its capacity to leverage quantum superposition and interference.

The QFT on n qubits can be devised as a quantum circuit encompassing $O(n^2)$ quantum gates, performing the discrete Fourier transform on 2^n amplitudes of quantum states. In contrast, the implementation of classical FFT requires $O(n2^n)$ gates. The inherent quantum nature of the QFT makes it exponentially faster than classical Fourier transforms for specific applications, thereby offering substantial computational acceleration, a characteristic that renders it an integral component of many quantum algorithms. It is crucial to note that for the QFT, we observe a se-

quence of probabilities for all potential outcomes upon measurement. However, as measurement collapses the quantum state to the computational basis, not every task that utilizes the classical Fourier transform can take advantage of the exponential speedup provided by the quantum Fourier transform.

The implementation of QFT has been proposed across various physical systems, and experimental demonstrations of small-scale implementations have been carried out using trapped ions and nuclear magnetic resonance. By extending this capability to photonics, we could significantly enhance photonic quantum technologies. This advancement would allow us to capitalize on the photon's inherent minimal interaction with the environment and its easy propagation through optical fibers.

4.2 Atom-Photon Interface Revisited

4.2.1 Controlled Phase-Shift Gate

In Section 2.2.2, we explored the use of the atom-photon interface to execute the controlled phase-flip (CZ) gate. However, the operation of the quantum Fourier transform (QFT) requires the implementation of the controlled phase-shift (CR_k) gate, which demands a fractional π phase shift as per Equation 4.2. Consequently, it's essential to revisit and expand upon the functionality of the atom-photon interface's capabilities.

We refer to the same physical system as detailed in Section 2.2.1, which includes an atom in a single-sided cavity as depicted in Figure 2.2(a). This system features atomic transitions of $|\uparrow\rangle \leftrightarrow |\Uparrow\rangle$ and $|\downarrow\rangle \leftrightarrow |\Downarrow\rangle$ coupling to the cavity mode in V-polarization. However, we now assume the system to possess a level structure as displayed in Figure 4.2, where both spin

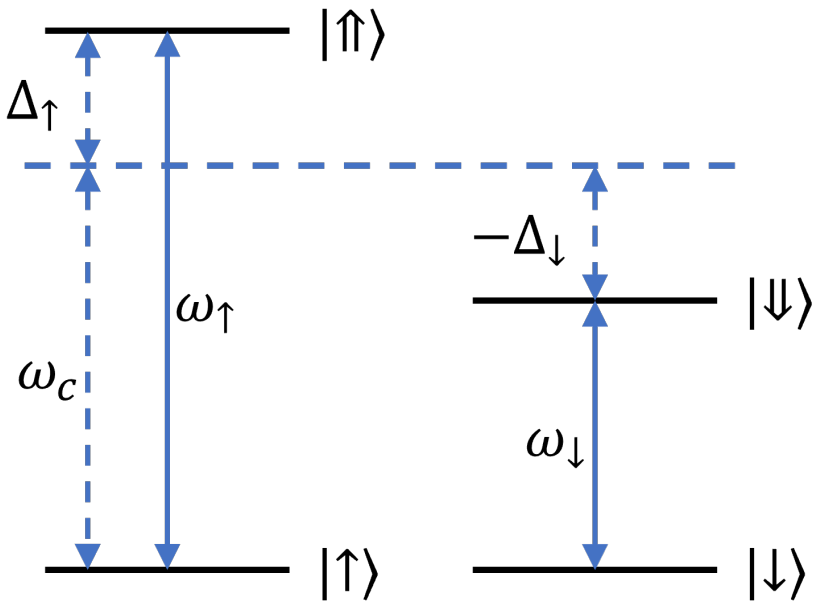

Figure 4.2: Level structure of the reengineered atom-cavity system.

transitions are detuned from the cavity mode, such that $\Delta_{\uparrow,\downarrow} = \omega_{\uparrow,\downarrow} - \omega_c$. Here, the spin-up atomic transition frequency is symbolized by $\omega_\uparrow$, the spin-down atomic transition frequency by $\omega_\downarrow$, and the cavity mode frequency by ω_c.

The reflection coefficient of a probe beam remains unchanged (for a detailed derivation, refer to Section 2.2.2), represented by

$$r_{\uparrow,\downarrow} = \frac{C_{\uparrow,\downarrow} - 1}{C_{\uparrow,\downarrow} + 1}. \tag{4.3}$$

In the above equation, $C_{\uparrow,\downarrow}$ denotes the atom-cavity cooperativity, defined as:

$$C_{\uparrow,\downarrow} = \frac{4g^2}{\gamma(\kappa + i2\Delta_{\uparrow,\downarrow})}, \tag{4.4}$$

where κ is the decay rate of the excited atom, and γ is the decay rate of the cavity mode. We also define the in-resonance cooperativity $C = 4g^2/\gamma\kappa$, which facilitates the relationship between the

in-resonance and spin-dependent cooperativities:

$$C_{\uparrow,\downarrow} = \frac{C}{1 + 2i\Delta_{\uparrow,\downarrow}/\kappa}. \tag{4.5}$$

In the strong coupling regime where $C \gg 1$, the reflection coefficient is given by $r_{\uparrow,\downarrow} = e^{i\theta_{\uparrow,\downarrow}}$, with

$$\theta_{\uparrow,\downarrow} = \mathrm{Im}\left\{\ln \frac{1 - i2\Delta_{\uparrow,\downarrow}/\kappa C}{1 + i2\Delta_{\uparrow,\downarrow}/\kappa C}\right\}, \tag{4.6}$$

a phase continuously adjustable from 0 to 2π by altering the detuning $\Delta_{\uparrow,\downarrow}$. After reflection, we apply a single-qubit phase gate of $\begin{pmatrix} 1 & 0 \\ 0 & e^{-i\theta_\uparrow} \end{pmatrix}$ on the photon. The reflection and the photonic phase gate implement a controlled phase-shift gate on the photon and atom, represented by

$$\mathrm{CR}\left(\Delta\theta\right) = \begin{pmatrix} 1 & 0 & 0 & 0 \\ 0 & 1 & 0 & 0 \\ 0 & 0 & 1 & 0 \\ 0 & 0 & 0 & e^{i\Delta\theta} \end{pmatrix}, \tag{4.7}$$

where $\Delta\theta = \theta_\downarrow - \theta_\uparrow$ is the relative phase shift. In these operators, the photonic state is denoted as $|H\rangle \equiv |0\rangle_p$ for H-polarization and $|V\rangle \equiv |1\rangle_p$ for V-polarization, the atomic state as $|\uparrow\rangle \equiv |0\rangle_a$ and $|\downarrow\rangle \equiv |1\rangle_a$, and the composite state space as $|x\rangle_p \otimes |y\rangle_a$.

4.2.2 Active Phase Tuning

The Quantum Fourier Transform (QFT) necessitates the sequential application of distinct CR_k gates. To accomplish this, rapid modulation of the detunings $\Delta_\uparrow$ and $\Delta_\downarrow$ is required. These

detunings are expressed as $\Delta_\uparrow = \omega_\uparrow - \omega_c$ and $\Delta_\downarrow = \Delta_\uparrow + \Delta_\mathrm{Z}$, with Δ_Z representing the Zeeman splitting of the spin transitions. Since Zeeman splitting is directly determined by the applied magnetic field, which is difficult to rapidly modulate, we employ a constant Zeeman splitting and actively adjust the atomic transitions via the quantum-confined Stark effect or AC Stark shift. This strategy facilitates the modulation of the detuning on nanosecond timescales, thereby enabling the swift alteration of the phase of the CR$_k$ gates.

We denote the spin-dependent detuning as $\Delta_\uparrow = \Delta_\mathrm{S} + \Delta_0$ and $\Delta_\downarrow = \Delta_\mathrm{S} + \Delta_\mathrm{Z} + \Delta_0$ under the influence of the Stark shift and Zeeman splitting, where Δ_S represents the Stark shift and Δ_0 signifies an offset. We set $\Delta_0 = \frac{\kappa}{2}\sqrt{C^2-1}$ and $\Delta_\mathrm{Z} = -2\Delta_0$, so that the controlled phase-shift $\Delta\theta = \pi$ when $\Delta_\mathrm{S} = 0$. The Zeeman splitting is determined by the magnetic field and is calculated as $\Delta_\mathrm{Z} = (g_e + g_h)\,\mu_B B/\hbar$, where g_e and g_h denote the Lande factors for the electron and hole, respectively, μ_B is the Bohr magneton, and B is the applied magnetic field.

Figure 4.3 1 illustrates the controlled phase-shift $\Delta\theta$ as a function of the Stark shift Δ_S, assuming parameters: $g_e = 0.43$, $g_h = 0.21$, $g = 11$ GHz, $\kappa = 0.3$ GHz, and $\gamma = 28$ GHz for the quantum dot-cavity system [119]. We further set the offset detuning to $\Delta_0 = 8.64$ GHz and apply a magnetic field of $B = 1.93$ T. The red markers indicate the specific Stark shifts utilized to implement CR$_k$ gates for $k = 1, 2, \cdots, 10$. With larger k values, the corresponding Stark shift scales as $\Delta_\mathrm{S} \sim \kappa C\sqrt{\frac{2^k}{2\pi}}$. Consequently, the implementation of a small phase shift of $\frac{2\pi}{2^k}$ demands high detuning, which may exceed practical values. However, we can omit the CR$_k$ gates when k exceeds a certain cutoff value K in the Fourier transform circuit. Since these gates exponentially approach an identity operation, omitting them introduces minimal error [124]. The state-of-the-art Stark shift can be achieved at ~ 1000 GHz for quantum dots [125], enabling the implementation of CR$_k$ gates with a maximum k of 14. This maximum is ample for a highly

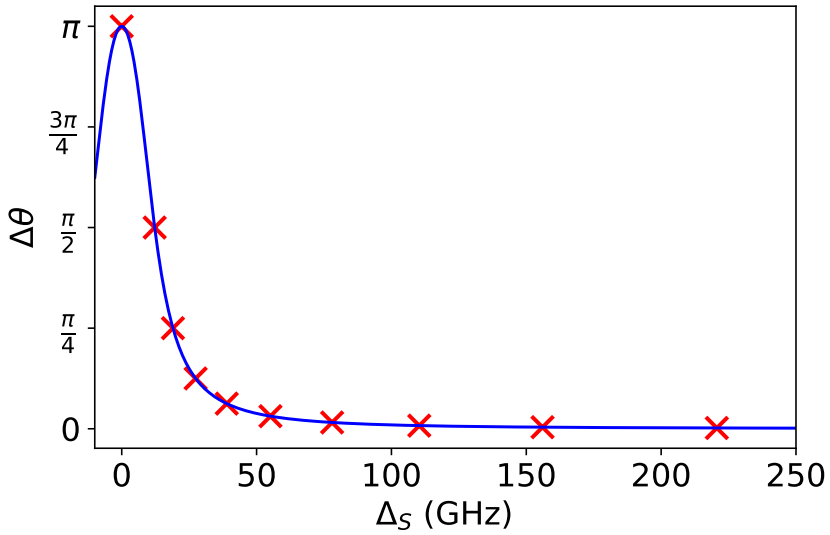

Figure 4.3: Plot of the controlled phase shift $\Delta\theta$ as a function of the Stark shift Δ_S.

accurate quantum Fourier transform.

4.3 Implementation of the Optical Quantum Fourier Transform

We employ an atom-photon interface to execute the discrete quantum Fourier transform (QFT). Figure 4.4(a) illustrates the circuit for the optical implementation of the QFT. The setup accepts an atomic qubit and n photons as input. We utilize the atom to mediate the interactions among the photons. The vertical line with crossed ends signifies a swap gate, which interchanges states between the atom and the photons. The box labeled H represents a Hadamard gate, while the box labeled R_k, linked to the photonic qubit via a vertical line, denotes the controlled phase-shift gate. Upon the completion of the transform, the first photon can be disregarded since it carries the ancilla's initial state.

The circuit comprises n subroutines. The first subroutine, demarcated by the dashed box in the figure, facilitates a swap gate between the ancilla and the first photon, which then exits

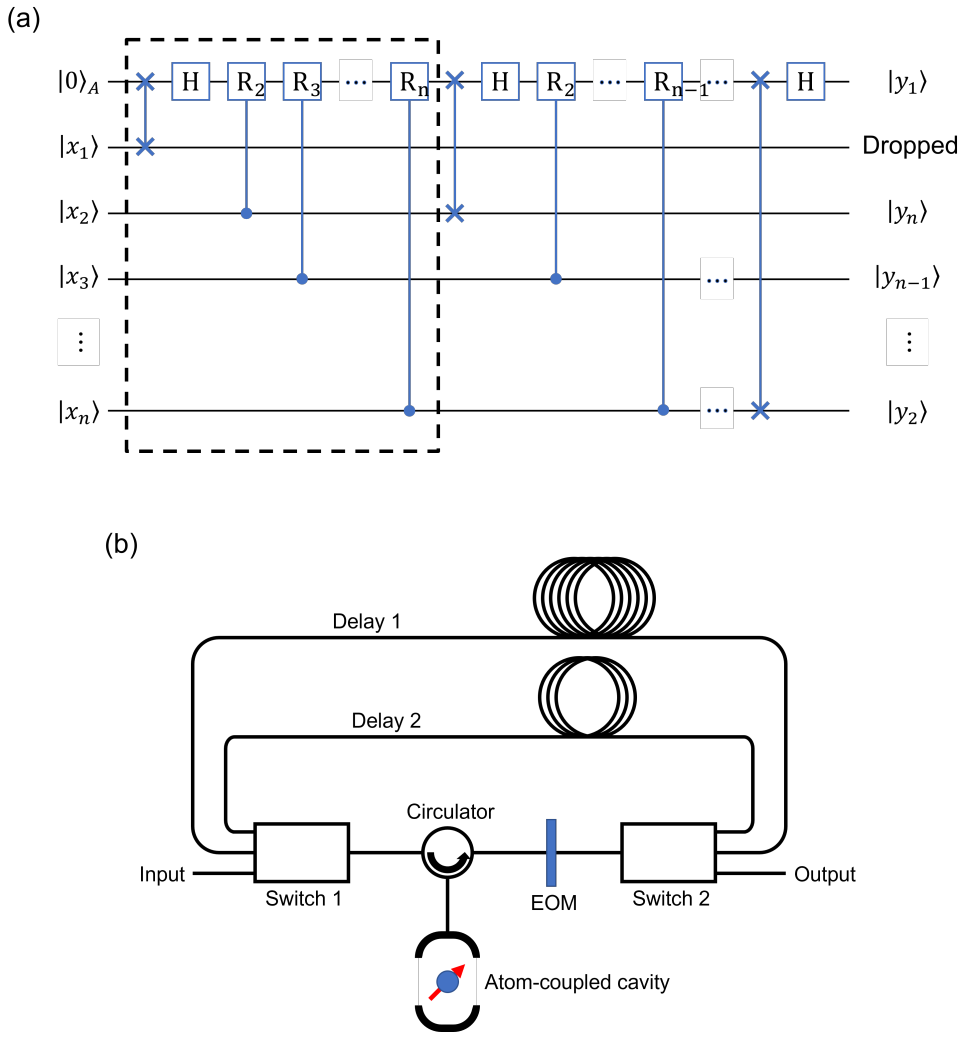

Figure 4.4: (a) Circuit designed for executing the quantum Fourier transform on photonic qubits. (b) Schematic setup for the photonic quantum Fourier transform.

the system. The ancilla subsequently applies a CR_k gate to the remaining photons 2 through n. The second subroutine repeats the process for the second photonic qubit, where a swap gate is applied and photon 2 departs the system. The ancilla then executes a CR_k gate on photons 3 to n. This procedure is reiterated until all the photons have vacated the system. Upon protocol completion, the atomic qubit houses the initial qubit of the Fourier transform. This qubit can be directly measured from the atom or, alternatively, another photon can be injected into the system and a swap operation can be executed to transfer the state back to an all-photonic Hilbert space.

In order to execute the quantum circuit, we propose the optical setup depicted in Figure 4.4(b). The ancillary qubit is a single atom connected to an optical cavity, which mediates robust interactions with the photons, thereby facilitating the generation of the CR_k gates. The photons are sequentially injected into the system, with each injection separated by an operation cycle time, denoted as T_{cycle}. In order to actualize the sequence of subroutines, we make use of two time-delay feedback loops and a pair of switches. Delay 1 produces a delay of $\tau_1 > nT_{\mathrm{cycle}}$, which retains the residual qubits following each subroutine execution, to be utilized in the subsequent subroutine. Delay 2, on the other hand, yields a delay of $\tau_2 \ll T_{\mathrm{cycle}}$. This brief delay permits a single photon to interact multiple times with the atomic qubit, which is an essential requirement for the creation of a swap gate.

The protocol begins with the injection of all n photons at the input. To effectuate the swap gate, we repeatedly reflect photon 1 off the cavity three times, facilitated by Delay 2. Each reflection implements a CR_1 gate between the photon and the atom. The amalgamation of the three CR_1 gates along with the Hadamard gates realizes the swap gate between the photon and

the atom, in accordance with the identity:

$$\text{SWAP} = H_{\text{a,p}} \cdot \text{CR}_1 \cdot H_{\text{a,p}} \cdot \text{CR}_1 \cdot H_{\text{a,p}} \cdot \text{CR}_1, \tag{4.8}$$

Here, $H_{\text{a,p}} = H_{\text{a}} \otimes H_{\text{p}}$ denotes a Hadamard gate applied both to the atom [86, 126] and the photon [52]. Following these reflections, photon 1 exits the system from the output. The remaining $n-1$ photons then sequentially reflect off the cavity, thereby executing the controlled phase-shift gates, and subsequently enter Delay 1. This route enables their transmission back to the input for the second subroutine. This process is iteratively repeated until all photons exit the system. The output then comprises the states following the execution of the QFT.

Chapter 5: Error Metric for Non-Trace-Preserving Operations

5.1 Quantum Error Correction and Threshold

For effective implementation of fault-tolerant quantum computing, quantum error correction is imperative [17]. This scheme is primarily designed to safeguard quantum information from errors due to decoherence and other quantum noise. The key principle underpinning quantum error correction lies in the distribution of a logical qubit across several physical qubits. In the event of an error in one of the qubits, the remaining qubits' data can be used to correct the error.

The concept of quantum error correction can be elucidated using the example of a 3-qubit error-correcting code, termed the "bit-flip code". Let's assume that a qubit is in state $|\psi\rangle = \alpha|0\rangle + \beta|1\rangle$. The bit-flip code associates the state $|0\rangle$ with $|000\rangle$ and the state $|1\rangle$ with $|111\rangle$. Consequently, state $|\psi\rangle$ is encoded as $|\psi'\rangle = \alpha|000\rangle + \beta|111\rangle$. In a scenario where a bit-flip (X) error impacts a qubit, state $|\psi'\rangle$ transforms into $\alpha|100\rangle + \beta|011\rangle$. Then, a majority vote is conducted to determine the original state. For each individual qubit, if its state disagrees with the others, it is deemed erroneous. The correct qubit state is then restored by flipping the erroneous qubit.

Real quantum error-correcting scheme should effectively address both bit-flip (X) and phase-flip (Z) errors. As an example, the depolarizing channel can be characterized by an error

probability (p). The effect of the depolarizing channel on a single qubit is expressed as follows:

$$\mathcal{E}(\rho) = (1-p)\rho + \frac{p}{3}\left(X\rho X + Y\rho Y + Z\rho Z\right), \tag{5.1}$$

where $\mathcal{E}$ is defined as a quantum operation, a process that transforms the input density operator ρ into another density operator. In general, a quantum operation holds important attributes such as the preservation of both positivity and the trace of a density operator, thereby classifying it as a completely positive and trace-preserving (CPTP) map. Equation 5.1 signifies that the qubit remains unaffected with a probability of $1-p$, and each of the Pauli operators, X, Y, and Z, are applied to the qubit with a probability of $p/3$. The fidelity of states passing through a depolarizing channel can be calculated as follows:

$$F = 1 - \frac{p}{3} + O(p^2). \tag{5.2}$$

Drawing on the discussions in [1], let's assume that a single qubit of information is encoded in an n-qubit quantum code capable of correcting errors on any single qubit. Let's also suppose that the depolarizing channel with parameter p acts independently on each of the qubits. This results in a joint action on all n qubits expressed as

$$\mathcal{E}^{\otimes n}(\rho) = (1-p)^n\rho + \sum_{j=1}^{3}\sum_{k=1}^{3}(1-p)^{n-1}\frac{p}{3}\sigma_k^j\rho\sigma_k^j + \cdots, \tag{5.3}$$

where $\cdots$ symbolizes higher-order terms that are positive and excluded from the analysis. After error correction, denoted as $\mathcal{R}$, has been executed, all terms appearing in this sum will revert to

the original state ρ,

$$\left(\mathcal{R} \circ \mathcal{E}^{\otimes n}\right)(\rho) = \left[(1-p)^n + n(1-p)^{n-1}p\right]\rho + \cdots . \tag{5.4}$$

This ensures that the fidelity is conforming to

$$\begin{aligned} F &\geq \sqrt{(1-p)^{n-1}(1-p+np)} \\ &= 1 - \frac{n(n-1)}{4}p^2 + O\left(p^3\right) \end{aligned} \tag{5.5}$$

By comparing the equation above with Equations 5.2, one can estimate a threshold, p_{th}, by solving:

$$\frac{n(n-1)}{4}p_{\text{th}}^2 < \frac{p_{\text{th}}}{3}. \tag{5.6}$$

Thus, if the error probability p is less than p_{th}, implementing the quantum error-correcting code can result in enhanced fidelity. Moreover, the principle of fault-tolerant quantum computing suggests that if the physical error rate is below the threshold, the logical error rate can be suppressed almost to zero using a concatenated code [70]. This paves the way for achieving scalable quantum computing.

However, it is important to note that not all noisy channels can be interpreted by a composite of Pauli operators. Consider, for instance, amplitude damping represented as:

$$\mathcal{E}_d(\rho) = E_0 \rho E_0^\dagger + E_1 \rho E_1^\dagger, \tag{5.7}$$

which encompasses operation elements E_0 and E_1 as:

$$E_0 = \begin{pmatrix} 1 & 0 \\ 0 & \sqrt{\gamma} \end{pmatrix}, \quad E_1 = \begin{pmatrix} 0 & \sqrt{\gamma} \\ 0 & 0 \end{pmatrix}. \tag{5.8}$$

Here, the parameter γ represents the strength of the amplitude damping process. As γ approaches zero, the strength of damping diminishes, leading ultimately to a noise-free quantum channel. When evaluating this error model, it becomes necessary to quantify the error using another measure, thereby deriving a threshold. If the error strength is less than this threshold, fault-tolerance can be assured.

5.2 Error Measure and Diamond Distance

A quantum operation, $\mathcal{E}$, signifies a map between the input and output states, denoted as $\rho_{\text{out}} = \mathcal{E}(\rho_{\text{in}})$. The measure of distance between two quantum operations gauges the divergence in their output states when subjected to identical input states. Any proper measure of distance, denoted as $\Delta(\mathcal{E}, \mathcal{F})$, between quantum operations $\mathcal{E}$ and $\mathcal{F}$, should adhere to the following mathematical properties [127]:

1. ***Metric***: For distance to serve as a metric, it must satisfy three conditions: (a) $\Delta(\mathcal{E}, \mathcal{F}) \geq 0$, where $\Delta(\mathcal{E}, \mathcal{F}) = 0$ only if $\mathcal{E} = \mathcal{F}$; (b) symmetry, implying $\Delta(\mathcal{E}, \mathcal{F}) = \Delta(\mathcal{F}, \mathcal{E})$; and (c) the triangle inequality, $\Delta(\mathcal{E}, \mathcal{F}) \leq \Delta(\mathcal{E}, \mathcal{G}) + \Delta(\mathcal{G}, \mathcal{F})$.

2. ***Chaining***: The measure $\Delta(\mathcal{E}_2 \circ \mathcal{E}_1, \mathcal{F}_2 \circ \mathcal{F}_1) \leq \Delta(\mathcal{E}_1, \mathcal{F}_1) + \Delta(\mathcal{E}_2, \mathcal{F}_2)$ should hold, where $\mathcal{E}_2 \circ \mathcal{E}_1$ indicates a composite process where operation $\mathcal{E}_1$ precedes operation $\mathcal{E}_2$ (similar for $\mathcal{F}$). This property ensures that the total distance of the composite operations

remains less than the sum of the distances in their respective steps.

3. ***Stability***: The property $\Delta(\mathcal{E} \otimes \mathcal{I}, \mathcal{F} \otimes \mathcal{I}) = \Delta(\mathcal{E}, \mathcal{F})$ should be maintained, where $\mathcal{I}$ denotes the identity operation in an extra state space. This ensures that the distance remains invariant when the operations act on a subsystem that can be entangled with other systems.

In practice, the distance between an experimentally implemented quantum operation and the ideal one is typically of interest, where the distance measure also serves as an error measure. The properties of chaining and stability are particularly useful for analyzing large and complex quantum information processing tasks, which involve sequential applications of quantum operations. These properties allow us to constrain the error of the entire process using the summation of the distances of the sequential operations.

The diamond distance [69] provides a way of quantifying the distance between two quantum operations, often expressed as completely positive trace-preserving (CPTP) maps. The diamond distance, symbolized as $d_\diamond(\mathcal{E}, \mathcal{F})$, between channels $\mathcal{E}$ and $\mathcal{F}$ is articulated as follows:

$$d_\diamond(\mathcal{E}, \mathcal{F}) = \frac{1}{2} \max_\rho \|(\mathcal{E} \otimes \mathcal{I}_R)(\rho) - (\mathcal{F} \otimes \mathcal{I}_R)(\rho)\|_1 , \tag{5.9}$$

In this expression, $\|\cdot\|_1$ represents the trace norm, $\mathcal{E}$ and $\mathcal{F}$ denote two quantum channels mapping quantum states from the input space X to the output space Y, $\mathcal{I}_R$ stands for the identity operation on an auxiliary space R, and ρ is a quantum state within the extended space $X \otimes R$.

The diamond distance quantifies the maximum trace distance between the output states that are produced by two quantum channels when they are provided with identical input states. This distance adheres to the three essential properties required of a distance measure for quantum

operations. Firstly, the metric property, which is inherently a characteristic of the trace norm. Secondly, the chaining property, which can be substantiated using the triangle inequality inherent in the trace norm. Lastly, the stability property, which is maintained as long as the dimension of the input space X is less than or equal to the dimension of the auxiliary space R [128]. Although no explicit formula currently exists to compute the diamond distance for general quantum channels, one can calculate it via convex optimization [68].

In the context of fault-tolerant quantum computing, the aim is to minimize the diamond distance between the implemented and ideal operations. If this distance surpasses a certain threshold value, the errors might accumulate and become uncorrectable, resulting in quantum computation failure. Conversely, if the diamond distance is below this threshold, errors can, in theory, be corrected more rapidly than they emerge, thus enabling reliable quantum computations.

5.3 General Distance for Non-Trace-Preserving Operations

5.3.1 Characteristic of Non-Trace-Preserving Errors

Real quantum systems often encounter non-trace-preserving errors, which stand in contrast to the idealized completely positive trace-preserving (CPTP) linear maps. A significant example of such an error is leakage, a scenario where qubits venture outside the computational subspace. For instance, atoms in excited states might spontaneously decay to irrelevant low-energy states, resulting in leakage. Such leakage can occur in a wide array of quantum computing platforms, including optics [47], superconducting circuits [129, 130], quantum dots [131], neutral atoms [132, 133], trapped ions [134], and topological qubits [135, 136].

Leakage errors pose serious issues as they corrupt the subspace encoding and invalidate

standard quantum error-correcting codes with syndrome measurements [17], which only convey information about error events restricted to a subspace. One approach to mitigating leakage errors employs the detect-and-reset method [137, 138], where each qubit undergoes continual monitoring for leakage. Upon detection of a leak event, the qubit in question can be discarded, replaced with an initialized state in the computational subspace, and then restored via a standard error-correcting scheme. However, this method may also introduce measurement-induced errors, as the detection process could inadvertently reveal the state of the qubit.

Furthermore, many quantum algorithms employ post-selection, a process that involves manipulating qubits based on measurement outcomes. An ideal post-selected protocol should present a uniform measurement probability regardless of the input state and should not reveal any information about that state. However, errors such as improperly prepared ancilla can break this symmetry, leading to biased measurements that divulge information about the input state. This disruption introduces additional disturbances beyond the original error. Because the channels corresponding to each measurement are non-trace-preserving, conventional error measures designed for trace-preserving operations cannot effectively quantify these imperfections. Therefore, an error measure specifically designed for non-trace-preserving operations is needed.

5.3.2 Defining the General Distance

The general distance, also referred to as the modified diamond distance [139], is given by

$$d_g\left(\mathcal{E},\mathcal{F}\right)=\frac{1}{2}\max_{\rho}\left\|\frac{\left(\mathcal{E}\otimes\mathcal{I}_R\right)\left(\rho\right)}{Tr\left[\left(\mathcal{E}\otimes\mathcal{I}_R\right)\left(\rho\right)\right]}-\frac{\left(\mathcal{F}\otimes\mathcal{I}_R\right)\left(\rho\right)}{Tr\left[\left(\mathcal{F}\otimes\mathcal{I}_R\right)\left(\rho\right)\right]}\right\|_1. \tag{5.10}$$

Here, $\|\cdot\|_1$ indicates the trace norm, $\mathcal{E}$ and $\mathcal{F}$ represent non-trace-preserving operations that map quantum states from input space X to output space Y. $\mathcal{I}_R$ is the identity operation on an auxiliary space R, and ρ is a quantum state in the expanded space $X \otimes R$. These operations can be expanded into operator-sum representations as

$$\begin{aligned} \mathcal{E}(\rho) &= \sum_i A_i \rho A_i^\dagger, \\ \mathcal{F}(\rho) &= \sum_j B_j \rho B_j^\dagger, \end{aligned} \tag{5.11}$$

where A_i and B_j are Kraus operators fulfilling $\sum_i A_i^\dagger A_i \leq I$ and $\sum_j B_j^\dagger B_j \leq I$. The general distance quantifies the deviation between two non-trace-preserving quantum operations as the maximum trace distance between their normalized output states. If operations $\mathcal{E}$ and $\mathcal{F}$ are trace-preserving, with $Tr[\mathcal{E}(\rho)] = 1$ and $Tr[\mathcal{F}(\rho)] = 1$, the general distance simplifies to the conventional diamond distance.

The primary challenge in using Equation 5.10 as an error metric is its inefficient computability. Unlike the diamond distance, which can be computed via convex optimization, Equation 5.10 does not present a convex problem. Consequently, I propose a metric that serves as an upper bound for the general distance.

5.3.3 Upper Bound for General Distance

To establish the upper bound, we initially depict the two quantum operations in Equation 5.10 via Stinespring dilation [68] as follows:

$$\begin{aligned} \mathcal{E}(\rho) &= Tr_Z\left\{\hat{A}\rho\hat{A}^\dagger\right\}, \\ \mathcal{F}(\rho) &= Tr_Z\left\{\hat{B}\rho\hat{B}^\dagger\right\}, \end{aligned} \tag{5.12}$$

where $\hat{A} = \sum_i e_i \otimes A_i$, $\hat{B} = \sum_j e_j \otimes B_j$, and e_i and e_j are the basis on a reference space Z. The general distance satisfies the stability property and is maximized over the set of pure states in the extended space $X \otimes R$ (for a detailed derivation, see Appendix 5.A). Consequently, we can recast Equation 5.10 as:

$$d_g(\mathcal{E},\mathcal{F}) = \frac{1}{2}\max_{\psi}\left\| Tr_Z\left\{\frac{\hat{A}\psi\psi^\dagger\hat{A}^\dagger}{\psi^\dagger\hat{A}^\dagger\hat{A}\psi} - \frac{\hat{B}\psi\psi^\dagger\hat{B}^\dagger}{\psi^\dagger\hat{B}^\dagger\hat{B}\psi}\right\}\right\|_1, \tag{5.13}$$

where ψ denotes a pure state in the expanded input space $X \otimes R$, and we have simplified $\hat{A} \otimes I_R$ as $\hat{A}$ and $\hat{B} \otimes I_R$ as $\hat{B}$.

Equation 5.13 can be bounded through renormalization [140, 141]. The critical step involves applying the singular value decomposition to $\hat{B}\hat{A}^{-1}$, yielding $\hat{B}\hat{A}^{-1} = UMV^\dagger$. Here, U and V are isometries with dimensions of $k'm \times n$ and $km \times n$ respectively, while M is a nonnegative diagonal operator with a dimension of $n \times n$. Here, n and m are the dimensions of the input and output spaces of the quantum operations, and k and k' are the number of Kraus operators A_i

and B_j. We define two renormalized trace-preserving operations as follows:

$$\begin{aligned} \mathcal{U}(\rho) &= Tr_Z\left\{U\rho U^\dagger\right\}, \\ \mathcal{V}(\rho) &= Tr_Z\left\{V\rho V^\dagger\right\}, \end{aligned} \tag{5.14}$$

and a normalizing operation as:

$$\mathcal{M}(\rho) = \frac{M\rho M}{Tr\left[M\rho M\right]}. \tag{5.15}$$

Employing these definitions, we demonstrate in Appendix 5.B that the general distance can be upper-bounded by:

$$d_g(\mathcal{E},\mathcal{F}) \leq d_\diamond(\mathcal{U},\mathcal{V}) + d_g(\mathcal{I},\mathcal{M}). \tag{5.16}$$

In the above equation, $d_\diamond(\mathcal{U},\mathcal{V})$ represents the conventional diamond distance, which is calculable via convex optimization, and $d_g(\mathcal{I},\mathcal{M})$ represents a general distance between an identity operation and the normalizing operation, which we denote as the normalizing distance. We can compute $d_g(\mathcal{I},\mathcal{M})$ analytically as:

$$d_g(\mathcal{I},\mathcal{M}) = \frac{\lambda_{\max} - \lambda_{\min}}{\lambda_{\max} + \lambda_{\min}}, \tag{5.17}$$

where $\lambda_{\max}$ and $\lambda_{\min}$ are the maximum and minimum eigenvalues of M respectively (see Appendix 5.C for a detailed calculation). By combining $d_\diamond(\mathcal{U},\mathcal{V})$ and $d_g(\mathcal{I},\mathcal{M})$, we can establish an upper bound on the general distance between two non-trace-preserving quantum operations.

5.4 Applications of the Error Metric

The general distance holds considerable potential for application in fault-tolerant quantum computing. It supplies a worst-case error boundary for various error models and can be seamlessly integrated into the method proposed by Aharonov and Ben-Or [70] for estimating fault-tolerant thresholds. Furthermore, this metric can aid in analyzing fault tolerance using numerical simulations [142–144], via extending the method suggested by Magesan, et al. [145] to encompass non-trace-preserving operations.

Subsequent sections will delve into two primary applications of the error metric: assessing leakage in the atom-photon interface and analyzing leakage in neutral atoms. For a broader range of applications, readers are referred to [59], which includes discussions on the Knill-Laflamme-Milburn protocol for linear optical quantum computing [53], the quantum Zeno gate [146], and measurement-induced errors in other post-selected protocols.

5.4.1 Leakage in Atom-Photon Interface

We first apply the general distance to examine the leakage in the atom-photon interface, as discussed in Section 4.2. In the case of an atom-photon interface with active phasing tuning, the reflection and the single-photon phase gate implement a controlled phase-shift gate on the photon and atom, represented by

$$U_k = \begin{pmatrix} 1 & 0 & 0 & 0 \\ 0 & 1 & 0 & 0 \\ 0 & 0 & |r_\uparrow| & 0 \\ 0 & 0 & 0 & |r_\downarrow| \, e^{\frac{i\pi}{2^{k-1}}} \end{pmatrix}, \tag{5.18}$$

where $r_\uparrow$ and $r_\downarrow$ are the spin-dependent reflection coefficients, as given by Equation 4.3. The general distance between the imperfect reflection operation and an ideal CR_k gate can be defined as:

$$d_g\left(U_k, \mathrm{CR}_k\right) = \frac{1}{2} \max_{\rho} \left\| \frac{U_k \rho U_k^\dagger}{Tr\left[U_k \rho U_k^\dagger\right]} - \mathrm{CR}_k \rho \mathrm{CR}_k^\dagger \right\|_1, \tag{5.19}$$

where we simplify $U_k \otimes I$ to U_k and $\mathrm{CR}_k \otimes I$ to CR_k for brevity and clarity. This distance can be interpreted as a measure between a weak-measurement operation and the identity channel. Based on Equation 5.17, this distance is determined as follows:

$$d_g\left(U_k, \mathrm{CR}_k\right) = \frac{1 - \min\left(|r_\uparrow|, |r_\downarrow|\right)}{1 + \min\left(|r_\uparrow|, |r_\downarrow|\right)}. \tag{5.20}$$

In the strong coupling regime, this approximates $\frac{1}{2C^2}$, where C denotes the atom-cavity cooperativity. Given an error rate threshold of 10^{-5} [147], the corresponding cooperativity is estimated to be $C > 220$, a level that is attainable in interfaces that use quantum dots as atomic qubits.

5.4.2 Leakage in Neutral Atoms

We analyze leakage errors specific to neutral-atom quantum computers. Leakage errors occur when qubits exit the computational subspace. In the context of neutral-atom quantum computers, qubits are encoded in metastable states. To entangle these qubits, atoms are typically driven to highly excited Rydberg states, which can spontaneously decay into irrelevant low-energy states, causing leakages. These leakages are the primary errors in neutral atoms [132, 133] and present significant issues. They corrupt subspace encoding and render the standard quantum error-correcting codes with syndrome measurements ineffective, as these measurements only pro-

vide information about error events within a specific subspace [148].

One approach to mitigating leakage errors utilizes the detect-and-reset method [137, 138]. Here, each qubit is continuously monitored for leakages. Upon detection of a leak event, the affected qubit is discarded, replaced with an initialized state within the computational subspace, and then restored using a standard error-correcting scheme. Wu et al. [132] have explored the application of the detect-and-reset method to neutral-atom quantum computers. They make the assumption that each atom carries a leakage probability of p. Upon detecting a leak event, they reset the qubit to state $|0\rangle$ and restore it using the XZZX surface code [149]. However, if a non-leak event is detected, the qubit undergoes a non-trace-preserving operation

$$\mathcal{E}_K(\rho) = \frac{K\rho K^\dagger}{Tr\left[K\rho K^\dagger\right]}, \tag{5.21}$$

where $K = I + \left(\sqrt{1-p} - 1\right)|1\rangle\langle 1|$ is the non-leak operator. They apply the Pauli twirling approximation [150] to operator K and approximate the operation as a channel that imposes a Pauli-Z error at a rate proportional to p^2. This error is then considered negligible since it scales quadratically, while other leakage errors due to detection inefficiencies scale linearly. With this approximation, the authors concluded that they could correct 98% of leakage errors. However, the Pauli twirling approximation only applies to trace-preserving linear maps. Hence, it's crucial to revisit the analysis using a metric suitable for non-trace-preserving operations.

We now apply our metric to this model. The undetected leakage channel is given by $\mathcal{E}_{\text{leak}}(\rho) = K\rho K^\dagger + L\rho L^\dagger$, where K is the non-leak operator, and $L = \sqrt{p}\,|e\rangle\langle 1|$ is the operator representing a qubit's leakage from computational state $|1\rangle$ to irrelevant state $|e\rangle$. We can

quantify the error of the undetected leakage channel by the diamond distance

$$d_{\text{leak}} = d_{\diamond}\left(\mathcal{E}_{\text{leak}}, \mathcal{I}\right), \tag{5.22}$$

where $\mathcal{I}$ is the identity channel, and derive $d_{\text{leak}} = p$. In the detect-and-reset method, assuming a detection efficiency of γ, the post-selected channel is given

$$\mathcal{E}_{\text{post}}\left(\rho\right) = \frac{K\rho K^{\dagger} + \left(1-\gamma\right) L\rho L^{\dagger}}{Tr\left[K\rho K^{\dagger} + \left(1-\gamma\right) L\rho L^{\dagger}\right]}, \tag{5.23}$$

Its error should be measured by the general distance $d_{\text{post}} = d_g\left(\mathcal{E}_{\text{post}}, \mathcal{I}\right)$. In the limit of perfect detection efficiency ($\gamma = 1$), $\mathcal{E}_{\text{post}}$ corresponds to the no-leak channel described only by operator K. We can calculate its distance by Equation 5.17 to obtain $d_{\text{post}} = \frac{1-\sqrt{1-p}}{1+\sqrt{1-p}}$, which is proportional to p and not p^2. It thus cannot be assumed as negligible and must be included in the error analysis.

For a comprehensive analysis, accounting for both detection inefficiencies and errors due to no-leak evolution, we define the error reduction rate $\eta = 1 - \frac{d_{\text{post}}}{d_{\text{leak}}}$. Figure 5.1 shows the error reduction rate as a function of leakage probability for several detection efficiencies. These plots provide a lower bound on the error reduction with the corresponding detection efficiency. In particular, the calculated error reduction rate with perfect detection efficiency is exact. Therefore, it imposes a tight upper bound on all error reductions of the detect-and-reset method, with an optimal rate of 75%. This result contrasts with the 98% reduction predicted by [132], which was assumed to be limited by detection inefficiencies.

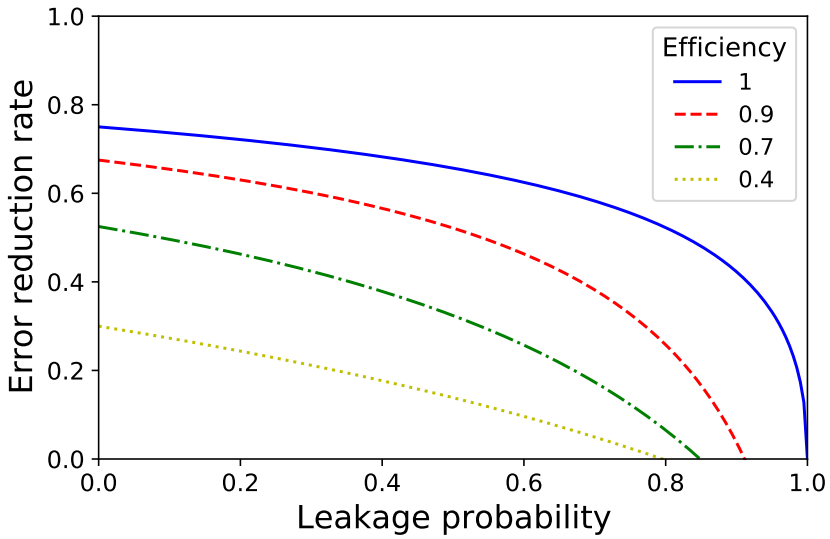

Figure 5.1: Error reduction rate as a function of leakage probability for different detection efficiencies.

Appendix 5.A Stability of the General Distance

The general distance between two non-trace-preserving quantum operations is characterized by

$$d_g\left(\mathcal{E},\mathcal{F}\right)=\frac{1}{2}\max_{\rho\in X\otimes R}\left\|\frac{\left(\mathcal{E}\otimes\mathcal{I}_R\right)\left(\rho\right)}{Tr\left[\left(\mathcal{E}\otimes\mathcal{I}_R\right)\left(\rho\right)\right]}-\frac{\left(\mathcal{F}\otimes\mathcal{I}_R\right)\left(\rho\right)}{Tr\left[\left(\mathcal{F}\otimes\mathcal{I}_R\right)\left(\rho\right)\right]}\right\|_1, \tag{5.24}$$

where $\mathcal{E}$ and $\mathcal{F}$ represent non-trace-preserving operations mapping states from the input space X to the output space Y. $\mathcal{I}_R$ denotes the identity operation on the auxiliary space R, and ρ signifies a quantum state on the extended space $X\otimes R$. We demonstrate that the distance adheres to stability, expressed as $d_g\left(\mathcal{E}\otimes\mathcal{I},\mathcal{F}\otimes\mathcal{I}\right)=d_g\left(\mathcal{E},\mathcal{F}\right)$, if $\dim\left(X\right)\leq\dim\left(R\right)$, where $\mathcal{I}$ symbolizes the identity operation within another state space. Furthermore, this distance is optimized over a pure state within the space $X\otimes R$. This proof can be seen as a generalization of Lemma 3.45 in [128].

To begin, we purify the quantum state ρ by introducing another auxiliary space, denoted R'. This results in $\rho=Tr_{R'}\left[uu^{\dagger}\right]$, where u is a pure state on the combined space $X\otimes R\otimes R'$. The

general distance between two non-trace-preserving quantum operations, $\mathcal{E}$ and $\mathcal{F}$, is presented as:

$$d_g(\mathcal{E},\mathcal{F}) = \frac{1}{2}\max_{u\in X\otimes R\otimes R'}\left\| Tr_{R'}\left\{ \frac{\sum_i A_i uu^\dagger A_i^\dagger}{Tr\left[\sum_i A_i uu^\dagger A_i^\dagger\right]} - \frac{\sum_j B_j uu^\dagger B_j^\dagger}{Tr\left[\sum_j B_j uu^\dagger B_j^\dagger\right]} \right\}\right\|_1 . \tag{5.25}$$

In the equation above, the operations are represented in the operator-sum form, with $\mathcal{E}(\rho) = \sum_i A_i \rho A_i^\dagger$ and $\mathcal{F}(\rho) = \sum_j B_j \rho B_j^\dagger$. Here, A_i and B_j denote the Kraus operators satisfying $\sum_i A_i^\dagger A_i \leq I$ and $\sum_j B_j^\dagger B_j \leq I$, and we simplify $A_i \otimes I$ to A_i and $B_j \otimes I$ to B_j. Utilizing the contractility of the trace distance, as outlined in [1], where

$$\frac{1}{2}\left\|Tr_{R'}(\sigma_1-\sigma_2)\right\|_1 \leq \frac{1}{2}\left\|\sigma_1-\sigma_2\right\|_1, \tag{5.26}$$

and where σ_1 and σ_2 are two distinct quantum states, we can express an upper bound for Equation 5.25 as:

$$d_g(\mathcal{E},\mathcal{F}) \leq \frac{1}{2}\max_{u\in X\otimes R\otimes R'}\left\| \frac{\sum_i A_i uu^\dagger A_i^\dagger}{Tr\left[\sum_i A_i uu^\dagger A_i^\dagger\right]} - \frac{\sum_j B_j uu^\dagger B_j^\dagger}{Tr\left[\sum_j B_j uu^\dagger B_j^\dagger\right]} \right\|_1 . \tag{5.27}$$

We now proceed to demonstrate that the bound in Equation 5.27 is indeed tight. By applying the Schmidt decomposition to state u, we obtain $u = \sum_{l=1}^{n} \sqrt{p_l} x_l \otimes z_l$, where p_l denotes the Schmidt coefficient, x_l and z_l are bases on spaces X and $R \otimes R'$ respectively, and n is the dimension of space X. Assuming that $\dim(X) \leq \dim(R)$, we can select a pure state $v \in X \otimes R$ such that $v = \sum_{l=1}^{n} \sqrt{p_l} x_l \otimes e_l$, where e_l represents a basis in space R. We can then construct an

isometry $U\left(R, R \otimes R'\right)$ defined as $U = \sum_{l=1}^{n} z_l e_l^{\dagger}$. This results in $u = \left(I_X \otimes U\right) v$ and

$$\begin{aligned}
\frac{\sum_i A_i u u^{\dagger} A_i^{\dagger}}{Tr\left[\sum_i A_i u u^{\dagger} A_i^{\dagger}\right]} &= \frac{\sum_i \left(A_i \otimes U\right) v v^{\dagger} \left(A_i^{\dagger} \otimes U^{\dagger}\right)}{Tr\left[\sum_i \left(A_i \otimes U\right) v v^{\dagger} \left(A_i^{\dagger} \otimes U^{\dagger}\right)\right]} \\
&= \frac{\sum_i \left(I \otimes U\right) A_i v v^{\dagger} A_i^{\dagger} \left(I \otimes U^{\dagger}\right)}{Tr\left[\sum_i \left(I \otimes U\right) A_i v v^{\dagger} A_i^{\dagger} \left(I \otimes U^{\dagger}\right)\right]} \\
&= \left(I \otimes U\right) \frac{\sum_i A_i v v^{\dagger} A_i^{\dagger}}{Tr\left[\sum_i A_i v v^{\dagger} A_i^{\dagger}\right]} \left(I \otimes U^{\dagger}\right),
\end{aligned} \tag{5.28}$$

and we can similarly express the quantum operation $\mathcal{F}$ as

$$\frac{\sum_j B_j u u^{\dagger} B_j^{\dagger}}{Tr\left[\sum_j B_j u u^{\dagger} B_j^{\dagger}\right]} = \left(I \otimes U\right) \frac{\sum_j B_j v v^{\dagger} B_j^{\dagger}}{Tr\left[\sum_j B_j v v^{\dagger} B_j^{\dagger}\right]} \left(I \otimes U^{\dagger}\right). \tag{5.29}$$

Given that the trace distance is invariant under isometry, we derive from Equation 5.27

$$\begin{aligned}
d_g\left(\mathcal{E}, \mathcal{F}\right) &\leq \frac{1}{2} \max_{u \in X \otimes R \otimes R'} \left\| \frac{\sum_i A_i u u^{\dagger} A_i^{\dagger}}{Tr\left[\sum_i A_i u u dag A_i^{\dagger}\right]} - \frac{\sum_j B_j u u^{\dagger} B_j^{\dagger}}{Tr\left[\sum_j B_j u u^{\dagger} B_j^{\dagger}\right]} \right\|_1 \\
&= \frac{1}{2} \max_{v \in X \otimes R} \left\| \left(I \otimes U\right) \left\{ \frac{\sum_i A_i v v^{\dagger} A_i^{\dagger}}{Tr\left[\sum_i A_i v v^{\dagger} A_i^{\dagger}\right]} - \frac{\sum_j B_j v v^{\dagger} B_j^{\dagger}}{Tr\left[\sum_j B_j v v^{\dagger} B_j^{\dagger}\right]} \right\} \left(I \otimes U^{\dagger}\right) \right\|_1 \\
&= \frac{1}{2} \max_{v \in X \otimes R} \left\| \frac{\sum_i A_i v v^{\dagger} A_i^{\dagger}}{Tr\left[\sum_i A_i v v^{\dagger} A_i^{\dagger}\right]} - \frac{\sum_j B_j v v^{\dagger} B_j^{\dagger}}{Tr\left[\sum_j B_j v v^{\dagger} B_j^{\dagger}\right]} \right\|_1 \\
&= \frac{1}{2} \max_{v \in X \otimes R} \left\| \frac{\left(\mathcal{E} \otimes \mathcal{I}_R\right)\left(v v^{\dagger}\right)}{Tr\left[\left(\mathcal{E} \otimes \mathcal{I}_R\right)\left(v v^{\dagger}\right)\right]} - \frac{\left(\mathcal{F} \otimes \mathcal{I}_R\right)\left(v v^{\dagger}\right)}{Tr\left[\left(\mathcal{F} \otimes \mathcal{I}_R\right)\left(v v^{\dagger}\right)\right]} \right\|_1.
\end{aligned} \tag{5.30}$$

Comparing Equation 5.30 with Equation 5.24, we observe that the pure state $v v^{\dagger}$ resides on a subset of the domain of the optimization variable ρ on space $X \otimes R$. Therefore, we conclude that when $\dim\left(X\right) \leq \dim\left(R\right)$, the general distance remains stable, and the distance is optimized

over a pure state v on space $X \otimes R$ such that

$$d_g\left(\mathcal{E},\mathcal{F}\right)=\frac{1}{2}\max_{v\in X\otimes R}\left\|\frac{\left(\mathcal{E}\otimes\mathcal{I}_R\right)\left(vv^\dagger\right)}{Tr\left[\left(\mathcal{E}\otimes\mathcal{I}_R\right)\left(vv^\dagger\right)\right]}-\frac{\left(\mathcal{F}\otimes\mathcal{I}_R\right)\left(vv^\dagger\right)}{Tr\left[\left(\mathcal{F}\otimes\mathcal{I}_R\right)\left(vv^\dagger\right)\right]}\right\|_1. \tag{5.31}$$

Appendix 5.B Renormalization of Quantum Operations

We can provide an upper bound for the general distance represented in Equation 5.10 using a renormalization process. Firstly, we present the two quantum operations in the Stinespring form [128], such that $\mathcal{E}\left(\rho\right)=Tr_Z\left\{\hat{A}\rho\hat{A}^\dagger\right\}$ and $\mathcal{F}\left(\rho\right)=Tr_Z\left\{\hat{B}\rho\hat{B}^\dagger\right\}$, where $\hat{A}=\sum_i e_i\otimes A_i$, $\hat{B}=\sum_j e_j\otimes B_j$, and e_i and e_j serve as bases on a reference space Z. We can rewrite the general distance between $\mathcal{E}$ and $\mathcal{F}$ as follows:

$$d_g\left(\mathcal{E},\mathcal{F}\right)=\frac{1}{2}\max_{v}\left\|Tr_Z\left\{\frac{\hat{A}vv^\dagger\hat{A}^\dagger}{v^\dagger\hat{A}^\dagger\hat{A}v}-\frac{\hat{B}vv^\dagger\hat{B}^\dagger}{v^\dagger\hat{B}^\dagger\hat{B}v}\right\}\right\|_1, \tag{5.32}$$

In the above equation, v signifies a pure state in the expanded state space $X\otimes R$. For simplicity, we denote $\hat{A}\otimes I_R$ as $\hat{A}$ and $\hat{B}\otimes I_R$ as $\hat{B}$, with I_R representing the identity operator on the auxiliary space R.

Next, we define a new state $\psi=\frac{\hat{A}v}{\left|\hat{A}v\right|}$ and reformulate Equation 5.32 as follows:

$$d_g\left(\mathcal{E},\mathcal{F}\right)=\frac{1}{2}\max_{\psi}\left\|Tr_Z\left\{\psi\psi^\dagger-\frac{\left(\hat{B}\hat{A}^{-1}\right)\psi\psi^\dagger\left(\hat{B}\hat{A}^{-1}\right)^\dagger}{\psi^\dagger\left(\hat{B}\hat{A}^{-1}\right)^\dagger\hat{B}\hat{A}^{-1}\psi}\right\}\right\|_1, \tag{5.33}$$

Here, $\hat{A}^{-1}$ represents the pseudoinverse of $\hat{A}$. Applying the singular value decomposition to $\hat{B}\hat{A}^{-1}$, we obtain $\hat{B}\hat{A}^{-1}=UMV^\dagger$. U and V are isometries with dimensions of $k'm\times n$ and

$km \times n$ respectively, while M is a nonnegative diagonal operator with a dimension of $n \times n$. Here, n and m denote the dimensions of the input and output spaces of the quantum operations, and k and k' represent the number of Kraus operators A_i and B_j respectively. Consequently, we rewrite Equation 5.33 as follows:

$$d_g\left(\mathcal{E},\mathcal{F}\right)=\frac{1}{2}\max_{\psi}\left\|Tr_Z\left\{\psi\psi^\dagger-\frac{UMV^\dagger\psi\psi^\dagger VMU^\dagger}{\psi^\dagger VM^2V^\dagger\psi}\right\}\right\|_1. \tag{5.34}$$

We now define a new state, $\phi=V^\dagger\psi$, and utilizing the triangular inequality, we can formulate an upper bound for Equation 5.34, as follows:

$$\begin{aligned} d_g\left(\mathcal{E},\mathcal{F}\right)&=\frac{1}{2}\max_{\phi}\left\|Tr_Z\left\{V\phi\phi^\dagger V^\dagger-\frac{UM\phi\phi^\dagger MU^\dagger}{\phi^\dagger M^2\phi}\right\}\right\|_1 \\ &=\frac{1}{2}\max_{\phi}\left\|Tr_Z\left\{V\phi\phi^\dagger V^\dagger-U\phi\phi^\dagger U^\dagger+U\phi\phi^\dagger U^\dagger-\frac{UM\phi\phi^\dagger MU^\dagger}{\phi^\dagger M^2\phi}\right\}\right\|_1 \\ &\leq\frac{1}{2}\max_{\phi}\left\|Tr_Z\left\{V\phi\phi^\dagger V^\dagger-U\phi\phi^\dagger U^\dagger\right\}\right\|_1+\frac{1}{2}\max_{\phi}\left\|\phi\phi^\dagger-\frac{M\phi\phi^\dagger M}{\phi^\dagger M^2\phi}\right\|_1. \end{aligned} \tag{5.35}$$

In the above calculations, we use the contractility property of trace distance [1], which states that the partial trace decreases the distance between two quantum states. This can be formally expressed as:

$$\left\|Tr_Z\left\{U\phi\phi^\dagger U^\dagger-\frac{UM\phi\phi^\dagger MU^\dagger}{\phi^\dagger M^2\phi}\right\}\right\|_1\leq\left\|\phi\phi^\dagger-\frac{M\phi\phi^\dagger M}{\phi^\dagger M^2\phi}\right\|_1 \tag{5.36}$$

We then introduce two renormalized quantum channels:

$$\begin{aligned} \mathcal{U}\left(\rho\right)&=Tr_Z\left\{U\rho U^\dagger\right\}, \\ \mathcal{V}\left(\rho\right)&=Tr_Z\left\{V\rho V^\dagger\right\}, \end{aligned} \tag{5.37}$$

and a normalizing operation:

$$\mathcal{M}(\rho) = \frac{M\rho M}{Tr[M\rho M]}. \tag{5.38}$$

Hence, we derive the following upper bound for the general distance between $\mathcal{E}$ and $\mathcal{F}$ from Equation 5.35:

$$d_g(\mathcal{E}, \mathcal{F}) \leq d_\diamond(\mathcal{U}, \mathcal{V}) + d_g(\mathcal{I}, \mathcal{M}), \tag{5.39}$$

Here, $d_\diamond(\mathcal{U}, \mathcal{V})$ is a diamond distance, calculable through convex optimization, and $d_g(\mathcal{I}, \mathcal{M})$ denotes a general distance between an identity operation and a normalizing operation, a value we refer to as the normalizing distance.

Appendix 5.C Calculation of the Normalizing Distance

We can directly compute the normalizing distance as:

$$d_g(\mathcal{I}, \mathcal{M}) = \frac{1}{2} \max_{\psi} \left\| \psi\psi^\dagger - \frac{M\psi\psi^\dagger M}{\langle\psi|M^2|\psi\rangle} \right\|_1, \tag{5.40}$$

where ψ is a pure quantum state, and M is a nonnegative diagonal operator of dimension $n \times n$. The normalized output state can be denoted as $|\phi\rangle = \frac{M|\psi\rangle}{|M|\psi\rangle|}$. Thus, the normalizing distance becomes

$$d_g(\mathcal{I}, \mathcal{M}) = \frac{1}{2} \max_{\psi} \left\| \psi\psi^\dagger - \phi\phi^\dagger \right\|_1. \tag{5.41}$$

The trace distance between two pure states is related to their inner product as

$$\frac{1}{2} \left\| \psi\psi^\dagger - \phi\phi^\dagger \right\|_1 = \sqrt{1 - |\langle\psi|\phi\rangle|^2}, \tag{5.42}$$

so maximizing $\left\|\psi\psi^\dagger - \phi\phi^\dagger\right\|_1$ is equivalent to minimizing $\cos\theta = |\langle\psi|\phi\rangle|$, with θ referring to the rotation angle between the input and output states.

We compute $\cos\theta$ through induction. We designate the normalizing operator as $M = \text{diag}\,(\lambda_1, \lambda_2, \cdots, \lambda_n)$, where $\lambda_1 \geq \lambda_2 \geq \cdots \geq \lambda_n \geq 0$. We first consider the projection of M on a l-dimensional subspace as $M_l = \text{diag}\,(\lambda_1, \lambda_2, \cdots, \lambda_l)$. A vector $|u\rangle$ on the subspace can be decomposed as $|u\rangle = \sqrt{x}\,|l\rangle + \sqrt{1-x}\,|v\rangle$, where $x \in [0,1]$, $|l\rangle$ is the basis of M corresponding to the eigenvalue λ_l, and $|v\rangle$ is a unit vector on the $(l-1)$-dimensional subspace orthogonal to $|l\rangle$. The assumption of positive coefficients does not lose generality because we can always redefine the basis with any phase. When we apply M_l to $|u\rangle$, we get

$$M_l\,|u\rangle = \lambda_l\sqrt{x}\,|l\rangle + \sqrt{1-x}M_{l-1}\,|v\rangle \ , \tag{5.43}$$

where M_{l-1} is the projection of M on the $(l-1)$-dimensional subspace. Application of M_{l-1} to $|v\rangle$ results in

$$M_{l-1}\,|v\rangle = r_{l-1}\cos\theta_{l-1}\,|v\rangle + r_{l-1}\sin\theta_{l-1}\,|v_\perp\rangle \ , \tag{5.44}$$

where r_{l-1} and θ_{l-1} are the contraction factor and rotation angle, respectively, and $|v_\perp\rangle$ represents a unit vector orthogonal to $|v\rangle$. A specific rotation axis doesn't affect the following calculation because the axis is always orthogonal to $|l\rangle$. The contraction factor and rotation angle of $M_l\,|u\rangle$ are given by $r_l = \sqrt{|\langle u|M_l^2|u\rangle|}$ and $\cos\theta_l = \langle u|M_l|u\rangle\,/r_l$, respectively. By combining Equations 5.43 and 5.44, we obtain

$$\begin{aligned} r_l^2 &= x\lambda_l^2 + (1-x)\,r_{l-1}^2, \\ r_l\cos\theta_l &= x\lambda_l + (1-x)\,r_{l-1}\cos\theta_{l-1}, \end{aligned} \tag{5.45}$$

i.e., $(r_l^2, r_l \cos\theta_l)$ is a convex combination of (λ_l^2, λ_l) and $\left(r_{l-1}^2, r_{l-1}\cos\theta_{l-1}\right)$. By induction, the feasible domain of $(r^2, r\cos\theta)$ for the normalizing operation $\mathcal{M}$ is given by

$$\begin{aligned} r^2 &= \sum_i x_i \lambda_i^2, \\ r\cos\theta &= \sum_i x_i \lambda_i, \end{aligned} \tag{5.46}$$

where x_i represents the coefficient of convex combination satisfying $\sum_i x_i = 1$, and λ_i is the eigenvalue of M. The minimum of $\cos\theta$ is on the boundary of the feasible domain depending on the combination of two eigenvalues. We can easily calculate the minimum of $\cos\theta$ using calculus, as follows:

$$\min\cos\theta = \frac{2\sqrt{\lambda_{\max}\lambda_{\min}}}{\lambda_{\max} + \lambda_{\min}}, \tag{5.47}$$

where $\lambda_{\max}$ and $\lambda_{\min}$ are the maximum and minimum eigenvalues of M, respectively. Therefore, the distance between the identity and normalizing operations is given by

$$d_g\left(\mathcal{I}, \mathcal{M}\right) = \frac{\lambda_{\max} - \lambda_{\min}}{\lambda_{\max} + \lambda_{\min}}. \tag{5.48}$$

Bibliography

[1] Michael A. Nielsen and Isaac L. Chuang. *Quantum Computation and Quantum Information: 10th Anniversary Edition*. Cambridge University Press, 2010.

[2] David Deutsch and Roger Penrose. Quantum theory, the church–turing principle and the universal quantum computer. *Proceedings of the Royal Society of London. A. Mathematical and Physical Sciences*, 400:97–117, 1997.

[3] Richard P. Feynman. Simulating physics with computers. *International Journal of Theoretical Physics*, 21:467–488, 1982.

[4] P. W. Shor. Algorithms for quantum computation: discrete logarithms and factoring. In *Proceedings 35th Annual Symposium on Foundations of Computer Science*, pages 124–134, 1994.

[5] Lov K. Grover. A fast quantum mechanical algorithm for database search. In *Proceedings of the Twenty-Eighth Annual ACM Symposium on Theory of Computing*, pages 212–219. Association for Computing Machinery, 1996.

[6] John Preskill. Quantum computing in the nisq era and beyond. *Quantum*, 2:79, 2018.

[7] Frank Arute, Kunal Arya, Ryan Babbush, Dave Bacon, Joseph C. Bardin, Rami Barends, Rupak Biswas, Sergio Boixo, Fernando G. S. L. Brandao, David A. Buell, et al. Quantum supremacy using a programmable superconducting processor. *Nature*, 574:505–510, 2019.

[8] Han-Sen Zhong, Hui Wang, Yu-Hao Deng, Ming-Cheng Chen, Li-Chao Peng, Yi-Han Luo, Jian Qin, Dian Wu, Xing Ding, Yi Hu, et al. Quantum computational advantage using photons. *Science*, 370:1460–1463, 2020.

[9] P.W. Shor. Fault-tolerant quantum computation. In *Proceedings of 37th Conference on Foundations of Computer Science*, pages 56–65, 1996.

[10] A. Einstein, B. Podolsky, and N. Rosen. Can quantum-mechanical description of physical reality be considered complete? *Physical Review*, 47:777–780, 1935.

[11] Daniel M. Greenberger, Michael A. Horne, and Anton Zeilinger. Going beyond bell's theorem. *Bell's Theorem, Quantum Theory and Conceptions of the Universe*, pages 69–72, 1989.

[12] Hans J. Briegel and Robert Raussendorf. Persistent entanglement in arrays of interacting particles. *Physical Review Letters*, 86:910–913, 2001.

[13] Robert Raussendorf and Hans J. Briegel. A one-way quantum computer. *Physical Review Letters*, 86:5188–5191, 2001.

[14] Christopher M. Dawson and Michael A. Nielsen. The solovay-kitaev algorithm. *Quantum Info. Comput.*, 6:81–95, 2006.

[15] Matt McEwen, Lara Faoro, Kunal Arya, Andrew Dunsworth, Trent Huang, Seon Kim, Brian Burkett, Austin Fowler, Frank Arute, Joseph C. Bardin, et al. Resolving catastrophic error bursts from cosmic rays in large arrays of superconducting qubits. *Nature Physics*, 18:107–111, 2022.

[16] Dorit Aharonov and Michael Ben-Or. Polynomial simulations of decohered quantum computers. In *Proceedings of 37th Conference on Foundations of Computer Science*, pages 46–55, 1996.

[17] Daniel Gottesman. Stabilizer codes and quantum error correction. *preprint arXiv:quant-ph/9705052*, 1997.

[18] A. Yu Kitaev. Fault-tolerant quantum computation by anyons. *Annals of Physics*, 303:2–30, 2003.

[19] Long B. Nguyen, Yen-Hsiang Lin, Aaron Somoroff, Raymond Mencia, Nicholas Grabon, and Vladimir E. Manucharyan. High-coherence fluxonium qubit. *Physical Review X*, 9:041041, 2019.

[20] Feng Bao, Hao Deng, Dawei Ding, Ran Gao, Xun Gao, Cupjin Huang, Xun Jiang, Hsiang-Sheng Ku, Zhisheng Li, Xizheng Ma, et al. Fluxonium: An alternative qubit platform for high-fidelity operations. *Physical Review Letters*, 129:010502, 2022.

[21] Shuo Ma, Alex P. Burgers, Genyue Liu, Jack Wilson, Bichen Zhang, and Jeff D. Thompson. Universal gate operations on nuclear spin qubits in an optical tweezer array of $^{171}\mathrm{Yb}$ atoms. *Physical Review X*, 12:021028, 2022.

[22] Alec Jenkins, Joanna W. Lis, Aruku Senoo, William F. McGrew, and Adam M. Kaufman. Ytterbium nuclear-spin qubits in an optical tweezer array. *Physical Review X*, 12:021027, 2022.

[23] Yosep Kim, Alexis Morvan, Long B. Nguyen, Ravi K. Naik, Christian Jünger, Larry Chen, John Mark Kreikebaum, David I. Santiago, and Irfan Siddiqi. High-fidelity three-qubit itoffoli gate for fixed-frequency superconducting qubits. *Nature Physics*, 18:783–788, 2022.

[24] Ivaylo S. Madjarov, Jacob P. Covey, Adam L. Shaw, Joonhee Choi, Anant Kale, Alexandre Cooper, Hannes Pichler, Vladimir Schkolnik, Jason R. Williams, and Manuel Endres. High-fidelity entanglement and detection of alkaline-earth rydberg atoms. *Nature Physics*, 16:857–861, 2020.

[25] Shuai Shi, Biao Xu, Kuan Zhang, Gen-Sheng Ye, De-Sheng Xiang, Yubao Liu, Jingzhi Wang, Daiqin Su, and Lin Li. High-fidelity photonic quantum logic gate based on near-optimal rydberg single-photon source. *Nature Communications*, 13:4454, 2022.

[26] C. J. Ballance, T. P. Harty, N. M. Linke, M. A. Sepiol, and D. M. Lucas. High-fidelity quantum logic gates using trapped-ion hyperfine qubits. *Physical Review Letters*, 117:060504, 2016.

[27] P. Gumann and J. Chow. Ibm scientists cool down the world's largest quantum-ready cryogenic concept system. IBM blog, 2022.

[28] Kenneth R. Brown, Jungsang Kim, and Christopher Monroe. Co-designing a scalable quantum computer with trapped atomic ions. *npj Quantum Information*, 2:16034, 2016.

[29] Loïc Henriet, Lucas Beguin, Adrien Signoles, Thierry Lahaye, Antoine Browaeys, Georges-Olivier Reymond, and Christophe Jurczak. Quantum computing with neutral atoms. *Quantum*, 4:327, 2020.

[30] Marcus W. Doherty, Neil B. Manson, Paul Delaney, Fedor Jelezko, Jörg Wrachtrup, and Lloyd C.L. Hollenberg. The nitrogen-vacancy colour centre in diamond. *Physics Reports*, 528:1–45, 2013.

[31] Nabeel Aslam, Hengyun Zhou, Elana K. Urbach, Matthew J. Turner, Ronald L. Walsworth, Mikhail D. Lukin, and Hongkun Park. Quantum sensors for biomedical applications. *Nature Reviews Physics*, 5:157–169, 2023.

[32] C. L. Degen, F. Reinhard, and P. Cappellaro. Quantum sensing. *Reviews of Modern Physics*, 89:035002, 2017.

[33] Christoph Kloeffel and Daniel Loss. Prospects for spin-based quantum computing in quantum dots. *Annual Review of Condensed Matter Physics*, 4:51–81, 2013.

[34] Jay M. Gambetta, Jerry M. Chow, and Matthias Steffen. Building logical qubits in a superconducting quantum computing system. *npj Quantum Information*, 3:2, 2017.

[35] Pieter Kok, W. J. Munro, Kae Nemoto, T. C. Ralph, Jonathan P. Dowling, and G. J. Milburn. Linear optical quantum computing with photonic qubits. *Reviews of Modern Physics*, 79:135–174, 2007.

[36] Michael A. Nielsen. Optical quantum computation using cluster states. *Physical Review Letters*, 93:040503, 2004.

[37] Sara Bartolucci, Patrick Birchall, Hector Bombín, Hugo Cable, Chris Dawson, Mercedes Gimeno-Segovia, Eric Johnston, Konrad Kieling, Naomi Nickerson, Mihir Pant, Fernando Pastawski, Terry Rudolph, and Chris Sparrow. Fusion-based quantum computation. *Nature Communications*, 14:912, 2023.

[38] Netanel H. Lindner and Terry Rudolph. Proposal for pulsed on-demand sources of photonic cluster state strings. *Physical Review Letters*, 103:113602, 2009.

[39] Daniel E. Browne and Terry Rudolph. Resource-efficient linear optical quantum computation. *Physical Review Letters*, 95:10501, 2005.

[40] Sophia E. Economou, Netanel Lindner, and Terry Rudolph. Optically generated 2-dimensional photonic cluster state from coupled quantum dots. *Physical Review Letters*, 105:093601, 2010.

[41] Mercedes Gimeno-Segovia, Pete Shadbolt, Dan E. Browne, and Terry Rudolph. From three-photon greenberger-horne-zeilinger states to ballistic universal quantum computation. *Physical Review Letters*, 115:020502, 2015.

[42] Mercedes Gimeno-Segovia, Terry Rudolph, and Sophia E. Economou. Deterministic generation of large-scale entangled photonic cluster state from interacting solid state emitters. *Physical Review Letters*, 123:070501, 2019.

[43] Hannes Pichler, Soonwon Choi, Peter Zoller, and Mikhail D. Lukin. Universal photonic quantum computation via time-delayed feedback. *Proceedings of the National Academy of Sciences*, 114:11362–11367, 2017.

[44] Yu Shi and Edo Waks. Deterministic generation of multidimensional photonic cluster states using time-delay feedback. *Physical Review A*, 104:013703, 2021.

[45] Kianna Wan, Soonwon Choi, Isaac H. Kim, Noah Shutty, and Patrick Hayden. Fault-tolerant qubit from a constant number of components. *PRX Quantum*, 2:040345, 2021.

[46] Yuan Zhan and Shuo Sun. Deterministic generation of loss-tolerant photonic cluster states with a single quantum emitter. *Phys. Rev. Lett.*, 125:223601, 2020.

[47] Terry Rudolph. Why i am optimistic about the silicon-photonic route to quantum computing. *APL Photonics*, 2:030901, 2017.

[48] Fulvio Flamini, Nicolò Spagnolo, and Fabio Sciarrino. Photonic quantum information processing: a review. *Reports on Progress in Physics*, 82:016001, 2018.

[49] Daniel Gottesman, Thomas Jennewein, and Sarah Croke. Longer-baseline telescopes using quantum repeaters. *Physical Review Letters*, 109:70503, 2012.

[50] Miles J. Padgett and Robert W. Boyd. An introduction to ghost imaging: quantum and classical. *Philosophical Transactions of the Royal Society A: Mathematical, Physical and Engineering Sciences*, 375:20160233, 2017.

[51] David Awschalom, Karl K. Berggren, Hannes Bernien, Sunil Bhave, Lincoln D. Carr, Paul Davids, Sophia E. Economou, Dirk Englund, Andrei Faraon, Martin Fejer, et al. Development of quantum interconnects (quics) for next-generation information technologies. *PRX Quantum*, 2:017002, 2021.

[52] Jeremy L. O'Brien. Optical quantum computing. *Science*, 318:1567–1570, 2008.

[53] E. Knill, R. Laflamme, and G. J. Milburn. A scheme for efficient quantum computation with linear optics. *Nature*, 409:46–52, 2001.

[54] Daniel Gottesman and Isaac L. Chuang. Demonstrating the viability of universal quantum computation using teleportation and single-qubit operations. *Nature*, 402:390–393, 1999.

[55] Dan Cogan, Zu-En Su, Oded Kenneth, and David Gershoni. Deterministic generation of indistinguishable photons in a cluster state. *Nature Photonics*, 17:324–329, 2023.

[56] Austin G. Fowler, Matteo Mariantoni, John M. Martinis, and Andrew N. Cleland. Surface codes: Towards practical large-scale quantum computation. *Physical Review A*, 86:032324, 2012.

[57] Jianwei Wang, Fabio Sciarrino, Anthony Laing, and Mark G. Thompson. Integrated photonic quantum technologies. *Nature Photonics*, 14:273–284, 2020.

[58] Yu Shi and Edo Waks. Quantum fourier transform on photonic qubits using cavity qed. *Physical Review A*, 106:013709, 2022.

[59] Yu Shi and Edo Waks. Error metric for non-trace-preserving quantum operations. *preprint arXiv:2110.02290*, 2021.

[60] Guifré Vidal. Efficient classical simulation of slightly entangled quantum computations. *Physical Review Letters*, 91:147902, 2003.

[61] Guifré Vidal. Efficient simulation of one-dimensional quantum many-body systems. *Physical Review Letters*, 93:040502, 2004.

[62] J. Ignacio Cirac, David Pérez-García, Norbert Schuch, and Frank Verstraete. Matrix product states and projected entangled pair states: Concepts, symmetries, theorems. *Reviews of Modern Physics*, 93:045003, 2021.

[63] Román Orús. A practical introduction to tensor networks: Matrix product states and projected entangled pair states. *Annals of Physics*, 349:117–158, 2014.

[64] F. Verstraete and J. I. Cirac. Renormalization algorithms for quantum-many body systems in two and higher dimensions. *preprint arXiv:cond-mat/0407066*, 2004.

[65] F. Verstraete and J. I. Cirac. Valence-bond states for quantum computation. *Physical Review A*, 70:060302, 2004.

[66] Andrei Faraon, Arka Majumdar, Hyochul Kim, Pierre Petroff, and Jelena Vučković. Fast electrical control of a quantum dot strongly coupled to a photonic-crystal cavity. *Physical Review Letters*, 104:047402, 2010.

[67] Ranojoy Bose, Tao Cai, Kaushik Roy Choudhury, Glenn S. Solomon, and Edo Waks. All-optical coherent control of vacuum rabi oscillations. *Nature Photonics*, 8:858–864, 2014.

[68] John Watrous. Semidefinite programs for completely bounded norms. *Theory of Computing*, 5:217–238, 2009.

[69] Dorit Aharonov, Alexei Kitaev, and Noam Nisan. Quantum circuits with mixed states. In *Proceedings of the Thirtieth Annual ACM Symposium on Theory of Computing*, pages 20–30, 1998.

[70] Dorit Aharonov and Michael Ben-Or. Fault-tolerant quantum computation with constant error rate. *SIAM Journal on Computing*, 38:1207–1282, 2008.

[71] Hyochul Kim, Ranojoy Bose, Thomas C. Shen, Glenn S. Solomon, and Edo Waks. A quantum logic gate between a solid-state quantum bit and a photon. *Nature Photonics*, 7:373–377, 2013.

[72] Shuo Sun, Hyochul Kim, Glenn S. Solomon, and Edo Waks. A quantum phase switch between a single solid-state spin and a photon. *Nature Nanotechnology*, 11:539–544, 2016.

[73] Shuo Sun, Hyochul Kim, Zhouchen Luo, Glenn S. Solomon, and Edo Waks. A single-photon switch and transistor enabled by a solid-state quantum memory. *Science*, 361:57–60, 2018.

[74] Zhouchen Luo, Shuo Sun, Aziz Karasahin, Allan S. Bracker, Samuel G. Carter, Michael K. Yakes, Daniel Gammon, and Edo Waks. A spin–photon interface using charge-tunable quantum dots strongly coupled to a cavity. *Nano Letters*, 19:7072–7077, 2019.

[75] Andreas Reiserer, Norbert Kalb, Gerhard Rempe, and Stephan Ritter. A quantum gate between a flying optical photon and a single trapped atom. *Nature*, 508:237–240, 2014.

[76] Bastian Hacker, Stephan Welte, Gerhard Rempe, and Stephan Ritter. A photon–photon quantum gate based on a single atom in an optical resonator. *Nature*, 536:193–196, 2016.

[77] R. E. Evans, M. K. Bhaskar, D. D. Sukachev, C. T. Nguyen, A. Sipahigil, M. J. Burek, B. Machielse, G. H. Zhang, A. S. Zibrov, E. Bielejec, H. Park, M. Lončar, and M. D. Lukin. Photon-mediated interactions between quantum emitters in a diamond nanocavity. *Science*, 362:662–665, 2018.

[78] Toshihiko Baba. Slow light in photonic crystals. *Nature Photonics*, 2:465–473, 2008.

[79] Michael Fleischhauer, Atac Imamoglu, and Jonathan P. Marangos. Electromagnetically induced transparency: Optics in coherent media. *Reviews of Modern Physics*, 77:633–673, 2005.

[80] Marlan O. Scully and M. Suhail Zubairy. *Quantum Optics*. Cambridge University Press, 1997.

[81] C. Monroe, R. Raussendorf, A. Ruthven, K. R. Brown, P. Maunz, L.-M. Duan, and J. Kim. Large-scale modular quantum-computer architecture with atomic memory and photonic interconnects. *Physical Review A*, 89:022317, 2014.

[82] I. Baumgart, J.-M. Cai, A. Retzker, M. B. Plenio, and Ch. Wunderlich. Ultrasensitive magnetometer using a single atom. *Physical Review Letters*, 116:240801, 2016.

[83] L.-M. Duan, M. D. Lukin, J. I. Cirac, and P. Zoller. Long-distance quantum communication with atomic ensembles and linear optics. *Nature*, 414:413–418, 2001.

[84] Łukasz Dusanowski, Cornelius Nawrath, Simone L Portalupi, Michael Jetter, Tobias Huber, Sebastian Klembt, Peter Michler, and Sven Höfling. Optical charge injection and coherent control of a quantum-dot spin-qubit emitting at telecom wavelengths. *Nature Communications*, 13:748, 2022.

[85] Kha X. Tran, Allan S. Bracker, Michael K. Yakes, Joel Q. Grim, and Samuel G. Carter. Enhanced spin coherence of a self-assembled quantum dot molecule at the optimal electrical bias. *Physical Review Letters*, 129:027403, 2022.

[86] David Press, Thaddeus D. Ladd, Bingyang Zhang, and Yoshihisa Yamamoto. Complete quantum control of a single quantum dot spin using ultrafast optical pulses. *Nature*, 456:218–221, 2008.

[87] L. M. Duan and H. J. Kimble. Scalable photonic quantum computation through cavity-assisted interactions. *Physical Review Letters*, 92:127902, 2004.

[88] Peter Lodahl, Sahand Mahmoodian, and Søren Stobbe. Interfacing single photons and single quantum dots with photonic nanostructures. *Reviews of Modern Physics*, 87:347–400, 2015.

[89] M. Bayer, G. Ortner, O. Stern, A. Kuther, A. A. Gorbunov, A. Forchel, P. Hawrylak, S. Fafard, K. Hinzer, T. L. Reinecke, S. N. Walck, J. P. Reithmaier, F. Klopf, and F. Schäfer. Fine structure of neutral and charged excitons in self-assembled in(ga)as/(al)gaas quantum dots. *Physical Review B*, 65:195315, 2002.

[90] Julia Kabuss, Florian Katsch, Andreas Knorr, and Alexander Carmele. Unraveling coherent quantum feedback for pyragas control. *J. Opt. Soc. Am. B*, 33(7):C10–C16, 2016.

[91] Pierre-Olivier Guimond, Hannes Pichler, Arno Rauschenbeutel, and Peter Zoller. Chiral quantum optics with v-level atoms and coherent quantum feedback. *Phys. Rev. A*, 94:033829, 2016.

[92] Hannes Pichler and Peter Zoller. Photonic circuits with time delays and quantum feedback. *Phys. Rev. Lett.*, 116:093601, 2016.

[93] P-O Guimond, M Pletyukhov, H Pichler, and P Zoller. Delayed coherent quantum feedback from a scattering theory and a matrix product state perspective. *Quantum Science and Technology*, 2(4):044012, 2017.

[94] S J Whalen, A L Grimsmo, and H J Carmichael. Open quantum systems with delayed coherent feedback. *Quantum Science and Technology*, 2(4):044008, 2017.

[95] Gavin Crowder, Howard Carmichael, and Stephen Hughes. Quantum trajectory theory of few-photon cavity-qed systems with a time-delayed coherent feedback. *Phys. Rev. A*, 101:023807, 2020.

[96] Sofia Arranz Regidor, Gavin Crowder, Howard Carmichael, and Stephen Hughes. Modeling quantum light-matter interactions in waveguide qed with retardation, nonlinear interactions, and a time-delayed feedback: Matrix product states versus a space-discretized waveguide model. *Phys. Rev. Res.*, 3:023030, 2021.

[97] Nikolett Német, Scott Parkins, Andreas Knorr, and Alexander Carmele. Stabilizing quantum coherence against pure dephasing in the presence of time-delayed coherent feedback at finite temperature. *Phys. Rev. A*, 99:053809, 2019.

[98] Alexander Carmele, Julia Kabuss, Franz Schulze, Stephan Reitzenstein, and Andreas Knorr. Single photon delayed feedback: A way to stabilize intrinsic quantum cavity electrodynamics. *Phys. Rev. Lett.*, 110:013601, 2013.

[99] Nikolett Német and Scott Parkins. Enhanced optical squeezing from a degenerate parametric amplifier via time-delayed coherent feedback. *Phys. Rev. A*, 94:023809, 2016.

[100] Giuseppe Calajó, Yao-Lung L. Fang, Harold U. Baranger, and Francesco Ciccarello. Exciting a bound state in the continuum through multiphoton scattering plus delayed quantum feedback. *Phys. Rev. Lett.*, 122:073601, 2019.

[101] Kisa Barkemeyer, Marcel Hohn, Stephan Reitzenstein, and Alexander Carmele. Boosting energy-time entanglement using coherent time-delayed feedback. *Phys. Rev. A*, 103:062423, 2021.

[102] D. F. Walls and Gerard J. Milburn. Input–output formulation of optical cavities. *Quantum Optics*, pages 127–141, 2008.

[103] Michael A. Nielsen. Cluster-state quantum computation. *Reports on Mathematical Physics*, 57:147–161, 2006.

[104] M. Hein, J. Eisert, and H. J. Briegel. Multiparty entanglement in graph states. *Physical Review A*, 69:062311, 2004.

[105] Robert Raussendorf, Daniel E. Browne, and Hans J. Briegel. Measurement-based quantum computation on cluster states. *Physical Review A*, 68:022312, 2003.

[106] R. Raussendorf, J. Harrington, and K. Goyal. Topological fault-tolerance in cluster state quantum computation. *New Journal of Physics*, 9:199–199, 2007.

[107] T. P. Bodiya and L.-M. Duan. Scalable generation of graph-state entanglement through realistic linear optics. *Phys. Rev. Lett.*, 97:143601, 2006.

[108] P. Walther, K. J. Resch, T. Rudolph, E. Schenck, H. Weinfurter, V. Vedral, M. Aspelmeyer, and A. Zeilinger. Experimental one-way quantum computing. *Nature*, 434:169–176, 2005.

[109] Chao-Yang Lu, Xiao-Qi Zhou, Otfried Gühne, Wei-Bo Gao, Jin Zhang, Zhen-Sheng Yuan, Alexander Goebel, Tao Yang, and Jian-Wei Pan. Experimental entanglement of six photons in graph states. *Nature Physics*, 3:91–95, 2007.

[110] I. Dhand, M. Engelkemeier, L. Sansoni, S. Barkhofen, C. Silberhorn, and M. B. Plenio. Proposal for quantum simulation via all-optically-generated tensor network states. *Phys. Rev. Lett.*, 120:130501, 2018.

[111] B. P. Lanyon, P. Jurcevic, M. Zwerger, C. Hempel, E. A. Martinez, W. Dür, H. J. Briegel, R. Blatt, and C. F. Roos. Measurement-based quantum computation with trapped ions. *Phys. Rev. Lett.*, 111:210501, 2013.

[112] I. Schwartz, D. Cogan, E. R. Schmidgall, Y. Don, L. Gantz, O. Kenneth, N. H. Lindner, and D. Gershoni. Deterministic generation of a cluster state of entangled photons. *Science*, 354(6311):434–437, 2016.

[113] Arne L. Grimsmo. Time-delayed quantum feedback control. *Physical Review Letters*, 115:060402, 2015.

[114] C. Schön, E. Solano, F. Verstraete, J. I. Cirac, and M. M. Wolf. Sequential generation of entangled multiqubit states. *Physical Review Letters*, 95:110503, 2005.

[115] Shanshan Xu and Shanhui Fan. Generate tensor network state by sequential single-photon scattering in waveguide qed systems. *APL Photonics*, 3:116102, 2018.

[116] Michael Lubasch, Antonio A. Valido, Jelmer J. Renema, W. Steven Kolthammer, Dieter Jaksch, M. S. Kim, Ian Walmsley, and Raúl García-Patrón. Tensor network states in time-bin quantum optics. *Physical Review A*, 97:062304, 2018.

[117] Matthew Fishman, Steven R. White, and E. Miles Stoudenmire. The itensor software library for tensor network calculations. *preprint arXiv:2007.14822*, 2020.

[118] Alexander V. Khaetskii, Daniel Loss, and Leonid Glazman. Electron spin decoherence in quantum dots due to interaction with nuclei. *Physical Review Letters*, 88:186802, 2002.

[119] Shuo Sun and Edo Waks. Deterministic generation of entanglement between a quantum-dot spin and a photon. *Physical Review A*, 90:042322, 2014.

[120] David Press, Kristiaan De Greve, Peter L. McMahon, Thaddeus D. Ladd, Benedikt Friess, Christian Schneider, Martin Kamp, Sven Höfling, Alfred Forchel, and Yoshihisa Yamamoto. Ultrafast optical spin echo in a single quantum dot. *Nature Photonics*, 4:367–370, 2010.

[121] M. K. Bhaskar, R. Riedinger, B. Machielse, D. S. Levonian, C. T. Nguyen, E. N. Knall, H. Park, D. Englund, M. Lončar, D. D. Sukachev, and M. D. Lukin. Experimental demonstration of memory-enhanced quantum communication. *Nature*, 580:60–64, 2020.

[122] C.-Y. Lu, Y. Zhao, A. N. Vamivakas, C. Matthiesen, S. Fält, A. Badolato, and M. Atatüre. Direct measurement of spin dynamics in inas/gaas quantum dots using time-resolved resonance fluorescence. *Physical Review B*, 81:035332, 2010.

[123] A. Yu. Kitaev. Quantum measurements and the abelian stabilizer problem. *preprint arXiv:quant-ph/9511026*, 1995.

[124] L. Hales and S. Hallgren. An improved quantum fourier transform algorithm and applications. In *Proceedings 41st Annual Symposium on Foundations of Computer Science*, pages 515–525, 2000.

[125] Shahriar Aghaeimeibodi, Chang-Min Lee, Mustafa Atabey Buyukkaya, Christopher J. K. Richardson, and Edo Waks. Large stark tuning of inas/inp quantum dots. *Applied Physics Letters*, 114:071105, 2019.

[126] Samuel G. Carter, Timothy M. Sweeney, Mijin Kim, Chul Soo Kim, Dmitry Solenov, Sophia E. Economou, Thomas L. Reinecke, Lily Yang, Allan S. Bracker, and Daniel Gammon. Quantum control of a spin qubit coupled to a photonic crystal cavity. *Nature Photonics*, 7:329–334, 2013.

[127] Alexei Gilchrist, Nathan K. Langford, and Michael A. Nielsen. Distance measures to compare real and ideal quantum processes. *Physical Review A*, 71:062310, 2005.

[128] John Watrous. *The Theory of Quantum Information*. Cambridge University Press, 2018.

[129] Joydip Ghosh, Austin G. Fowler, John M. Martinis, and Michael R. Geller. Understanding the effects of leakage in superconducting quantum-error-detection circuits. *Physical Review A*, 88:62329, 2013.

[130] Christopher J. Wood and Jay M. Gambetta. Quantification and characterization of leakage errors. *Physical Review A*, 97:032306, 2018.

[131] Reed W. Andrews, Cody Jones, Matthew D. Reed, Aaron M. Jones, Sieu D. Ha, Michael P. Jura, Joseph Kerckhoff, Mark Levendorf, Seán Meenehan, Seth T. Merkel, Aaron Smith, Bo Sun, Aaron J. Weinstein, Matthew T. Rakher, Thaddeus D. Ladd, and Matthew G. Borselli. Quantifying error and leakage in an encoded si/sige triple-dot qubit. *Nature Nanotechnology*, 14:747–750, 2019.

[132] Yue Wu, Shimon Kolkowitz, Shruti Puri, and Jeff D. Thompson. Erasure conversion for fault-tolerant quantum computing in alkaline earth rydberg atom arrays. *Nature Communications*, 13:4657, 2022.

[133] Iris Cong, Harry Levine, Alexander Keesling, Dolev Bluvstein, Sheng-Tao Wang, and Mikhail D. Lukin. Hardware-efficient, fault-tolerant quantum computation with rydberg atoms. *Physical Review X*, 12:21049, 2022.

[134] Natalie C. Brown and Kenneth R. Brown. Comparing zeeman qubits to hyperfine qubits in the context of the surface code: $^{174}\mathrm{Yb}^{+}$ and $^{171}\mathrm{Yb}^{+}$. *Physical Review A*, 97:52301, 2018.

[135] Haitan Xu and Xin Wan. Constructing functional braids for low-leakage topological quantum computing. *Physical Review A*, 78:42325, 2008.

[136] R. Ainsworth and J. K. Slingerland. Topological qubit design and leakage. *New Journal of Physics*, 13:065030, 2011.

[137] John Preskill. Fault-tolerant quantum computation. *preprint arXiv:quant-ph/9712048*, 1997.

[138] Emanuel Knill, Raymond Laflamme, and Wojciech Zurek. Threshold accuracy for quantum computation. *preprint arXiv:quant-ph/9610011*, 1996.

[139] Zuzana Gavorová. Notes on distinguishability of postselected computations. *preprint arXiv:2011.08487*, 2020.

[140] G. Vidal. Entanglement renormalization. *Physical Review Letters*, 99:220405, 2007.

[141] G. Evenbly and G. Vidal. Tensor network renormalization. *Physical Review Letters*, 115:180405, 2015.

[142] Christopher M. Dawson, Henry L. Haselgrove, and Michael A. Nielsen. Noise thresholds for optical quantum computers. *Physical Review Letters*, 96:020501, 2006.

[143] Panos Aliferis, Daniel Gottesman, and John Preskill. Accuracy threshold for postselected quantum computation. *Quantum Information and Computation*, 8:181–244, 2008.

[144] Andrew S. Darmawan and David Poulin. Tensor-network simulations of the surface code under realistic noise. *Physical Review Letters*, 119:40502, 2017.

[145] Easwar Magesan, Daniel Puzzuoli, Christopher E. Granade, and David G. Cory. Modeling quantum noise for efficient testing of fault-tolerant circuits. *Physical Review A*, 87:012324, 2013.

[146] E. Blumenthal, C. Mor, A. A. Diringer, L. S. Martin, P. Lewalle, D. Burgarth, K. B. Whaley, and S. Hacohen-Gourgy. Demonstration of universal control between non-interacting qubits using the quantum zeno effect. *npj Quantum Information*, 8:88, 2022.

[147] Emanuel Knill, Raymond Laflamme, and Wojciech H. Zurek. Resilient quantum computation. *Science*, 279:342–345, 1998.

[148] Mark S. Byrd, Daniel A. Lidar, Lian-Ao Wu, and Paolo Zanardi. Universal leakage elimination. *Phys. Rev. A*, 71:052301, May 2005.

[149] J. Pablo Bonilla Ataides, David K. Tuckett, Stephen D. Bartlett, Steven T. Flammia, and Benjamin J. Brown. The xzzx surface code. *Nature Communications*, 12:2172, 2021.

[150] M. Silva, E. Magesan, D. W. Kribs, and J. Emerson. Scalable protocol for identification of correctable codes. *Phys. Rev. A*, 78:012347, 2008.